

A FLOW BOILING MICROCHANNEL THERMOSYPHON FOR FUEL CELL THERMAL
MANAGEMENT

By

PATRICK THOMAS GARRITY

A DISSERTATION PRESENTED TO THE GRADUATE SCHOOL
OF THE UNIVERSITY OF FLORIDA IN PARTIAL FULFILLMENT
OF THE REQUIREMENTS FOR THE DEGREE OF
DOCTOR OF PHILOSOPHY

UNIVERSITY OF FLORIDA

2009

© 2009 Patrick Thomas Garrity

To my parents, James and Nancy Garrity. Without their continuous support and encouragement this work would not have been possible.

ACKNOWLEDGMENTS

The author would like to express his sincerest gratitude to his academic advisor and PhD committee chairperson, Professor James Frederick Klausner. His guidance, support, encouragement and insight contributed immensely to the accomplishment of this work. The author would also like to express his appreciation to Professor Renwei Mei for his invaluable input throughout the course of my studies. The author would like to thank Professor Jacob Chung, Professor Mark Sheplak and Professor Ranga Narayanan for serving on his PhD committee. Their insight has helped the author to develop the necessary critical thinking skills needed to become a contributing member of the academic community.

This research was supported by the National Aeronautics and Space Administration Glenn Research Center, through contract NA63-2750. Without its financial support this work would not be possible.

TABLE OF CONTENTS

	<u>page</u>
ACKNOWLEDGMENTS	4
LIST OF TABLES	8
LIST OF FIGURES	9
LIST OF ABBREVIATIONS.....	12
ABSTRACT.....	17
CHAPTER	
1 INTRODUCTION	17
PEM Fuel Cells.....	18
Two-Phase Flow and Thermosyphons.....	22
Microchannels.....	25
Compact Condensers	30
Instabilities and Subcooling.....	35
Summary	37
2 FLOW BOILING MICROCHANNEL EVAPORATOR AND THERMOSYPHON PERFORMANCE.....	39
Background and Objectives.....	39
Experimental Facility.....	42
Experimental Protocol	46
Results.....	48
Flow Modeling.....	51
3 MICROCHANNEL PRESSURE DROP CORRELATION	59
Background and Objectives.....	59
Experimental Facility.....	59
Experimental Protocol	60
Results.....	61
Pressure Drop Correlations.....	64
Conclusion	69

4	INSTABILITY PHENOMENA IN A TWO-PHASE THERMOSYPHON	70
	Background and Objectives	70
	Experimental Considerations	71
	Facility	71
	Experimental Protocol	72
	System Subcooling and Manifold Pressure Drop	72
	Flow Modeling	74
	Experimental Results	76
	Instability Prediction	82
5	PERFORMANCE OF ALUMINUM AND CARBON FOAMS FOR AIR SIDE HEAT TRANSFER AUGMENTATION	86
	Background and Objectives	86
	Experimental Facility	88
	Experimental Results	91
	Heat Transfer Analysis	95
	Results	101
	Hypothetical Heat Exchanger Performance	103
	Numerical Model	105
6	CONCLUSIONS	111
APPENDIX		
A	INSTABILITY IDENTIFICATION	113
B	UNCERTAINTY AND CALIBRATION	116
	Data Acquisition (DAQ)	116
	Pressure Drop	117
	Flow Meter Calibration	120
	Uncertainty in Power Measurement	122
	Temperature	123
	Various Parameters	125
	Wall Temperature	125
	Vapor Quality	125
	Vapor Superficial Velocity	125
	Pitot Tube Velocity	126
C	PRESSURE GRADIENT AND HEAT TRANSFER DATA FOR FOAM SAMPLES	127
D	NUMERICAL CODE FOR SOLVING POROUS MEDIA TRANSPORT EQUATIONS	130
	LIST OF REFERENCES	145

BIOGRAPHICAL SKETCH152

LIST OF TABLES

<u>Table</u>	<u>page</u>
1-1 Typical values of the convection heat transfer coefficient.	24
1-2 Various types of two-phase flow instability.	37
3-1 Frictional pressure drop data.....	62
3-2 Error between measured and predicted frictional pressure drop for various models.	69
4-1 Experimentally observed limiting heat flux.....	78
5-1 Foam properties.	92
5-2 Relative error for pressure drop and Nusselt number correlations.	103
5-3 Geometric parameters for louvered fin configuration.	107
B-1 Diaphragm maximum pressure, sensitivity parameter, and standard error of the estimate for each pressure transducer.	120
C-1 Pressure gradient for different foams.....	128
C-2 Volumetric heat transfer coefficient and upper fall temperature for different foams.	129

LIST OF FIGURES

<u>Figure</u>	<u>page</u>
1-1 Operation of a PEM fuel cell.	19
1-2 Thermosyphon.	23
1-3 Microchannel and conventional channel configurations.	26
1-4 Cross- flow condenser.....	31
1-5 Thermal transport mechanisms inside the condenser.	32
1-6 Thermal resistance inside the condenser.....	32
1-7 Flow field and boundary layer for louver type fins.	34
2-1 Experimental two-phase thermosyphon.....	42
2-2 Exploded view of the cooling plate assembly.....	43
2-3 Section view of flow meter.	44
2-4 Thermocouple locations on cooling plate.	45
2-5 Degree of inlet sub cooling variation with heat flux.....	47
2-6 Variation of flow rate with heat flux.....	48
2-7 Wall temperature at various locations.....	49
2-8 Variation in vapor quality with channel height.....	51
2-9 Measured and predicted microchannel pressure drop variation with flow rate.	54
2-10 Comparison between measured and predicted flow rate.	55
2-11 Comparison between measured and predicted wall temperature at thermocouple location 5 based on measured flow rate and vapor quality.	56
3-1 Thermosyphon experimental facility.	60
3-2 Experimental versus predicted frictional pressure drop using Friedal correlation.	67
3-3 Experimental versus predicted frictional pressure drop using Mueller-Steinhagen correlation.	67
3-4 Experimental versus predicted frictional pressure drop using homogeneous model.....	68

3-5	Experimental versus predicted frictional pressure drop using Lee correlation.....	68
4-1	Variation of inlet subcooling with heat flux.	73
4-2	Pressure drop across inlet and outlet manifolds.....	74
4-3	Mass flow rate variation with increasing heat flux.....	76
4-4	Pressure drop variation across the microchannel evaporator plate with respect to mass flow rate.	77
4-5	Upper and lower bounds for predicted mass flow rates for H = 1.33 m and H = 0.79 m.	78
4-6	Measured probability density function for pressure drop prior to unstable flow.	79
4-7	Measured probability density function for mass flow rate prior to unstable flow.....	79
4-8	Measured probability density function for mass flow rate following the onset of unstable flow.	80
4-9	Measured probability density function for pressure drop following the onset of unstable flow.....	81
4-10	Power spectrum for mass flow rate.....	82
4-11	Pressure drop across the microchannel plate for varying flow rate at H=1.33 m.....	84
4-12	Comparison of measured and predicted heat flux at the onset of instability.....	85
5-1	Foam samples.....	89
5-2	Porous media experimental facility.	91
5-3	Axial pressure upper wall temperature variation for 10 PPI aluminum foam sample, $u_m = 1.13 \text{ m/s}$	93
5-4	Carbon foam pressure gradient variation with mean air velocity.	93
5-5	Aluminum foam pressure gradient variation with mean air velocity.	94
5-6	Foam upper wall temperature variation with mean air velocity.	94
5-7	Dimensionless velocity profile.	97
5-8	Dimensionless temperature profile	98
5-9	Carbon foam volumetric heat transfer coefficient variation with mean fluid velocity.....	99

5-10	Aluminum foam volumetric heat transfer coefficient variation with mean fluid velocity.....	100
5-11	Nusselt number correlation for aluminum foams.	102
5-12	Nusselt number correlation for carbon foams.....	103
5-13	Hypothetical heat exchanger in cross flow	104
5-14	Geometric comparison of louvered fin and foam heat exchanger configurations.	107
5-15	Comparison of coefficient of performance for louvered fin and foam configurations....	108
5-16	Comparison of compactness factor for louvered fin and foam configurations.....	109
5-17	Comparison of power density for louvered fin and foam configurations.....	110
B-1	Pressure drop calibration curve used for measurement of pressure drop	119
B-2	Flow rate versus pressure drop calibration curve used for measurement of flow rate within the venturi flow meter.....	121
B-3	Temperature calibration curve for a type-E thermocouple.....	124

LIST OF ABBREVIATIONS

A	Area (m^2)
a	Surface area per unit volume (m^{-1})
Bi	Biot number
C	Thermal conductivity ratio
C_F	Inertia coefficient
C_0	Distribution parameter
C_p	Constant pressure specific heat (J/kgK)
$C_{p,f}$	Constant pressure specific heat of fluid (J/kgK)
CF	Compactness factor (W/m^3)
COP	Coefficient of performance
d	Hydraulic diameter (m)
D	Machined passage diameter (m)
Da	Darcy number
D_k	Dimensionless parameter describing small scale friction
\dot{E}_{input}	Electrical Energy (W)
F_h	Fin height (mm)
F_p	Fin pitch (mm)
f	Friction factor
f_s	Sampling frequency (1/s)
G	Mass velocity (kg/m ² s)
g	Gravitational constant (m/s ²)

H	Condenser Height (m)
h_{sf}	Interstitial heat transfer coefficient (W/m^2K)
h_v	Volumetric heat transfer coefficient (W/m^3K)
h_{fg}	Latent heat of vaporization (J/kg)
K	Permeability (m^2)
k	Thermal conductivity (W/mK)
L	Axial length of cartridge heater (m)
L_a	Louver angle (degrees)
L_d	Louver depth (mm)
L_H	Louver height (mm)
L_p	Louver Pitch (mm)
m	Mass (kg)
\dot{m}	Mass flow rate (kg/s) or (g/s)
N	Number of samples
Nu_K	Nusselt number
P	Pressure (Pa) or (kPa)
PD	Power Density (W/kg)
Pr	Prandtl number
\dot{q}	Heat rate (W)
$\dot{Q}_{removed}$	Heat removed from hypothetical condenser (W)
q_w	Heat flux along heater wall (W/m^2)

R	Flow resistance ($Pa\ s/kg$)
Re_K	Reynolds number based on permeability
Re_L	Reynolds number based on L
Re	Reynolds number
St	Stanton number
T	Temperature ($^{\circ}C$)
U	Normalized fluid U-velocity
u	Fluid u-velocity (m/s)
u_m	Mean fluid velocity (m/s)
u_v	Superficial vapor velocity (m/s)
V	Volume (m^3)
V_{vj}	Drift velocity (m/s)
W	Width (m)
x	Vapor quality
x'	Dimensionless x-coordinate
y'	Dimensionless y-coordinate
z	Axial location (m)

Greek Symbols

α	Vapor volume fraction
ε	Porosity
ε_p	Carbon foam porosity based on interstitial pores
Φ_{fr}	2-phase friction multiplier

μ	Dynamic viscosity (Ns/m^2)
ν	Kinematic viscosity (m^2/s)
θ	Inclination angle (radians)
ρ	Density (kg/m^3)
σ	Surface tension (N/m)
ΔP	Pressure drop (Pa)
ΔP_s	Total system pressure drop (Pa)
ΔP_m	Measured pressure drop (Pa)
ΔP_p	Predicted pressure drop (Pa)

Subscripts

2ϕ	Two-phase mixture
a	Accelerational component
<i>amb</i>	Ambient air
<i>b, f</i>	Bulk fluid
e	Exit
f	Frictional component
<i>fl</i>	Fluid
<i>fe</i>	Effective fluid property
g	Gravitational component
i	Inlet
<i>K</i>	Permeability based length scale
l	Liquid

<i>m</i>	Mixture
<i>mf</i>	Mean fluid velocity
<i>s</i>	Solid
<i>se</i>	Effective solid property
<i>T</i>	Total
<i>v</i>	Vapor
<i>w</i>	Wall
<i>z</i>	z-location

Abstract of Dissertation Presented to the Graduate School
of the University of Florida in Partial Fulfillment of the
Requirements for the Degree of Doctor of Philosophy

A FLOW BOILING MICROCHANNEL THERMOSYPHON FOR FUEL CELL THERMAL
MANAGEMENT

By

Patrick T. Garrity

May 2009

Chair: James Frederick Klausner

Major: Mechanical and Aerospace Engineering

To provide a high power density thermal management system for proton exchange membrane (PEM) fuel cell applications, a passively driven thermal management system was assembled to operate in a closed loop two-phase thermosyphon. The system has two major components; a microchannel evaporator plate and a condenser. The microchannel evaporator plate was fabricated with 56 square channels that have a 1 mm x 1 mm cross section and are 115 mm long. Experiments were conducted with a liquid cooled condenser with heat flux as the control variable. Measurements of mass flow rate, temperature field, and pressure drop have been made for the thermosyphon loop. A model is developed to predict the system characteristics such as the temperature and pressure fields, flow rate, flow regime, heat transfer coefficient, and maximum heat flux. When the system is subjected to a heat load that exceeds the maximum heat flux, an unstable flow regime is observed that causes flow reversal and eventual dryout near the evaporator plate wall. This undesirable phenomenon is modeled based on a quasi-steady state assumption, and the model is capable of predicting the heat flux at the onset of instability for quasi-steady two-phase flow.

Another focus of this work is the performance of the condenser portion of the loop, which will be air cooled in practice. The aim is to reduce air side thermal resistance and increase the

condenser performance, which is accomplished with extended surfaces. A testing facility is assembled to observe the air side heat transfer performance of three aluminum foam samples and three modified carbon foam samples, used as extended surfaces. The aluminum foam samples have a bulk density of 216 kilograms per cubic meter with pore sizes of 0.5, 1, and 2 mm. The modified carbon foam samples have bulk densities of 284, 317, and 400 kilograms per cubic meter and machined flow passages of 3.2 mm. in diameter. Each sample is observed under forced convection with air velocity as the control variable. Thermocouples and pressure taps are distributed axially along the test section and measurements of pressure and temperature are recorded for air velocities ranging from 1-6 meters per second. Using the Darcy-Forcheimer equation, the porosity is determined for each sample. The volumetric heat transfer coefficient is extracted by means of solving the coupled energy equations of both the solid and fluid respectively. Nusselt number is correlated with Reynolds number. The optimal foam configuration is explored based on a Coefficient of Performance, (COP), Compactness Factor (CF) and Power Density (PD). The COP is the ratio of total heat removed to electrical heat consumption of the blower, CF is the total heat removed per unit volume, and PD is the total heat removed per unit mass. These performance parameters are computed for a hypothetical heat exchanger using each foam sample at various fluid velocities. They are also compared against those for the hypothetical heat exchanger fitted with conventional louvered fins. Given a proper weighting function based on the importance of CF, COP, and PD in the condenser design, an optimal configuration for an air cooled condenser can be obtained for various operating conditions.

CHAPTER 1 INTRODUCTION

Fuel cells are expected to play a major role in energy production within the foreseeable future. Increasing concerns about pollution and possible anthropogenic global warming, coupled with economic issues involving fossil fuels have accelerated research interest in alternative energy systems. Energy Systems that run on a clean, economical energy source such as hydrogen are of particular interest. It is anticipated that the development and deployment of economical and reliable fuel cells could be the catalyst for hydrogen production and usage. Proton Exchange Membrane Fuel Cells (PEMFC) are of significant interest to the automobile, avionics and space industries, due to the potential for high power density, relatively quick start up, rapid response to varying loads, and low operating temperatures. In addition, there is effectively no pollution produced during operation of PEM fuel cells as water and heat essentially make up all of the exhaust to the environment (Vishnyakov, 2006).

Thermal issues arise within a PEM fuel cell stack that can significantly limit its cells performance. By rapidly removing heat from the fuel cell stack as it is generated, it is possible to maintain the stack temperature within its optimal range. Such a heat removal technology can increase both the power density and energy density. The objective of this work is to understand and analyze the heat transfer performance of a two-phase microchannel evaporator plate that can be inserted within a PEMFC stack used in conjunction with a two-phase thermosyphon. The system operates in a natural circulation mode which reduces the required pumping energy. Initial experiments are conducted with a liquid cooled condenser, with focus being on the evaporator plate. After taking extensive measurements of the temperature and pressure fields within the microchannel evaporator plate, a 1-D model is developed to predict the thermal hydraulics of the cooling plate including the maximum heat removal capabilities, where the

limiting heat flux is governed by system instabilities. The ideal working fluid for the thermosyphon loop is chosen with a saturation temperature that allows for the fuel cell stack to operate within its optimal range. Once the maximum heat removal of the cooling plate is known, along with the properties of the ideal working fluid, focus is shifted to the condenser design, with a focus on maximizing air side heat transfer rates. Carbon and metallic foams are configured as extended surfaces for heat transfer augmentation. The various metallic and carbon foam materials are placed in a forced convection arrangement and the volumetric heat transfer characteristics of each sample are analyzed and correlated. Each foam configuration is evaluated based on a Coefficient of Performance, (COP), Compactness Factor (CF) and Power Density (PD). These performance parameters are computed for a hypothetical heat exchanger using each foam sample at various fluid velocities. They are also compared against those for the hypothetical heat exchanger fitted with conventional louvered fins. Given a proper weighting function based on the importance of CF, COP, and PD in the condenser design, an optimal configuration for an air cooled condenser can be obtained for various operating conditions.

PEM Fuel Cells

The basic operation of a PEMFC converts hydrogen fuel to electricity by passing the fuel across a solid polymer membrane, a thin plastic film that is permeable to protons, but does not conduct electrons. Thus electrons are forced through an external electric circuit for power production, see Figure 1-1. The solid polymer membrane, also known as the electrolyte, is located between the anode and the cathode side of the cell. At the anode, the hydrogen makes contact with a thin layer of platinum catalyst and the electron is stripped away from the hydrogen. The liberated electrons continue to flow through the external circuit while the protons travel through the electrolyte to the cathode side (Barbir, 2005). The anode side half reaction is



On the cathode side, protons passing through the membrane encounter oxygen and the electrons from the external circuit. They recombine at a catalyst electrode layer to form liquid water, which is drained away so as to not block the fuel cell. The cathode side half reaction is given in Eq. (1-2), while the total reaction is provided in Eq. (1-3).

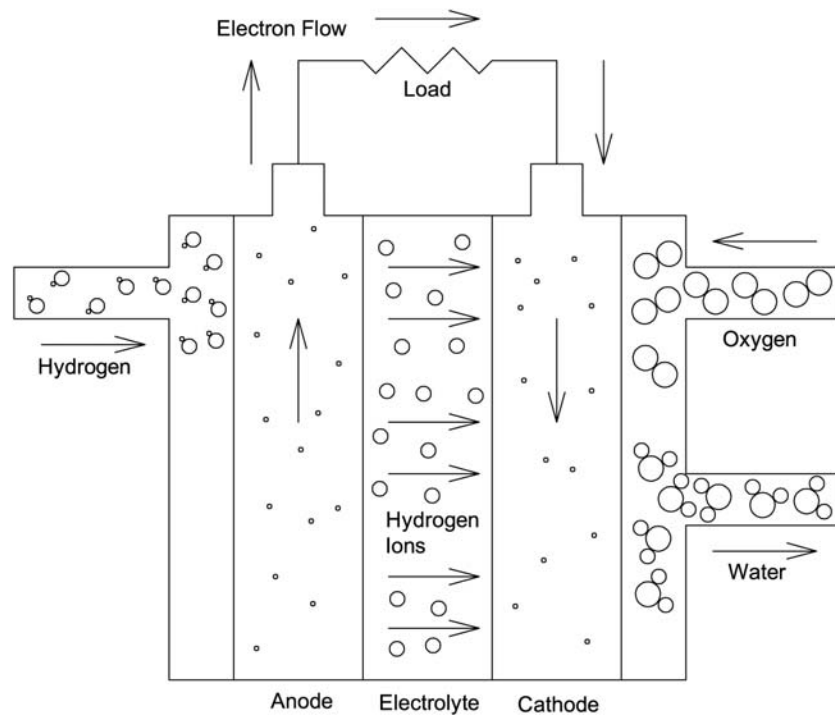


Figure 1-1. Operation of a PEM fuel cell.

Prior to operation, in an open circuit, there exists a voltage potential between the anode and cathode sides of the cell due to the free electrons generated at the electrolyte. Once the circuit is closed and the load is connected, external current is generated initiating the chemical reaction within the cell. As the external resistance is reduced the reaction rates increase allowing

the current to adjust, while simultaneously generating different types of internal resistance in the process.

In the case of PEM fuel cells, the polymer membrane is solid; reducing corrosion and electrolyte management problems. However, in order for the hydrogen ions to conduct through to the cathode, sufficient hydration is required. The proton has to first bind with water to form hydronium ions, which are then drawn across the membrane by the existing electric field. This implies that every proton moving across the membrane carries along with it a certain number of water molecules. This phenomenon is referred to as electro-osmotic drag (Coppo et al., 2005). If there is not enough water present, a high resistance to proton conduction takes place while on the other hand, if too much water is present, flooding will occur and block the transport of reactants. This process makes water management essential. Likewise, thermal problems can arise within the stacks that significantly lower the fuel cell efficiency.

With the hopes of optimizing efficiency, PEM fuel cells have recently been subject to an ever-increasing number of modeling efforts for the past 15 years. Accurate models describing the complex coupling of the heat, mass and momentum transfer within the stack are a crucial step in optimizing fuel cell efficiency with regards to thermal management. Coppo et al. (2005) developed a 3-D computational model to describe the effects of temperature on the operation of PEM fuel cells. It is shown that temperature affects the fuel cell differently depending on current density. At low current density, ($0 < J < 0.2 \text{ A/cm}^2$) reaction activation losses are dominant, in the intermediate current density range ($0.2 < J < 0.7 \text{ A/cm}^2$), ohmic losses are strongest, and at higher current density, mass transport losses prevail. In the activation regime, or low current density operation, the optimal temperature is balanced between the effects of the cathode side activation overpotential and the open circuit resistance, i.e. an increase in temperature lowers the activation

overpotential, which increases current density. However this simultaneously raises electrical resistance, reducing the cell power output. At slightly higher current densities, classified as the ohmic region, electro-osmotic drag becomes more significant causing the optimal temperature to be governed by membrane ionic conductivity and dissolved water diffusivity. Higher temperature decreases the ionic conduction due to the reduced hydration in the presence of electro-osmotic drag. On the other hand, lowering the temperature decreases the dissolved water diffusivity. This causes the membrane hydration level to be less homogeneous, bringing about localized regions of low ionic conductivity. Finally, for high current density operation, also known as the mass transport limited regime, the optimal temperature is governed by the resistance to reactant transport that results from the high mass flow rates required to sustain the electrochemical reactions at a rapid rate (Coppo et al., 2005). By increasing the operating temperature, the oxygen diffusivity within the gas diffusion layer as well as the ion-conducting polymer is enhanced. Simultaneously, the air/water concentration ratio influencing reaction kinetics decreases with temperature. The higher water content in the gas stream reduces oxygen concentration at the cell inlet. So even though the oxygen diffusivity is higher, less oxygen is available when the temperature is too high, reducing the cathode overpotential and consequently cell voltage. Similarly, water diffusivity increases with temperature due to the strong temperature dependency of kinematic viscosity, contact angle, and surface tension. It should also be noted that there is a strong coupling between the liquid water and oxygen diffusion, since higher liquid water diffusion increases the water content in the gas stream. The resulting optimal temperature within the mass transport limited regime is governed by a balance of the coupled oxygen and liquid water diffusivities as well as the resulting saturation level of the oxygen at the

cell inlet. It can then be concluded that optimal operating temperatures vary depending on the fuel cell output or current density.

You and Liu (2002) have developed a two-phase flow transport model for the cathode side of PEM fuel cells. They have demonstrated that there exists an operating temperature for optimum performance that tends to be in the range of 70-80 °C. This low operating temperature, coupled with the large heat flux removal demand renders thermal management a difficult task and further elucidates the need for enhanced modes of thermal transport. There are also several advantages to the low operating temperature that allow PEM fuel cells to be used as lightweight and mobile energy sources. For instance, at low operating temperature, the fuel cell is capable of warming up quickly which can be beneficial for mobile applications. Other advantages include the elimination of expensive containment structures and less wear on system components, resulting in better durability. By implementing various heat removal methods such as two-phase heat transfer in a thermosyphon, this low operating temperature can make PEM fuel cells more practical to energy production.

Two-Phase Flow and Thermosyphons

The concept of passively driven thermal management has been the focus of intense research in a wide variety of applications both small and large scale. Two-phase thermosyphons are considered to be high efficiency heat transfer devices capable of transporting relatively large amounts of heat with a relatively small temperature drop. This low thermal resistance encountered in thermosyphons has proven useful in small applications such as microelectronics cooling and solar water heaters, as well as larger scale applications such as nuclear reactors and heat exchangers used in the petroleum industry. Faghri (1995) and Peterson et al. (1993), among others, have reviewed the theory and the applications of the two phase thermosyphon

technology. Aside from the low thermal resistance and the uniform temperature distribution in both the evaporator and condenser sections of the thermosyphon loop, thermosyphons have many advantages over other cooling techniques.

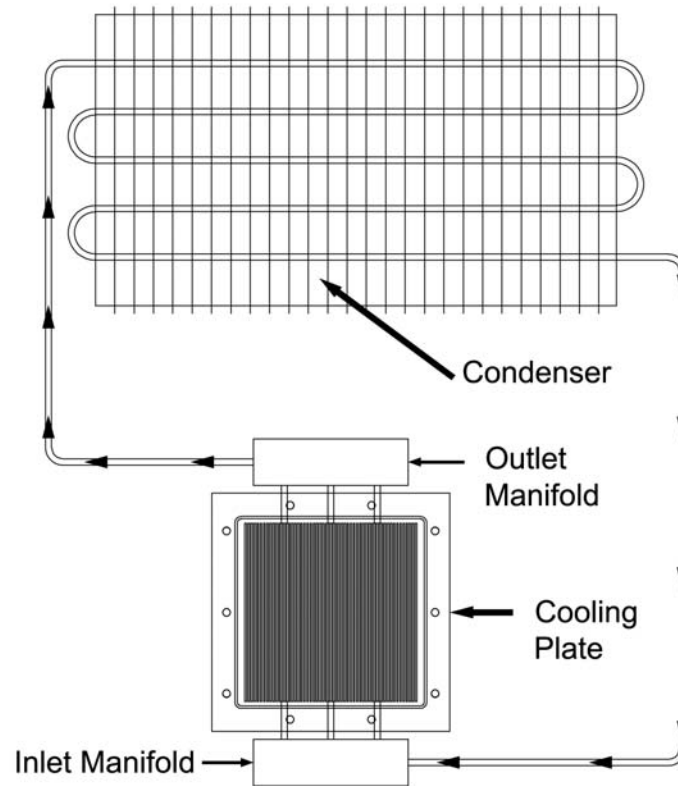


Figure 1-2. Thermosyphon.

In a two-phase thermosyphon, see Figure 1-2, heat is conducted from the heat source, across an interface, to an evaporator plate. At this point the coolant inside the plate is vaporized, taking with it the latent heat of vaporization. The vapor then travels up the riser and into the condenser where it condenses, transferring the latent heat to the tube wall. Forced air blown over the condenser dissipates heat to the ambient, while the condensate travels back down to the evaporator plate and the cycle is repeated. The density difference between the vapor and the liquid portions of the loop, create a pressure head that drives the flow. The thermal resistance encountered within the evaporator plate and throughout the condenser will play a critical role in

the overall system heat removal capabilities. This process has several advantages over single phase, forced convection techniques. By utilizing phase change heat transfer, heat rejection capabilities become an order of magnitude greater than that for single-phase, (Table 1-1). On the other hand, there exists a limiting heat flux at which point the system flow becomes unstable.

Table 1-1. Typical values of the convection heat transfer coefficient.

Process	$h(W/m^2K)$
Free convection	
Gases	2-25
Liquids	50-100
Forced convection	
Gases	25-250
Liquids	100-20,000
Convection with phase change	
Boiling or Condensation	2500-100,000

(Incropera et al. 2007)

The idea of a thermosyphon dates back to 1836 with the invention of the Perkins Tube (Palm & Tengblad, 1996). The idea was thought up for transferring heat from a furnace to a baking oven with the hopes of producing more uniformly baked bread. More recently, thermosyphons have been put into practice in demanding thermal management application. However, the specific purpose of a thermosyphon is not necessarily for cooling, but to transfer heat away from a heat source, where cooling can be achieved more conveniently by means of a secondary coolant. By implementing a multi-phase evaporator plate to transfer the heat away from the source, it becomes beneficial to include an air-cooled condenser with an extended surface and relatively low thermal resistance to condense the working fluid. Palm and Tengblad (1996) classify this type of thermosyphon as an advanced thermosyphon loop in a detailed review of thermosyphon loops. In this paper Palm and Tengblad (1996) clarify the reasons for thermosyphon system failure. They show that the heat transfer capacity of a simple

thermosyphon loop with adequate filling is restricted only by the pressure drop limit and the boiling limit. In the case of an advanced thermosyphon loop, it is possible to enhance the boiling surface in order to prevent any system failure that results near the boiling limit. Therefore, the heat removal capabilities of a thermosyphon with an advanced configuration are only limited by the pressure drop limit, which entails flow oscillations and eventually system failure due to dryout at relatively high heat flux.

In order to reduce the thermal resistance within the thermosyphon considered in this work, a microchannel plate will be used in the evaporator. The purpose of the microchannels is to enhance the thermal transport from the plate to the working fluid, which will help the efficiency of the condenser by increasing the temperature difference between the vapor and ambient.

Microchannels

Within the past twenty years, there have been a growing number of experimental studies on two-phase flow and evaporation heat transfer in microchannels that suggest significant improvement in heat transfer over conventional channels. Pioneering research in this field began about 2 decades ago with Tuckerman and Pease (1981). Applications such as micro-heat exchangers, micro-cooling assemblies and micro-thermal-mechanical systems (MTMS) are rapidly advancing. While microchannel cooling has contributed largely to the success of these smaller scale systems, a lack of fundamental understanding still exists that limits design methods. Thome (2004) has provided a literature review on microchannel boiling. He explains that there is currently no distinct definition for the transition from conventional channels to microchannels. Mehendal et al. (2003) recommends a size classification as follows: microchannels (1-100 μm), mesochannels (100 μm to 1mm), macrochannels (1-6mm), and

conventional channels ($D_h \geq 6\text{mm}$) while Kandlikar (1997) recommends the following classification and size ranges: microchannels ($50\text{-}600 \mu\text{m}$), minichannels ($600 \mu\text{m}$ to 3mm) and conventional

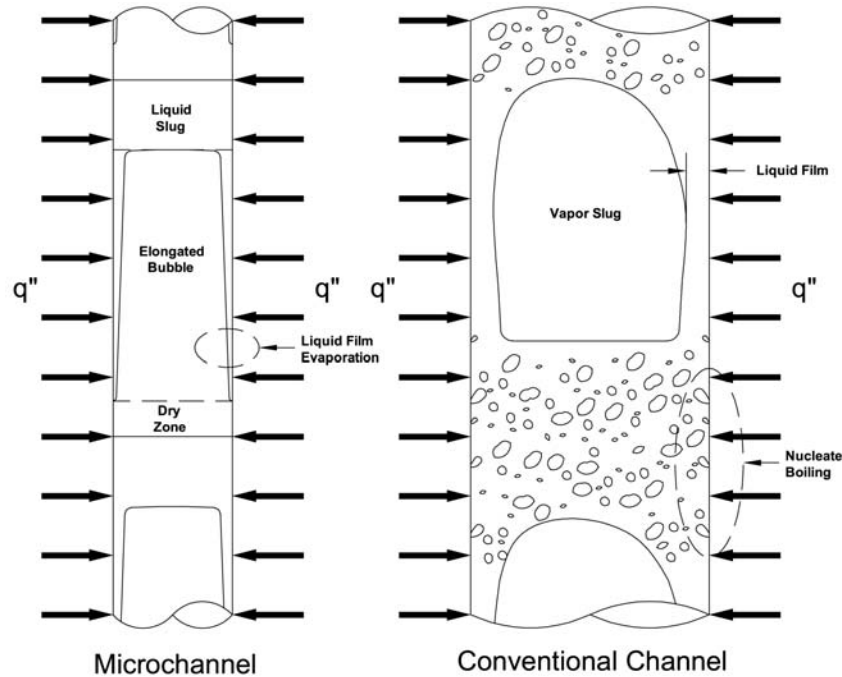


Figure 1-3. Microchannel and conventional channel configurations.

channels ($D_h \geq 3\text{mm}$). Although there is no clear understanding of the transition, Thome does discuss several explanations for the error that arises when using conventional models to describe the heat transfer and pressure drop present in microchannels. In both two-phase heat transfer and pressure drop correlations found in the literature for large scale configurations, there is a large reliance on experiment. The experiments used to fit these correlations are more often than not found to be in a turbulent type flow regime. Do to the small length scales associated with microchannels; laminar flow is more frequently observed. Therefore, it is not fair to assume that the flow characteristics such as flow transition, vapor volume fraction and drift velocity, among others found in a laminar flow will accurately reflect those encountered in experiments with

flows of a turbulent nature. Other effects such as capillary (surface tension) forces will also strongly effect flow transitions as well as flow structure. The flow structure observed in microchannels is described by Thome (2004), see Figure 1-3. He suggests that under high heat flux conditions, there exist three important regions, a liquid slug, elongated bubble, and dry zone region.

This alternate flow configuration that is observed in microchannels results from the combination of vapor bubble departure diameter to channel size ratio (d_b/d_h) and surface tension effects. While Mehendal et al. (2000) and Kandlikar (2001) have made preliminary estimates of the channel size in which these alternate flow structures are observed, it has been accepted that a proper threshold value at which a channel can be classified as “micro” will depend on the fluid properties, system pressure, surface characteristics, flow properties, etc.

Kandlikar (2005) provides a detailed review on experimental work and observation of microchannel flow boiling. He concludes that nucleating bubbles are present in flow boiling under high shear conditions during the bubbly, slug, and annular flow regimes. The bubbles depart into the flow as individual bubbles unless their size is smaller than the channel dimension normal to the nucleating surface. Small bubbles continue to grow until they eventually become confined by the channel walls under the confined flow pattern which is similar to a plug flow seen in conventional channels followed by an annular flow pattern at higher vapor qualities. Throughout each stage, Kandlikar argues that a combination of nucleate boiling and convective heat transfer are the dominant mechanisms responsible for thermal transport, as is the case in conventional channels. Kasza et al. (1997) use a high speed camera to observe boiling phenomenon at high bubble nucleation frequencies. Through flow visualization, he provides evidence that nucleate boiling within the thin liquid film is present within the slug flow regime,

supporting Kandlikar's argument. Relying heavily on experimental measurements, Kandlikar (2004) suggests a correlation for heat transfer within microchannels and compares it against a large database. For experiments with Reynolds number ranging from 400 to 3000, (laminar to turbulent transition type flow), the average deviation between the predicted heat transfer coefficient and the data is 21.9%. For low Reynolds number flows ($100 \leq Re_D \leq 410$), Kandlikar's correlation deviates 16.3% from the data and for very low Reynolds number flows ($Re \leq 100$), the average deviation from experimental data is 17.3%.

Thome et al. (2004) claim that transient evaporation of the thin liquid film surrounding the elongated bubbles is the dominant heat transfer mechanism as opposed to nucleate boiling. Due to the strong surface tension forces present in microchannels, he suggests there are nearly no stratification effects or orientation effects, making the most important flow regimes bubbly, elongated bubble, annular, mist, and flows with partial dryout. For evaporating flow, Thome reasons that the lifespan of the bubbly flow regime in microchannels is short lived and the dominating regimes are elongated bubble followed by annular flow. Here Thome presents a *three-zone* flow boiling heat transfer model to describe the evaporation of the thin liquid film that is present in the elongated bubble flow regime that also includes the effects of partial dryout, see Figure 1-3. He argues that even though the evaporation process is heat flux dependent, bubble nucleation is not the dominant form of thermal transport. The evaporation of the thin liquid film is the dominant heat transfer mechanism within microchannels. This dynamic system is modeled based on the time averaged heat transfer that occurs from the cyclic pattern of each of the three zones. In conclusion, this model predicts the transient variation in local heat transfer coefficient during the cyclic passage of (1) a liquid slug, (2) an evaporating elongated bubble, and (3) a vapor slug. There is strong dependency on the bubble frequency and the liquid film

geometry at formation and dryout. He shows that the heat transfer in the elongated bubble zone, where a thin liquid film exists, promotes heat transfer that is an order of magnitude greater than that in the liquid slug region. In contrast the vapor slug, or dryout zone, provides negligible heat transfer. The relative length of each zone is crucial for proper modeling as they influence the time period for each zone to pass the point of observation for each cycle and thus the value of the local time-averaged heat transfer coefficient. With experimental data taken from 9 sources covering tube diameters ranging from 0.51 to 3.1 mm, mass velocities of 50 to 564 kg/m^2s , pressures ranging from 124 to 5776 kPa, heat fluxes from 5 to 178 kW/m^2 , and vapor qualities in the range of 0.01 to 0.99, Thome (2004) compares against his 3-zone model and predicts 67% of the points within $\pm 30\%$. Excluding multichannel experiments, the model was able to predict 77% of the data to within $\pm 30\%$.

An experimental investigation on pressure drop within microchannels has been provided by Kandlikar (2005). He shows that in the case of multiple parallel channels, there are pressure fluctuations that are proportional to surface temperature, and occasionally flow reversal is observed. Ribatski (2006) provides a two-phase pressure drop correlation in microchannel flow. In the laminar region he uses a homogeneous model while using Mueller-Steinhagen (1986) friction correlation for turbulent flow. Ribatski (2006) compares this model against 2210 experimental two-phase frictional pressure drop data points, and with exception to the transition region, provides reasonable agreement. More than 85.7% of the data were correlated within $\pm 20\%$ and over 96% within $\pm 30\%$. Lee and Lee (2001) provide a pressure drop correlation for two-phase flow through small channels. Using a modified Lockhart-Martinelli (1949) type correlation, Lee and Lee (2001) correlate all of the data within $\pm 10\%$.

During flow boiling experiments near the limiting case of a microchannel configuration, conventional two phase frictional pressure drop and flow boiling models are capable of reasonably predicting the pressure and heat transfer characteristics. Gungor and Winterton (1986)(1987) provide two-phase heat transfer correlations that are applicable to subcooled flow. The first of the two is based on the convective heat transfer coefficient and the boiling number, while the latter uses the method of superposition similar to the Chen (1966) correlation, which couples the convective boiling heat transfer and the nucleate boiling heat transfer to obtain an overall 2-phase heat transfer coefficient. Both agree reasonably with experiments for conventional channels. Kandlikar (1991) also presents a correlation based on the boiling number that does a reasonably good job in predicting 2-phase heat transfer coefficients in large scale channels.

Several correlations for frictional pressure drop through conventional size channels have been presented in the literature. Mueller-Steinhagen (1996) uses a method of superposition which couples the single-phase pressure drop of the vapor and liquid respectively. The average deviation between the predicted and the measured values are $\pm 41\%$. Other two-phase frictional pressure drop models include Lockhart and Martinelli (1949) and Friedel (1979) which incorporate a 2-phase frictional multiplier to account for the increased pressure drop within a two-phase flow.

Compact Condensers

In order to design a high performance thermosyphon loop, the design and fabrication of a compact efficient condenser is necessary. The condensation process will transfer the latent heat of the vapor to the ambient air. There are a limited number of configurations available for the air cooled condensation process. On the airside it is most common to have a plate-fin type arrangement. The addition of fins increases the surface area and reduces the thermal resistance

significantly. More recently however, materials such as carbon and metal foams have been used in place of fins and have shown low airside thermal resistance. With the goal of minimizing the air side pumping power and overall condenser volume, difficulty arises on the liquid side when choosing an arrangement that allows for the proper drainage. The most common configurations include the Serpentine/Parallel Cross Flow Condenser, Downflow Condenser, and the Reflux Condenser; (Figure 1-4). Each configuration has its own benefits and drawbacks.

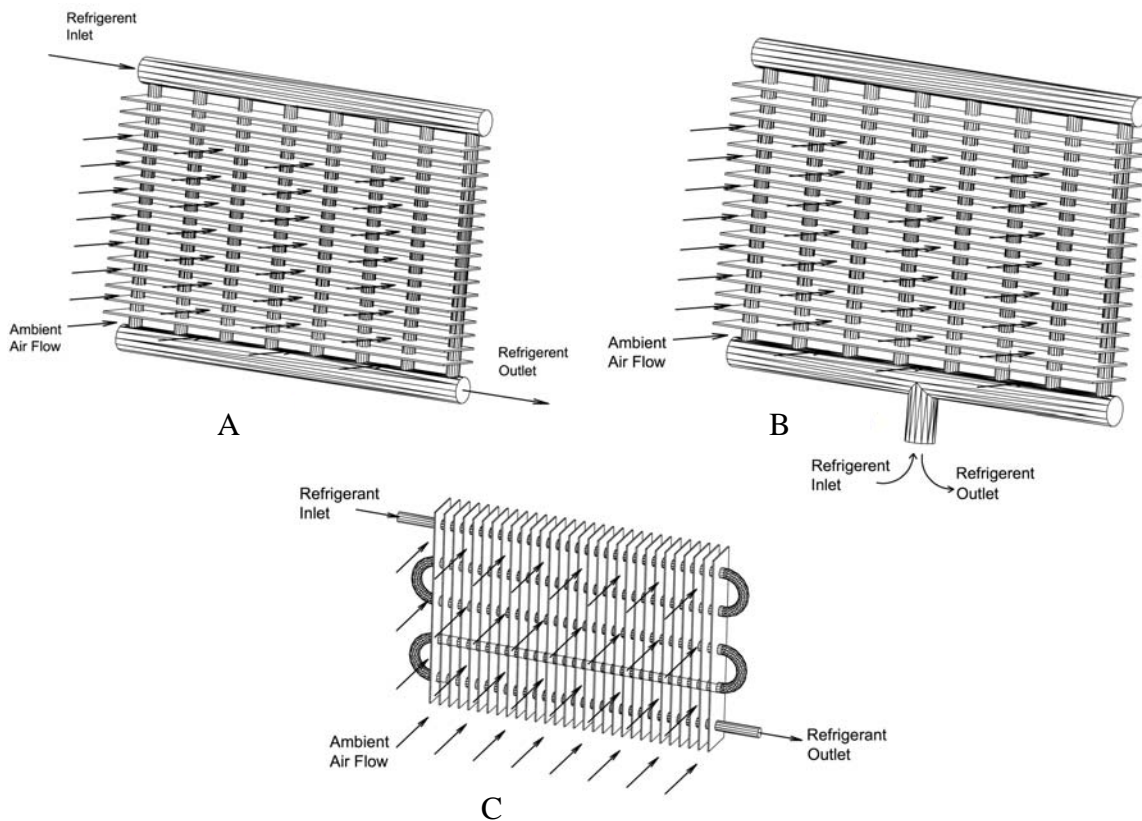


Figure 1-4. Cross- flow condenser. A) Downflow. B) Reflux. C) Serpentine.

In the case of plain fins, as is shown in Figures 1-4a through 1-4c, there exist several copper tubes, either in serpentine or parallel, surrounded by an array of fins, usually aluminum or copper, which add surface area and pull heat away from the copper tubing. The mechanisms responsible for the thermal transport are illustrated in Figure 1-5.

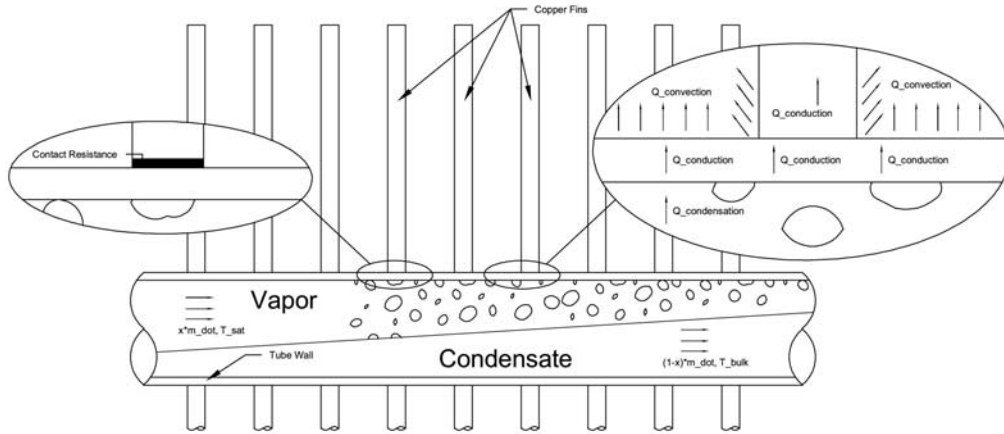


Figure 1-5. Thermal transport mechanisms inside the condenser.

Q_{total}	Total Heat Transfer	$R_{condensation}$	Condensation Resistance
Q_{fin}	Heat Transferred from Fin to Ambient	$R_{pipe\ wall}$	Pipe Conduction Resistance
Q_b	Heat Transferred from Pipe to Ambient	$R_{contact}$	Contact Resistance
T_{sat}	Saturation Temperature	R_{fin}	Fin Resistance
T_{∞}	Ambient Temperature	R_{base}	Convection Resistance
N	Number of Fins		

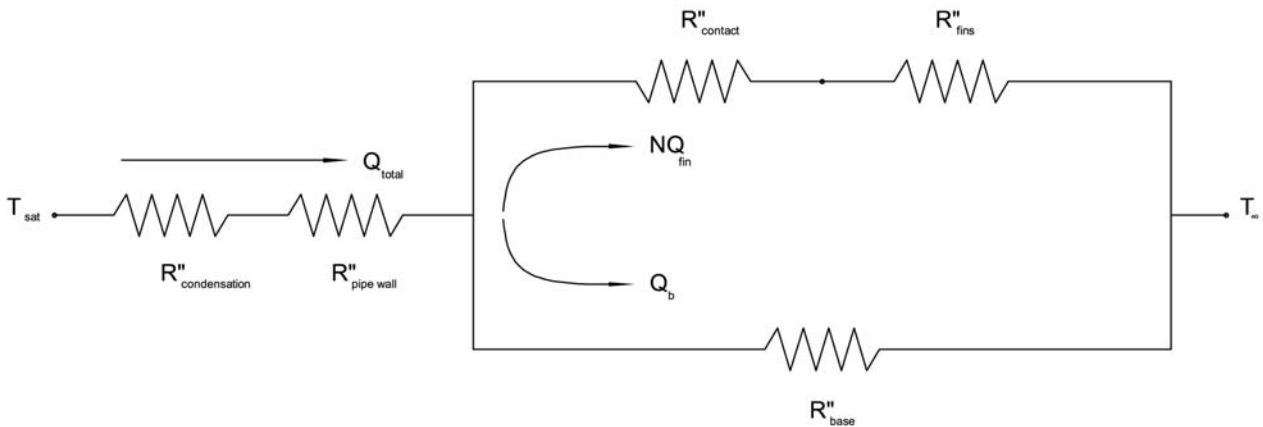


Figure 1-6. Thermal resistance inside the condenser.

As the heat transfers from the condensing fluid to the ambient air, several forms of resistance to heat flow are encountered. The vapor enters the condenser and condenses along the tube wall, $R''_{condensation}$. The latent heat is then conducted through the wall, $R''_{pipewall}$, to the fins where it passes through any added contact resistances that may result from the manufacturing

process, $R_{contact}''$. The forced air passing over both the fins, R_{fins}'' , and tube banks, R_{base}'' , allows the heat to dissipate to the ambient. The resulting thermal resistance is shown in Figure 1-6.

Several innovative techniques have been implemented over the years to significantly enhance heat transfer by reducing the thermal resistance. Starting with the manufacturing process, techniques such as electroplating and aluminum braising have been put into practice that minimize interfacial gaps that minimize the localized thermal resistance.

The liquid side heat transfer enhancement has been investigated by Zuo et al. (2000). Applicable to both the downflow and reflux configurations, Zuo shows that by adding drainage disks within the tube, the film thickness is reduced, allowing considerable improvement in the heat transfer. However, flooding within the channels becomes increasingly more significant because of the increased liquid entrainment. While proper drainage is highly beneficial to enhancing heat transfer, the added pressure drop that results close to the flooding limit within a reflux type condenser can make for a relatively inefficient process.

The highest thermal resistance found within an air-cooled condenser comes from the air-side heat transfer coefficient. Even with the extended fin surface, the heat transfer is still constrained by air-side limitations. By altering the geometry and generating turbulence, the thermal boundary layer can be interrupted, allowing adequate mixing between the plates and providing a significant increase in heat removal. Fin geometries such as louver, offset strip and wavy fins are among the geometries classified as “interrupted surfaces” that are commonly encountered in industrial applications due to the enhanced heat transfer performance, ease of fabrication, and low cost. Figure 1-7 shows the louvered fin geometry and the corresponding boundary layer thickness along the plate. This noticeable decrease in boundary layer thickness, keeps the ambient air well mixed, although the pressure drop is increased. Proper modeling tools

therefore require a firm understanding of the heat transfer capabilities as well as the pressure drop characteristics for a given system. Several papers in the open literature compare the heat transfer performance of plain fins versus louver or offset strip fins claiming a vast improvement in efficiency for the interrupted surfaces. In contrast, the performance of extended surfaces in the form of carbon or metal foams is not as frequently encountered in the literature. Therefore this study will focus on evaluating the heat transfer performance of carbon and metal foams for comparison with louvered fins.

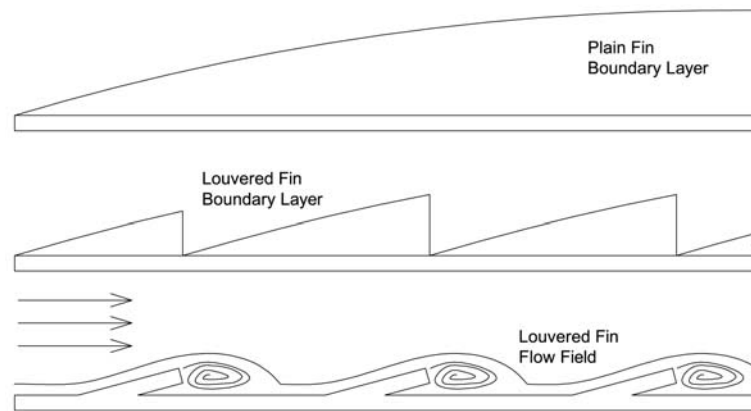


Figure 1-7. Flow field and boundary layer for louver type fins.

Due to the vast amount of experiments conducted on louver type fins, there have been several empirical correlations presented in the literature that provide reasonable accuracy. Wang et al. (1999), Chang et al. (1997) and Chang et al. (2006) have provided generalized heat transfer and friction correlations that are widely used and each has been tested against a large database consisting of 74, 91, and 91 data samples. The correlations were constructed from experiments in which the fin efficiencies are determined using the Schmidt (1949) approximation and the average local heat transfer coefficients are computed.

The idea of using foam materials to enhance heat transfer is a relatively recent concept. Lu et al. (2006) and Zhao et al. (2006) conducted a thermal analysis on a metal foam tube-in-

tube heat exchanger and compared it to that of a conventional uninterrupted finned tube heat exchanger. They conclude that the use of metal foams can significantly enhance the heat transfer performance when compared to conventional plain fin heat exchangers due to the increased surface area and mixing capabilities; however no information on pressure drop is provided. Boomsma et al (2003) conducted experiments using 50% water-ethylene glycol solutions and claim that for a given pressure drop, metal foams are capable of removing 2 or 3 times higher heat loads.

Implementing carbon foam into heat exchanger design has recently been investigated by Klett (2002). He demonstrates that the ligament conductivity of the carbon exceeds 1700 W/mK , compared to aluminum's 237 W/mK and copper 401 W/mK . High thermal conductivity foam drastically increases the fin efficiency and heat transfer rates. He shows that for a solid foam configuration, heat transfer rates compared to aluminum foams are enhanced by a factor of 10, while the pressure drop increases by a factor of 40. Other configurations such as through holes or fin shapes provide similar heat transfer results while detailed pressure drop data are not provided.

Instabilities and Subcooling

Several reviews on two-phase flow instability phenomena exist within the literature including Boure et al. (1973), Ishi (1970), Bergles (1977), Yadigaroglu et al. (1981), Fukuda & Kobori (1979), and Kakac & Bon (2008). A general classification for instabilities in forced convection two-phase flow systems is described in Table 1-2 (Boure et al. 1973).

A more detailed description of the various instabilities can be found in Boure et al. (1973). Numerous studies have been conducted to observe the mechanisms responsible for the onset of instability under natural circulation conditions (Kyung et al. 1996)(Aritome & Chang

1993)(Van Bragt, 1998)(Yang et al. 2005)(Durga Prasad et al. 2007)(Jiang et al. 2000). For natural circulation systems, Yang et al. (2005), Durga Prasad et al. (2007), and Jiang et al. (2000), describe natural circulation instability unique to passively driven flow. In this case the instability is first triggered by the static instability (Ledinegg) before becoming dynamic. After the flow excursion, dynamics are introduced in the form of both pressure drop (1995) and natural circulation instability. Pressure drop instabilities result from the added dynamics of a compressible volume within the system. Once the Ledinegg excursion takes place, the vapor or gas within the system is compressed, and the build up of pressure will cause the flow rate to increase again. The result is an oscillatory flow rate, or a dynamic state. Natural circulation instability results from added dynamics that arise when hydrostatic head replaces the pumping mechanism to drive the flow. Once a Ledinegg excursion occurs, the flow rate is decreased, causing an increase in void fraction. This in turn results in an increase in hydrostatic head causing the flow rate to increase and the cycle is repeated causing oscillations in flow rate. Both pressure drop oscillations and natural circulation instability occur as secondary phenomenon triggered by the static instability (Ledinegg). Tadrist (2006) provides a review on instability phenomena found in narrow spaces. He shows that instability can arise in small channels due to the onset of critical heat flux, CHF. The dryout and rewetting cycle of the heated surface can result in vapor recoil within the channel. Depending on the compressibility of the inlet zone of the channel and the magnitude of density oscillations, quasi-periodical pressure fluctuations are observed.

For ideal thermal management design in the case of a thermosyphon, one must pay close attention to system instability. By controlling the system pressure and bulk fluid temperature it is

possible to alter the point of instability or improve the heat transfer for flow rates encountered during stable operation.

Table 1-2. Various types of two-phase flow instability.

Static Instabilities	Dynamic Instabilities
Ledinegg instability	Density wave oscillations
Boiling crisis	Acoustic oscillations
Bumping, chugging, or geysering	Pressure drop oscillations
Flow pattern transition	Thermal oscillation
	Multi-channel instabilities
	BWR instabilities

As is well known for two-phase flow, the pressure drop can be double valued for a specified flow rate. This characteristic of two-phase flow can give rise to the Ledinegg instability. In a given system, there exists a critical vapor quality in which the friction in the system is significant enough to cause fluctuations in the flow rate, ultimately resulting in dryout and system failure. Joshi et al (2005) provide a numerical study on two-phase flow in a thermosyphon. They conclude that an increase in power or a decrease in subcooling results in a destabilizing effect on the natural circulation within the loop. He also concludes that the margin of instability increases for reduced riser height.

The problems that arise from this unstable flow structure makes reducing pressure drop on the liquid side critical for operation at high heat flux. By lowering the bulk fluid temperature entering the evaporator plate, it is possible to keep the vapor quality down and delay the onset of instability. On the other hand, decreasing the bulk fluid temperature requires a larger condenser or a more powerful fan.

Summary

Due to the demand for high efficiency energy conversion devices, there is current interest in improving the overall power and energy densities of PEM fuel cells. Major challenges arise

with respect to thermal management, and new techniques are needed to handle the high thermal loads introduced in high power density systems. The goal of this research is to construct a flow boiling microchannel thermosyphon system that can be integrated into a PEM fuel cell stack to improve the overall power/energy density of the cell. By successfully measuring and modeling the thermal-hydraulics of the system, this research should allow for future optimization of a microchannel thermosyphon facility for fuel cell thermal management applications.

CHAPTER 3 FLOW BOILING MICROCHANNEL EVAPORATOR AND THERMOSYPHON PERFORMANCE

Background and Objectives

Proton-exchange membrane (PEM) fuel cells have recently been the focus of intense research for mobility applications. When considering fuel cells for space applications Burke (2003) suggests that fuel cell development should focus on both *power density* and *energy density*. The added value potentially provided by fuel cells to space science missions takes the form of mass savings, volume savings or more power or energy at the same mass and volume when compared with battery energy storage. The basic operating principle of a PEM fuel cell is that hydrogen fuel is oxidized at the anode, thus liberating electrons and producing protons. The free electrons flow to the cathode through an external circuit and combine with the protons and dissolved O₂ to produce water and heat. The electric circuit is completed as the protons flow from the anode to the cathode through a solid electrolyte membrane. As elucidated by Djilali and Lu (2006) and Berning and Djilali (2003) several important coupled mass, momentum, and heat transport problems occur simultaneously within the fuel cell stack. Three particularly crucial issues that strongly influence PEM performance are: 1) thermal management, 2) water management, and 3) mass transport limitations. During current PEM operation, humidification of the reactant gas stream is used to control the membrane moisture content. At high current densities, product water is removed by air stream convection, and is controlled by adjusting pressure drop, temperature, and moisture content. Up to 50% of the heat generated during high current density PEM fuel cell operation must be removed to prevent dry out and excessive heating of the membrane, otherwise local degradation of the membrane will occur. The small temperature difference available between the fuel stack and the ambient environment renders

thermal management a very difficult issue. NASA Glenn has been developing unitized regenerative fuel cells for unmanned vehicle applications (Burke 2003). Currently the limiting factor to increasing the power density of their test fuel cell is an inability to remove the heat load at higher current densities (Bents, 2004). Burke (2003) is currently working to develop a loop heat pipe evaporator, where low temperature heat sinks are available. The more conventional approach to thermal management is to utilize forced convection of liquid coolant through the fuel cell stack (Zhang et al. 2004). A major concern in fuel cell operation is that the required pumping energy for the coolant flow reduces the net power output of the fuel cell (Wetton, 2004).

The objective of this work is to develop a flow boiling microchannel cooling plate that may be easily inserted into the stack of a PEM fuel cell for thermal control. The current thermal control system operates in the natural circulation mode where the flow is driven by two-phase density gradients. You and Liu (2002) have developed a two-phase flow transport model for the cathode side of PEM fuel cells. They have demonstrated that there exists an operating temperature for optimum performance. At low operating temperature the reduction reaction requires higher activation overpotential to produce the same current density. However, at higher temperatures the membrane resistance is higher. The optimum temperature tends to be in the range of 70-80 °C. Evaporative cooling inherently involves two-phase flow and changing flow regimes. The ideal configuration would utilize a cooling medium whose saturation temperature is approximately 10 to 20 degrees less than the optimum PEM stack operating temperature. Thus, once the PEM stack ramps up to its designed operating temperature, sufficient superheat will be available for boiling, and a naturally driven flow will be established. At steady-state, the flow rate is established by a balance of the pressure head and flow resistance. At higher heat

loads more evaporation will occur and establish a larger pressure head and flow resistance. The advantages of using phase-change for thermal management include: 1) the wall superheat associated with flow boiling does not change appreciably over a large change in heat flux, and thus the membrane temperature may be kept near the optimum, 2) natural circulation flow does not consume additional electric power to drive a pump, and 3) high heat fluxes may be achieved at low superheat, thus allowing for high power density operation. A potential disadvantage of operating in the natural circulation mode is that the flow is susceptible to a disrupting Ledinegg instability if the operating heat flux is too high.

This work describes the thermal hydraulic performance of a flow boiling microchannel cooling plate operating within a closed loop two-phase thermosyphon. The cooling medium used is HFE-7100 which has a saturation temperature of 61 °C at atmospheric pressure. Conventional flow boiling heat transfer correlations are found to be applicable to predict the wall superheat for an imposed heat flux in such microchannels. The mass flow rate through the thermosyphon can also be well predicted using standard macro-scale thermal hydraulic models. Although the Ledinegg instability could potentially limit satisfactory operation of the system at very high heat flux, the present flow boiling microchannel cooling plate is found to be suitable for high power density PEM fuel cell applications since it can already handle a significantly larger operating heat flux than currently encountered in industrial practice. This work should provide the tools necessary to accurately model the thermal hydraulics of the microchannel evaporator plate and give insight into the heat removal capabilities when integrated into a PEM fuel cell stack.

Experimental Facility

The experimental two-phase thermosyphon is shown in Figure 2-1. The main test section consists of a 56 channel aluminum cooling plate. Each channel has a cross section of 1 x 1 mm and has a length of 115 mm, (the 1 mm. x 1 mm. cross section of the channels are classified by Kandlikar (2001) as minichannels while Mehendal (2000) classifies these at the threshold of mesochannels and conventional channels).

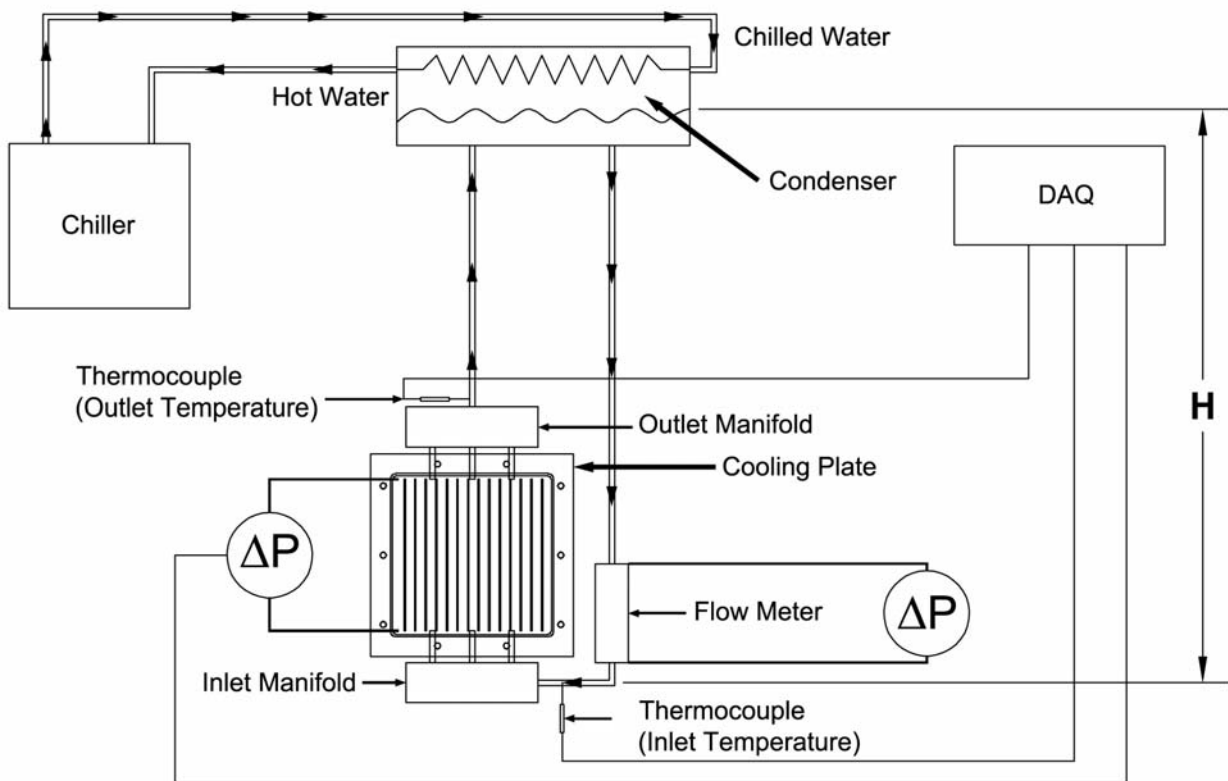


Figure 2-1. Experimental two-phase thermosyphon.

The cooling plate is covered with Lexan to allow for flow visualization. An imposed heat flux is placed on the cooling plate using a Minco foil heater, 127 mm X 127 mm, that covers the back of the cooling plate, and the maximum heater flux is 70 kW/m^2 , based on the surface area of the heater. The heated surface area in contact with the liquid is 193.2 cm^2 . During operation,

the cooling plate is thoroughly insulated with polyurethane foam insulation rated at a thermal conductivity of 0.04 W/mK . The temperature difference between the insulation and ambient is used to evaluate the heat loss, which is based on calibration. By taking direct measurements of voltage and current, the total heat input is determined. The heat transferred to the working fluid is taken as the difference between the total heat input and the heat loss.

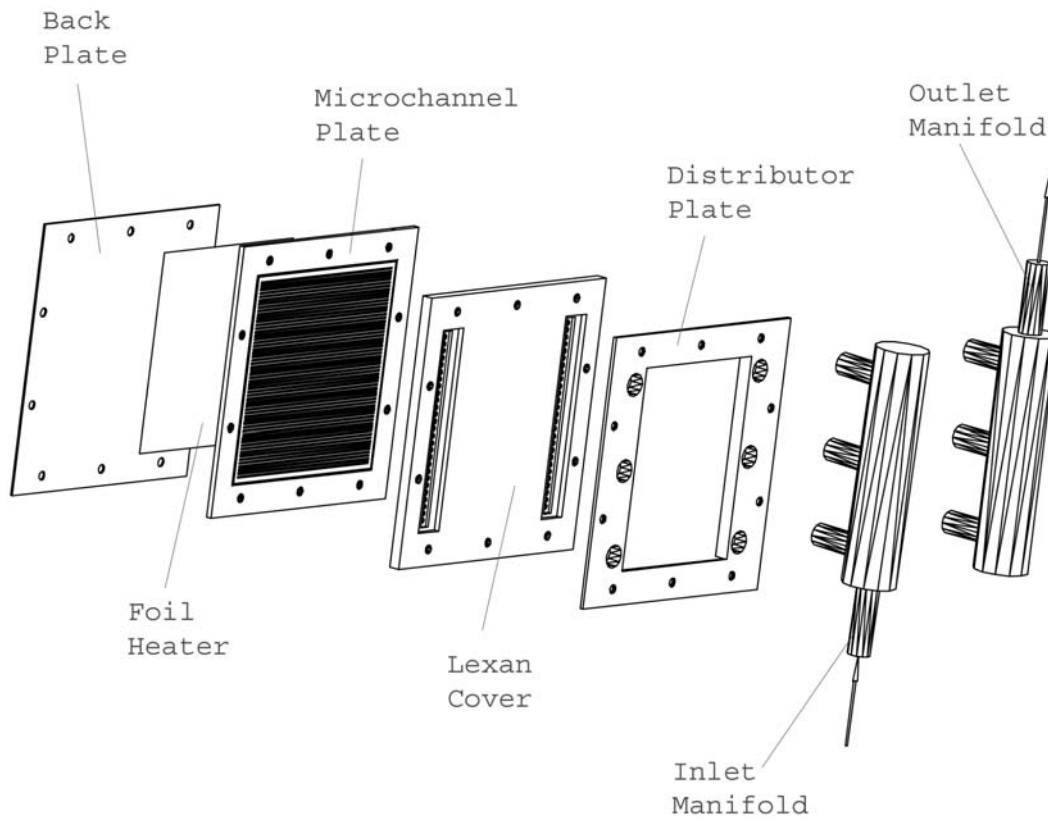


Figure 2-2. Exploded view of the cooling plate assembly.

An exploded view of the cooling plate assembly is shown in Figure 2-2. The facility is filled with HFE-7100 which enters and discharges the cooling plate through an inlet and outlet manifold, respectively. The two-phase mixture discharges the cooling plate and rises to a water cooled condenser operating at $15\text{ }^{\circ}\text{C}$ with a water flow rate of up to 43 g/s . The vapor is condensed, and the pure liquid phase flows out of the condenser and through a flow meter. The liquid discharge from the flow meter returns to the cooling plate. The inner diameter of the

tubing carrying fluid between the condenser and cooling plate is 9.5 mm. The vertical height between the condenser outlet and manifold inlet is 114 cm, while the vertical height between the outlet manifold and condenser inlet is 102 cm. The test section and piping throughout the system are insulated with elastomeric foam.

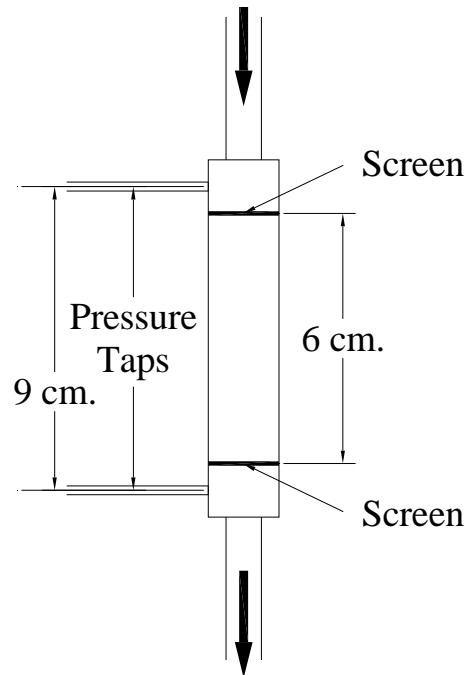


Figure 2-3. Section view of flow meter.

Since the facility operates in the natural circulation mode, it is important to have a flow meter that does not add a significant pressure drop. Therefore, a flow meter was fabricated using two 29 gauge screen meshes as depicted in Figure 2-3. The pressure drop across the screens is measured with a Validyne differential pressure transducer with a diaphragm capable of measuring a pressure drop up to 0.55 kPa. The maximum pressure drop recorded was 0.125 kPa which corresponds to a flow rate of 43 g/s. The relationship between flow rate and pressure drop was determined through calibration over a range of 50 g/s. The uncertainty of the flow rate measurement is explained in detail in Appendix-B.

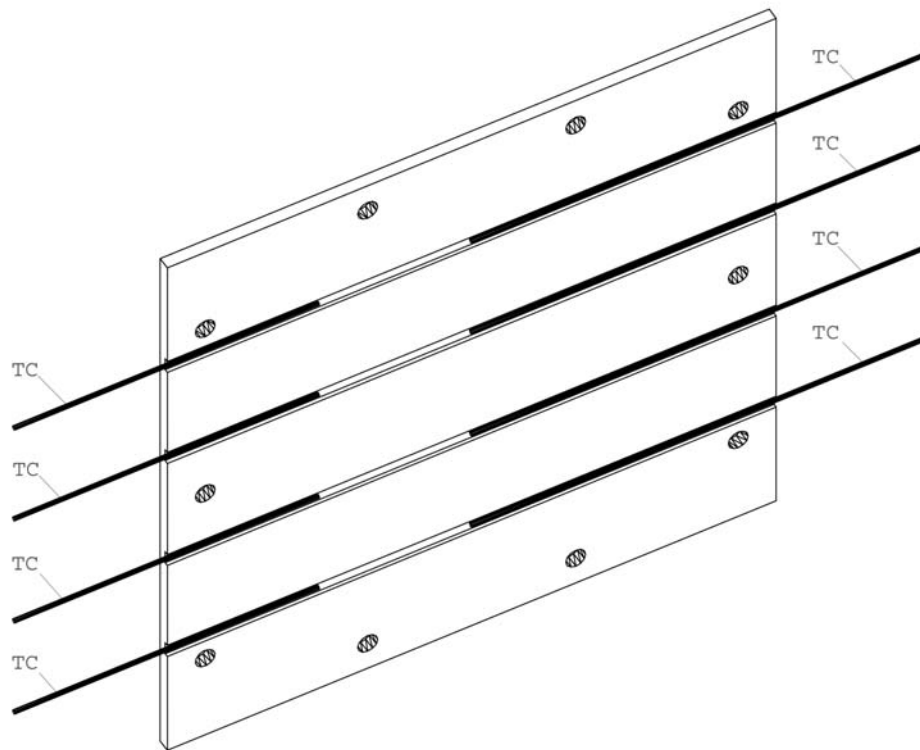


Figure 2-4a. Thermocouple locations on cooling plate.

A second Validyne differential pressure transducer is used to measure the pressure drop across the cooling channel and has a range of 0-3.5 kPa, respectively. Type E thermocouples have been inserted into the inlet and outlet manifolds to measure the fluid temperature. Also, 8 thermocouples have been embedded into the back of the cooling plate to measure wall temperature as depicted in Figures 2-4 a and b. The aluminum wall thickness between each thermocouple and the fluid is 1 ± 0.1 mm. The thermocouples were bonded securely using Omegabond-200 high thermal conductivity adhesive. Each thermocouple has been labeled 1-8 for reference. All calibrations and uncertainties are explained in detail in Appendix B.

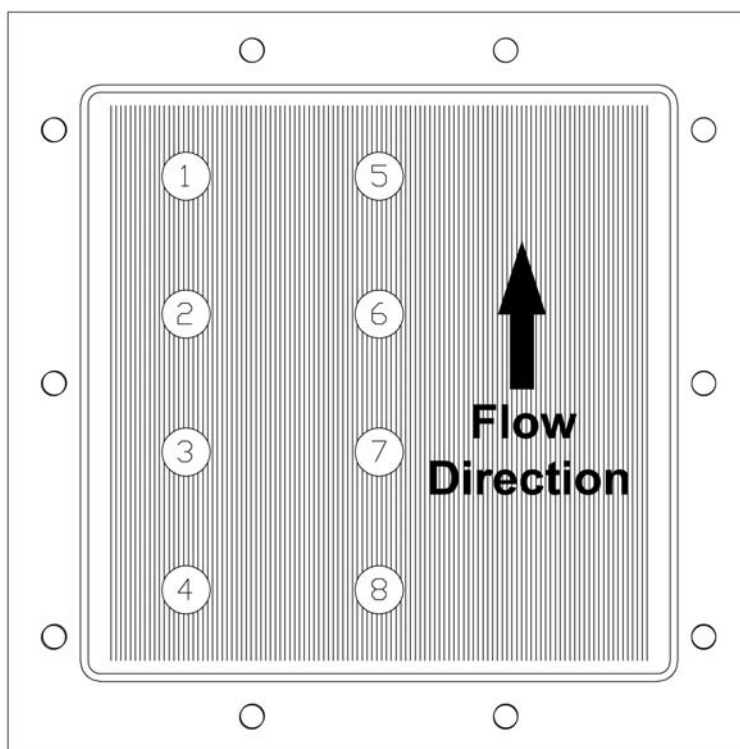


Figure 2-4b. Thermocouple locations on cooling plate.

All signals were measured using digital data acquisition consisting of a Measurement and Computing CIO-EXP32 multiplexer and PCIM-DAS1602/16 16 bit analog to digital converter. A custom algorithm was developed to convert the measured voltages to pressure, temperature, and flow rate, see Appendix B for more details.

Experimental Protocol

HFE-7100 is added to the facility through the top of the condenser until the height of the fluid is just below the condenser coil. Liquid water at 15°C is then circulated through the condenser coil. The differential pressure transducers are then purged of air. The heat flux on the cooling plate is gradually raised so that vigorous boiling is observed through the channels. Once vigorous boiling is established for a half an hour, the condenser is purged of non-condensable gas. Following purging, the heat flux is reduced to zero so that the flow through the facility

ceases. The heat flux is then raised in increments, and at each increment the flow rate and temperatures are allowed to reach a steady state. Measurements of pressure, flow rate, and temperature are made at each heat flux interval. The heat flux is raised until the flow becomes unstable, at which point large scale flow oscillations and flow reversal are easily visible.

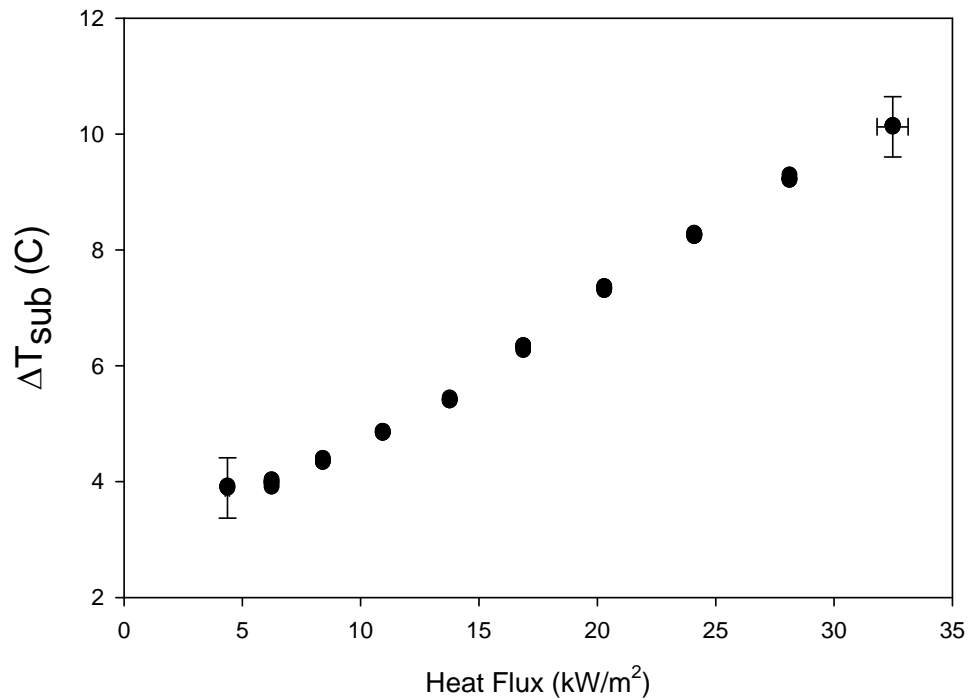


Figure 2-5. Degree of inlet sub cooling variation with heat flux.

The fluid leaving the condenser is subcooled to some degree. The degree of sub-cooling increases for increasing heat flux, as shown in Figure 2-5. The condenser coils are located above the liquid level within the condenser. When the vapor condenses, it is highly subcooled and mixes with the bulk liquid in the storage area. Therefore, as more vapor flows through the condenser, the bulk fluid becomes more subcooled.

Results

Figure 2-6 shows the measured flow rate circulating through the two-phase thermosyphon at various heat fluxes, (where the heat flux is based on the heated area in contact with the liquid). Initially, there is a rapid rise in flow rate with increasing heat flux. This rapid rise in flow rate is due to an increase in vapor volume fraction in the riser, and thus the density difference between the down flow line and riser increases, which results in an increased flow rate. As the heat flux increases further, the increase in vapor volume fraction is marginal, but the increase in vapor quality is significant which results in increased friction. Thus, the mass flow rate peaks at 43 g/s, corresponding to a heat flux of approximately 24 kW/m². As the heat flux is further increased, the mass flow rate decreases. The maximum achievable heat flux during these sets of experiments is 32 kW/m². At that point, the flow becomes unstable due to the onset of a Ledinegg instability.

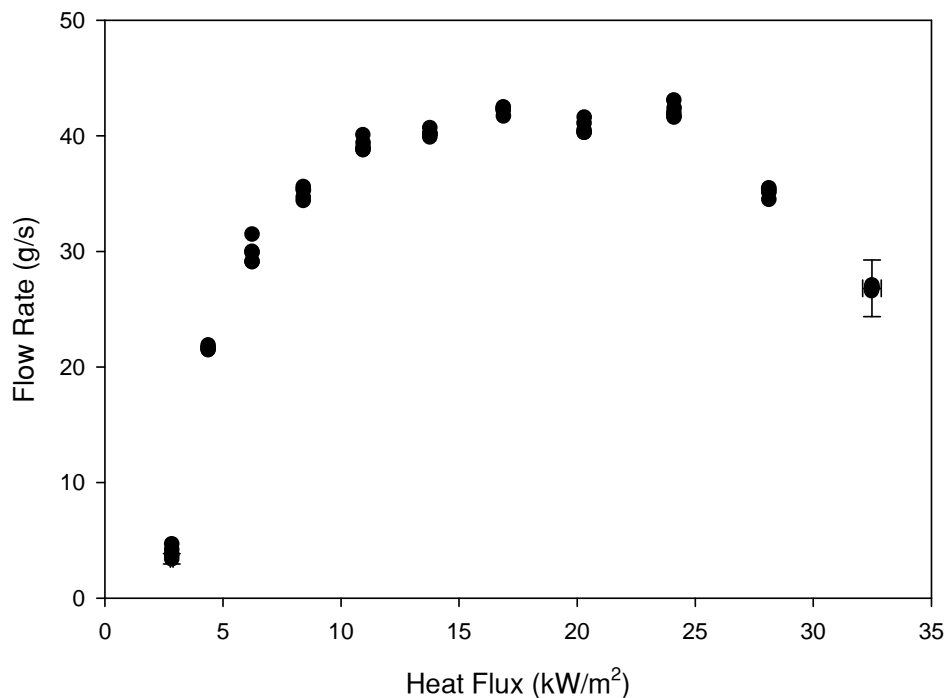


Figure 2-6. Variation of flow rate with heat flux.

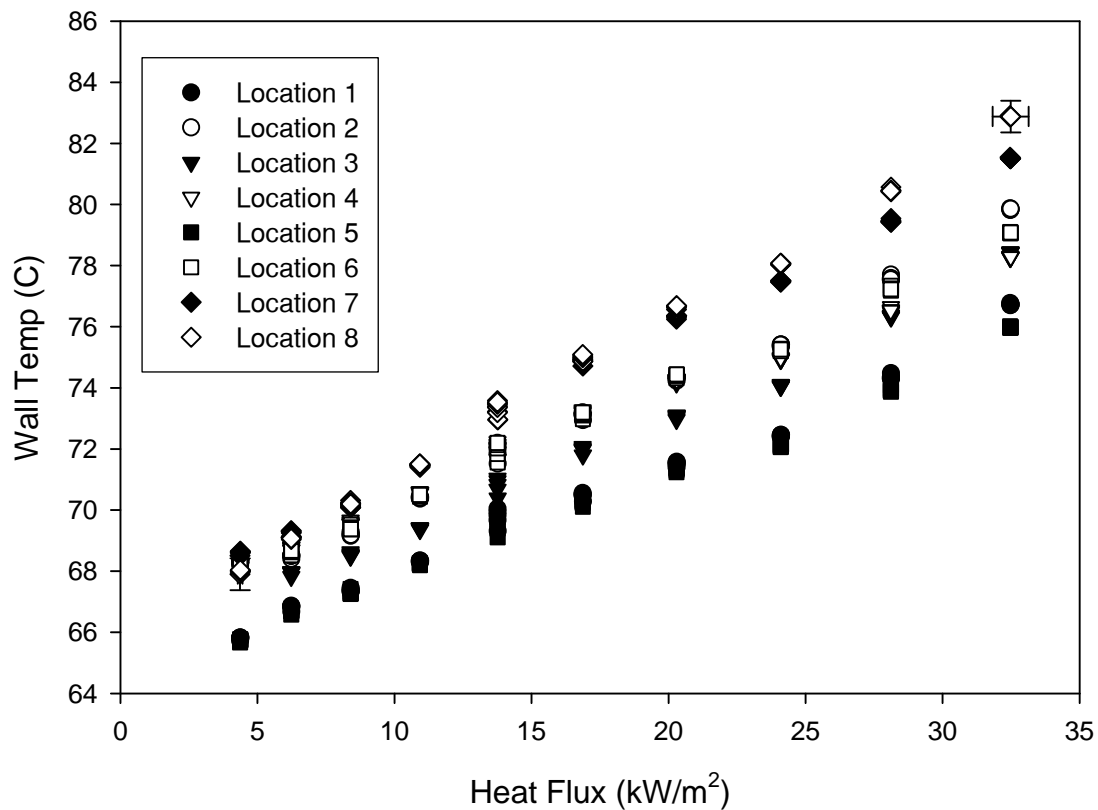


Figure 2-7. Wall temperature at various locations.

Figure 2-7 shows the measured wall temperatures for thermocouple positions 1-8 at various heat fluxes. The wall temperatures near the entrance to the cooling plate, which correspond to locations 4 & 8 from Figure 4b, tend to be the highest. This is because the fluid enters the cooling plate as a pure liquid, and the heat transfer coefficient is lower than that near the exit of the cooling plate, where the vapor quality is relatively high. Also, the wall temperatures are slightly less near the side of the plate than at the central region. This is due to the fact that there is finite heat leakage at the edges of the plate. In general, the thermal performance of the two-phase thermal management system is quite good. The wall temperatures of the cooling plate vary from approximately 66 to 82 °C depending on the heat flux and location. This is very close to the optimum temperature range for PEM fuel cell membranes.

Furthermore, PEM fuel cells currently only require a heat flux of 5 kW/m² (Lasbet, 2006) heat removal capacity. Therefore, the present system far exceeds the current need and has sufficient heat removal capacity for larger power density systems prior to the onset of Ledinegg instability. It should be noted, that the thermal performance of the system can be tuned by raising or lowering the height between the microchannel cooling plate and the condenser. Increasing the height will tend to increase the flow rate, and the vapor quality and heat transfer will adjust accordingly.

In order to elucidate how the variation of vapor quality influences the thermal field along the cooling plate, the axial variation of thermodynamic vapor quality is computed. Since the flow is subcooled entering the cooling plate, the change in sensible heat must be considered when evaluating the thermodynamic equilibrium vapor quality, $x(z)$, at any z-location along the cooling plate; therefore from an energy balance the axial vapor quality is computed,

$$x(z) = \frac{\dot{q}_z - \dot{m}C_p(T(z) - T_i)}{\dot{m}h_{fg}}, \quad (2-1)$$

where \dot{q}_z is the rate of heat flow into the cooling plate from the entrance to the z-location, $T(z)$ is the bulk fluid temperature at the z-location, T_{in} is the inlet fluid temperature, \dot{m} is the mass flow rate, and h_{fg} is the latent heat of vaporization for the fluid. In order to evaluate $T(z)$, the inlet and exit fluid temperatures are measured, and it is assumed that there is a linear change in the bulk fluid temperature along the z-direction. This assumption may not be exact, but since the maximum temperature change between the inlet and outlet is only 10 °C, it is acceptable for the estimation of the vapor quality $x(z)$. The non-uniform heating is apparent from the measured wall temperatures shown in Figure 2-7. The lateral heat flux toward the edges of the cooling plate is approximately 27% of the heat flux into the fluid. Figure 2-8 shows the variation of

vapor quality along the z-direction for various heat fluxes at the central region of the cooling plate. While the quality appears to be small for low heat flux, this approximation is based on thermodynamic quality and does not account for the localized subcooled boiling which produces net vapor generation at negative thermodynamic equilibrium quality. Also, the quality increases rather slowly for low heat flux. At higher heat flux, the flow begins to decrease in flow rate and a rapid increase in vapor quality is observed.

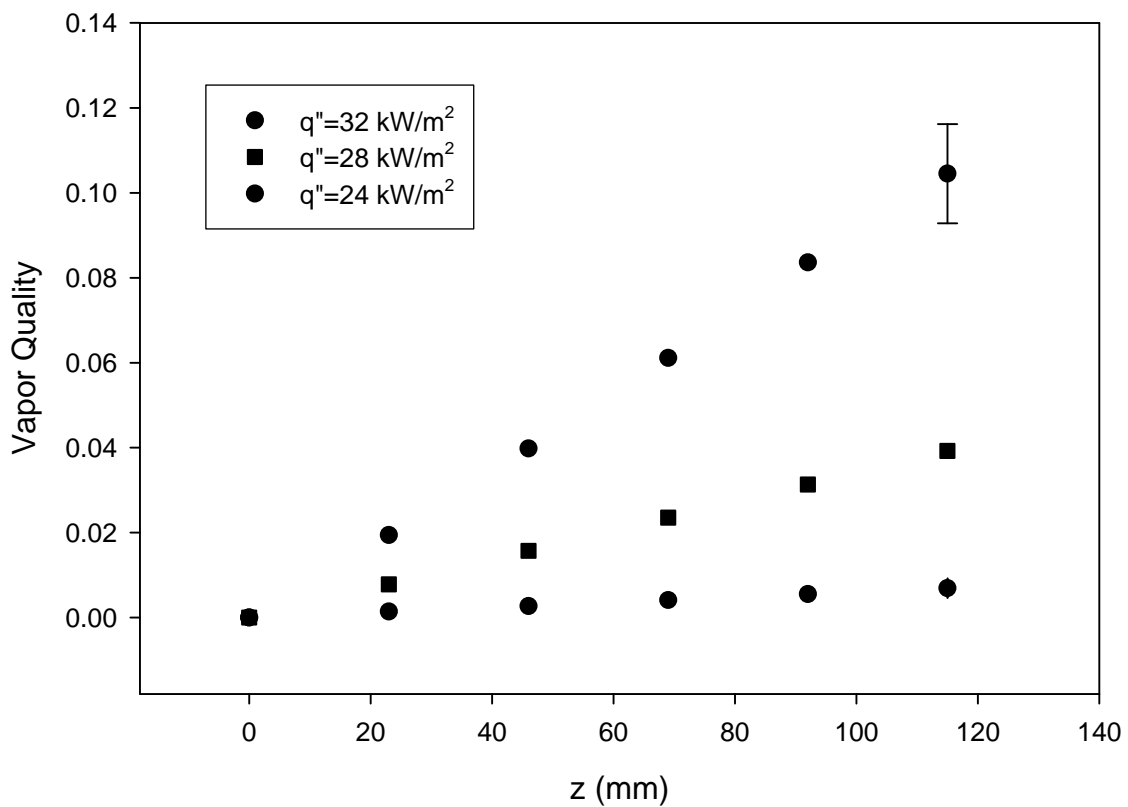


Figure 2-8. Variation in vapor quality with channel height.

Flow Modeling

In a closed loop natural circulation system, the pressure at the discharge of the condenser is the same as that at the return of the condenser. Therefore, in order to predict the system flow rate it is necessary to compute the pressure change around the flow loop and converge on a flow

rate that insures the inlet and discharge pressure at the condenser match. The two phase pressure gradient may be expressed as,

$$\left(\frac{dP}{dz}\right)_{2\phi} = \left(\frac{dP}{dz}\right)_g + \left(\frac{dP}{dz}\right)_f + \left(\frac{dP}{dz}\right)_a \quad (2-2)$$

It consists of three components, gravitational, frictional, and accelerational, denoted by subscripts g, f, and a respectively. Each must be modeled accordingly to ensure proper representation of the flow behavior. The gravitational pressure gradient results from a body force acting on the fluid and is given by,

$$-\left(\frac{dP}{dz}\right)_g = \rho_m g \sin \theta \quad (2-3)$$

where ρ_m is the mixture density, g is the gravitational acceleration, and θ is an inclination angle.

For upflow $\theta=\pi/2$ and $\theta=-\pi/2$ for downflow. The mixture density depends on the vapor volume fraction α ,

$$\rho_m = \alpha\rho_v + (1-\alpha)\rho_l \quad (2-4)$$

where ρ is the density and the subscripts l and v refer to the liquid and vapor, respectively. In order to estimate the vapor volume fraction, the standard Zuber-Findlay (1965) drift flux model for slug flow is used,

$$\alpha = \left(C_0 \left(1 + \left(\frac{1-x}{x} \right) \frac{\rho_v}{\rho_l} \right) + \frac{\rho_v}{Gx} V_{vj} \right)^{-1} \quad (2-5)$$

$$V_{vj} = 1.53 \left(g \sigma \frac{(\rho_l - \rho_v)}{\rho_l^2} \right)^{1/4} \quad (2-6)$$

where G is the mass flux and $C_0=1.2$. The pressure gradient associated with the acceleration of the fluid is derived from a momentum balance on a differential section of the tube in a constant

cross section. The resulting expression for the change in velocity due to the change in vapor quality and vapor volume fraction is,

$$-\left(\frac{dP}{dz}\right)_a = G^2 \frac{d}{dz} \left(\frac{(1-x)^2}{\rho_l(1-\alpha)} + \frac{x^2}{\rho_v\alpha} \right) \quad (2-7)$$

The frictional pressure gradient is modeled using the correlation from Mueller-Steinhagen and Heck (1986). This correlation considers the single-phase frictional pressure gradient for both liquid and vapor and uses superposition along with an empirical fit to model the two-phase frictional pressure gradient,

$$-\left(\frac{dP}{dz}\right)_f = F(1-x)^{1/3} + Bx^3 \quad (2-8)$$

$$F = A + 2(B-A)x \quad (2-9)$$

where the superficial velocity of the liquid and vapor phases is used to evaluate A & B as,

$$A = f_l \frac{G^2}{2\rho_l d} \quad (2-10)$$

$$B = f_v \frac{G^2}{2\rho_v d} \quad (2-11)$$

Here, d is the hydraulic diameter, and the Darcy friction factor is computed as,

$$f_l = \begin{cases} \frac{64}{\text{Re}_l}, \text{Re}_l < 1187 \\ \frac{0.3164}{\text{Re}_l^{1/4}}, \text{Re}_l > 1187 \end{cases} \quad (2-12)$$

$$f_v = \begin{cases} \frac{64}{\text{Re}_v}, \text{Re}_v < 1187 \\ \frac{0.3164}{\text{Re}_v^{1/4}}, \text{Re}_v > 1187 \end{cases} \quad (2-13)$$

$$\text{Re}_l = \frac{Gd}{\nu_l} \quad (2-14)$$

$$\text{Re}_v = \frac{Gd}{\nu_v} \quad (2-15)$$

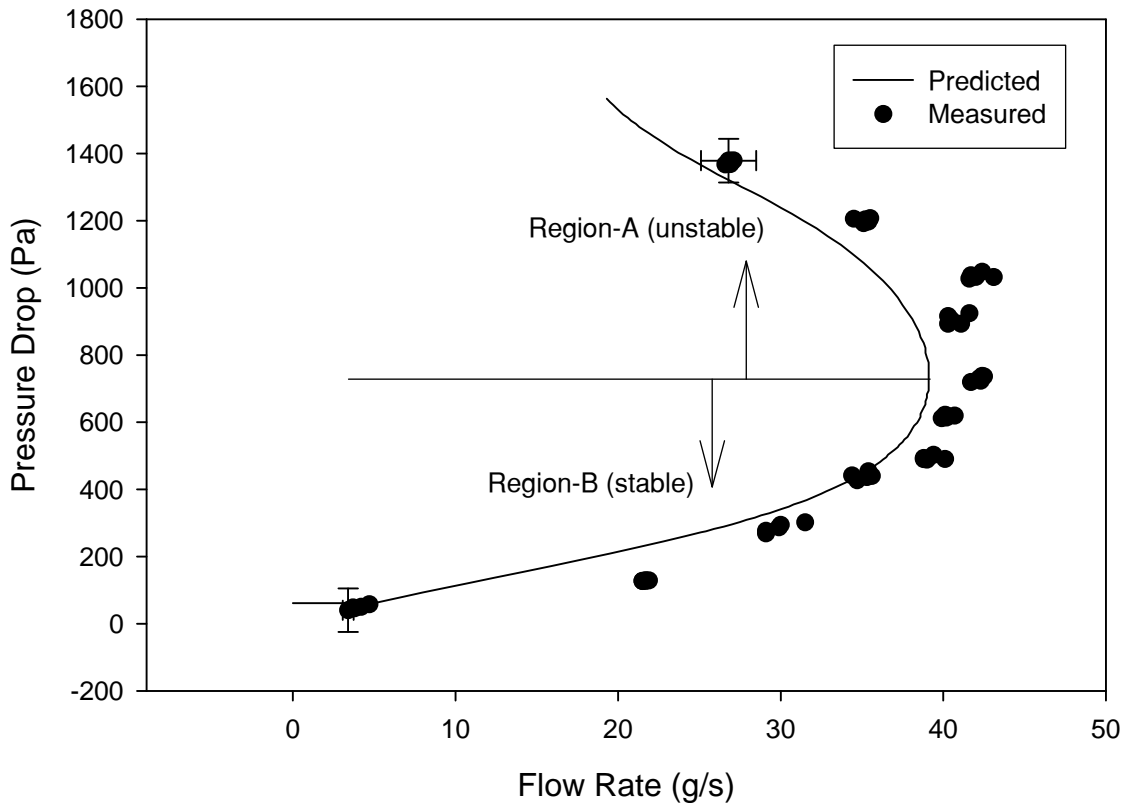


Figure 2-9. Measured and predicted microchannel pressure drop variation with flow rate.

At high heat flux the frictional pressure gradient within the microchannel plate is approximately 50 times the pressure gradient in the liquid section of the thermosyphon loop and 2.5 that in the two-phase upper section. To test the correlation of Mueller-Steinhagen and Heck (1986), the total measured pressure drop across the microchannel plate, which is dominated by friction, is compared against that predicted. As observed in Figure 2-9, the predicted pressure drop is in reasonable agreement with that measured. The model of Mueller-Steinhagen (1987), commonly used to predict 2-phase frictional pressure drop within conventional sized channels, is used here and found to be satisfactory. The 1 mm. x 1 mm. cross section of the channels under investigation are classified by Kandlikar (2001) as minichannels while Mehendal (2000)

classifies these at the threshold of mesochannels and conventional channels. Therefore it is understandable that the Mueller-Steinhagen model works well in predicting the frictional pressure drop in this configuration.

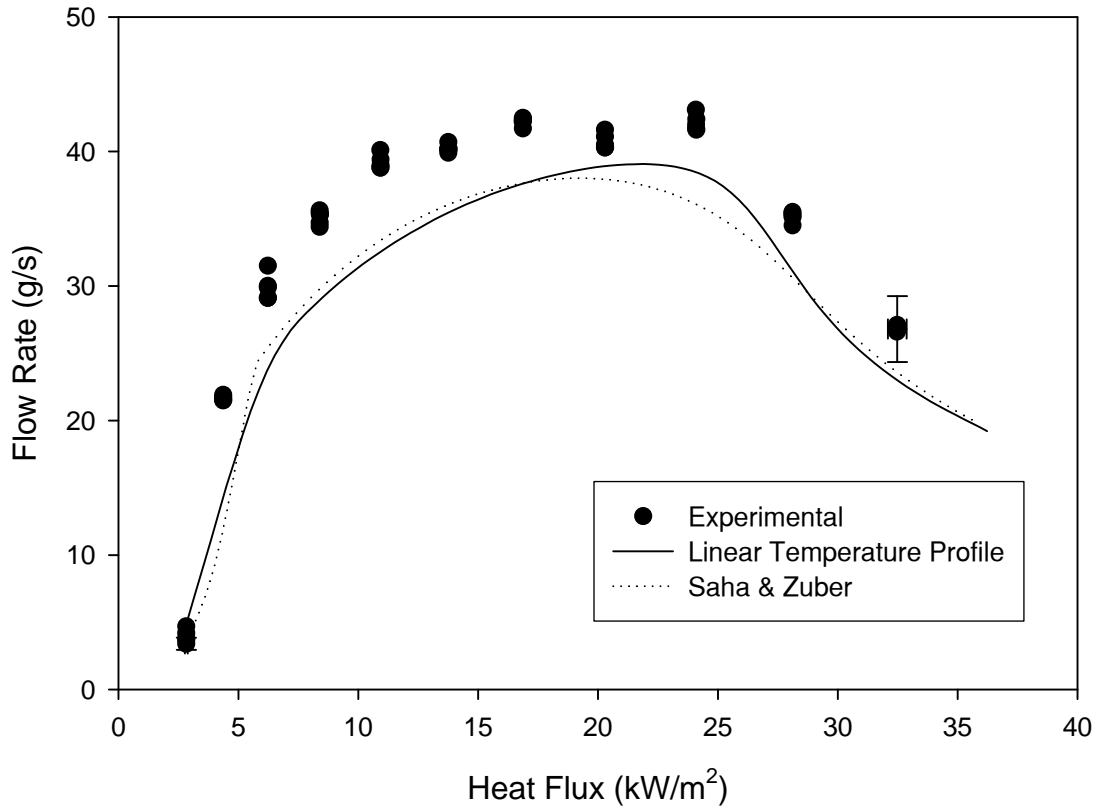


Figure 2-10. Comparison between measured and predicted flow rate.

As is well known for two-phase flow, the pressure drop can be double valued for a specified flow rate. This characteristic of two-phase flow can give rise to the Ledinegg instability. In region-I, where the slope of the pressure drop as a function of flow rate curve is positive, a small perturbation decreasing the flow rate will result in increasing vapor quality and larger gravitational pumping potential. Simultaneously, the frictional pressure drop decreases due to decreased flow rate, and thus the flow rate will adjust back to its original value.

Likewise, in region-I, the flow rate will return to its original value following a perturbation

increasing the flow rate. The flow resistance, defined as $R = \frac{\partial \Delta P}{\partial \dot{m}}$, in this region is positive,

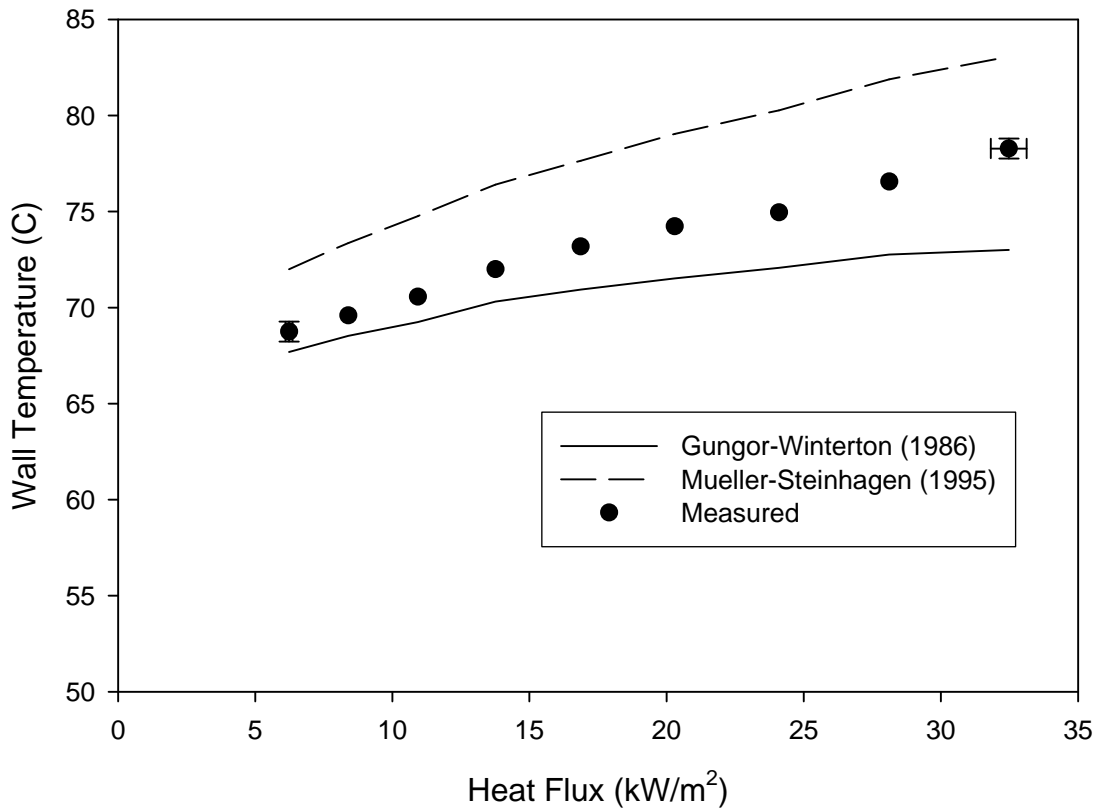


Figure 2-11a. Comparison between measured and predicted wall temperature at thermocouple location 5 based on measured flow rate and vapor quality.

thus the flow is stable in region-I. In contrast, in region II the slope of the pressure drop as a function of flow rate curve, R , is negative and a small perturbation increasing the flow rate will result in decreasing vapor quality and gravitational pumping potential. Simultaneously, the frictional pressure drop is reduced. Thus further increases in flow rate and decrease in vapor quality can result, until the flow swings back to region I. However, the flow state does not remain in region I for long due to the high heat flux and rapid increase in vapor quality. This behavior continues back and forth in an oscillatory mode until eventual dryout. In region-II,

where the resistance is negative, power is being produced instead of dissipated; therefore the possibility exists for unstable flow. In the current experiment, this oscillatory behavior was observed at a heat flux of 32 kW/m². Further explanation of the onset of Ledinegg instability for microchannel systems will be discussed in Chapter 4.

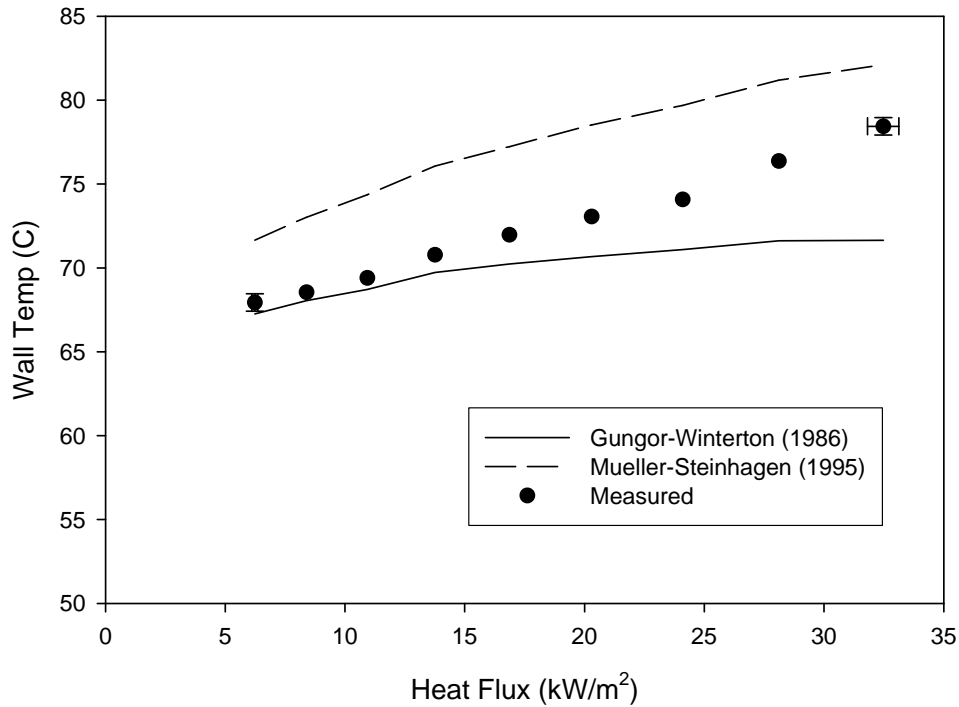


Figure 2-11b. Comparison between measured and predicted wall temperature at thermocouple location 6 based on measured flow rate and vapor quality.

In order to compute the mass flow rate for a specified heat flux, an algorithm has been developed that searches for the flow rate that yields an equal pressure at the inlet and exit of the condenser. Figure 2-10 shows a comparison between the measured and predicted mass flow rate at various heat fluxes assuming a linear bulk fluid temperature profile along the microchannel plate and a non-linear temperature profile using the Saha & Zuber (1974) correlation. Very little difference is observed between the two predictions. In general, the flow rate is slightly under-

predicted, but considering the complexity of the system, the predicted flow rate is satisfactory for design purposes.

Figures 2-11 a and b compare the measured wall temperatures at thermocouple locations 5 and 6, respectively, with those predicted using the Gungor-Winterton (1987) and Mueller-Steinhagen (1996) subcooled flow boiling correlations. The computations for these comparisons use the measured flow rate and vapor quality. The Gungor-Winterton (1987) correlation gives better agreement at lower heat flux and vapor quality, and in general the data lie between both predictions. The wall temperatures were also computed using the predicted mass flow rates, and the results are virtually identical to those shown in Figures 2-11 a and b. This indicates that the predicted wall temperatures are not sensitive to small variations in vapor quality and mass flow rate. It is also noteworthy that flow boiling correlations developed for large diameter tubes are also satisfactory for the current microchannel plate design. The thermal-hydraulic models presented in this work allow the thermal field in the microchannel plate to be predicted from fundamental models without the need for experimental inputs. While these correlations provide satisfactory results for the current configuration, it is unlikely smaller sized channels will be correlated accurately using the models discussed here.

CHAPTER 3 MICROCHANNEL PRESSURE DROP CORRELATION

Background and Objectives

A lot of attention has been paid to the two-phase flow pressure drop in small channels as the ability to fabricate flow channels at increasingly smaller sizes continues to improve. New technologies allowing fabrication of microchannels on the order of a few micrometers (Hwang) have found to be helpful in a variety of advanced applications including microelectro-mechanical systems (MEMS), fuel cells, electronics cooling, and others. In such applications, it is beneficial from a thermal management perspective to fabricate small channels due to an ability to yield high heat transfer coefficients and allow for a compact design. Since the reduction in channel size often leads to an undesirable increase in pressure drop, it is important to have an understanding of the transport phenomena governing pressure drop within these small channels. A limited number of work exists in the literature describing pressure drop in small channels (Lee & Lee, 2001) (Lowry, 1988) (Ide, 1990) (Wambsganss, 1991) (Wambsganss, 1992) (Mishima, 1993) (Fujita, 1995) (Mishima, 1996) (Kandlikar 2005) (Ribatski, 2006), while others exist for conventional channels (Muller-Steinhagen, 1986) (Friedal, 1979) (Lockhart & Martinelli, 1949). The goal of this work is to experimentally measure both the single phase and multi-phase pressure drop across a microchannel plate over a wide parameter space and compare against various pressure drop correlations available in the literature. This work is expected to contribute to the overall understanding of transport phenomenon within microchannels.

Experimental Facility

The experimental facility is shown in Fig. 3-1. The main test section consists of a 56 channel aluminum microchannel plate. Each channel has a cross section of 1 x 1 mm. and has a length of 115 mm, (the 1 mm. x 1 mm. cross section of the channels are classified by Kandlikar

(2001) as minichannels while Mehendal (2000) classifies these at the threshold of mesochannels and conventional channels). The microchannel plate is covered with Lexan to allow for flow visualization. A Minco foil heater, 127 mm. x 127 mm, is in direct contact with the bottom of the aluminum plate that provides a maximum heat flux of $70 \text{ kW}/\text{m}^2$. A micropump is integrated into the loop to allow for flow rate control. During operation HFE-7100 circulates between the microchannel plate and the condenser. A more detailed description of the experimental facility is given in Chapter 2.

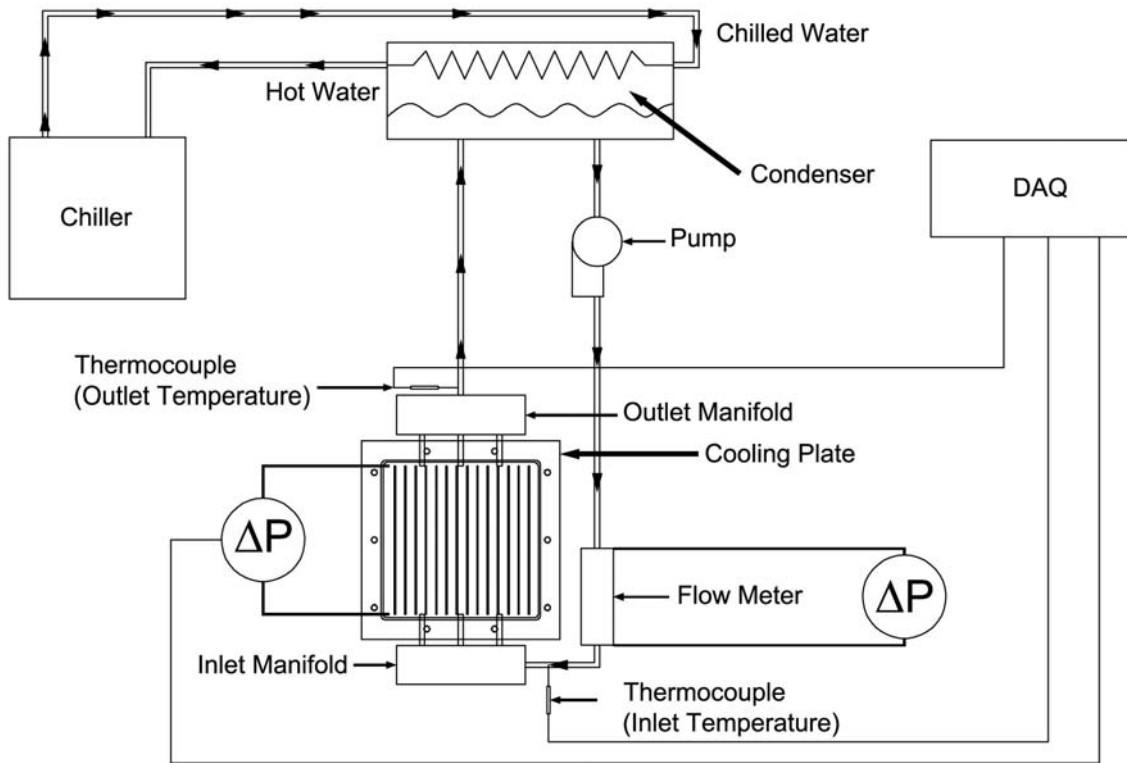


Figure 3-1. Thermosyphon experimental facility.

Experimental Protocol

During operation HFE-7100 is first added to the system until the liquid height is just below the condenser coils. All pressure lines are then purged of air to allow for accurate measurements.

The pump is then increased in increments to allow for flow through the system. At each increment of pumping power, the heat flux is also raised in increments to allow for varying vapor quality. By controlling both the pumping power and the heat flux, a large parameter space is obtained with respect to flow rate and vapor quality. At each increment, the pressure drop, flow rate, heat input, inlet temperature, and outlet temperature are recorded after the system is allowed to reach a quasi-steady state condition.

Results

The important parameters governing pressure drop aside from the geometric dimensions are the flow rate and vapor quality. During operation, the heat input, \dot{q} , flow rate, \dot{m} , inlet temperature, T_{in} , and outlet temperature, T_{out} , are directly measured. Using these direct measurements the vapor quality can be extracted at each axial location. First the temperature field is computed using the Saha-Zuber (1974) model for subcooled boiling. Once this is obtained, the variation in vapor quality in the axial direction is obtained from Eq. 2-1.

The next step is to extract the frictional component of pressure drop from the total pressure drop measurements that were measured directly. This is done by subtracting both the accelerational and gravitational pressure drops from the measured pressure drops as shown in Eq. 2-2. The details on computing both the accelerational and gravitational pressure drop are given in Eqs. 2-4 through 2-7. Table 3-1 summarizes the experimentally measured frictional pressure drop data for different heat inputs and mass flow rates.

Table 3-1. Frictional pressure drop data.

\dot{q}	\dot{m}	ΔP_f	T_{in}	T_{out}	\dot{q}	\dot{m}	ΔP_f	T_{in}	T_{out}
W	kg/s	Pa	°C	°C	W	kg/s	Pa	°C	°C
2.6	1.0	111	22.0	22.2	890.3	12.3	1069	47.8	60.8
2.6	1.0	116	21.9	22.1	0.5	0.4	34	21.3	21.6
57.3	4.7	123	47.4	56.8	0.5	0.5	35	21.4	21.6
57.3	4.9	36	47.4	56.8	11.3	1.7	19	30.8	36.7
147.4	21.7	370	56.7	61.7	11.2	1.7	19	30.9	36.7
208.4	25.8	627	56.2	61.5	28.6	2.5	46	40.3	49.6
208.4	25.7	630	56.3	61.5	54.9	6.8	20	52.3	58.9
276.5	27.1	801	55.1	61.0	54.9	6.7	20	52.3	58.8
276.4	27.1	800	55.2	61.1	91.2	15.3	285	56.7	61.0
350.8	27.2	922	54.1	61.0	91.2	15.3	286	56.6	60.9
350.8	27.3	918	54.2	61.0	148.9	20.8	627	56.9	60.9
441.0	26.5	1034	53.0	61.0	148.9	20.8	634	57.0	60.9
441.0	26.6	1035	53.0	61.1	0.3	0.6	26	21.7	21.9
533.9	24.7	1150	51.5	60.9	0.3	0.6	24	21.7	21.9
533.9	24.7	1152	51.5	60.9	208.6	21.9	756	56.0	60.6
645.5	21.6	1308	50.1	61.2	208.5	21.8	752	55.9	60.6
645.6	21.5	1309	50.1	61.2	278.0	22.0	856	54.9	60.6
738.8	18.2	1354	49.3	61.2	277.9	22.0	858	55.0	60.6
738.7	18.3	1354	49.3	61.2	345.0	21.5	930	54.0	60.7
861.2	14.7	1268	48.8	61.2	345.0	21.5	931	54.0	60.7
861.2	14.7	1266	48.9	61.2	435.8	20.5	1019	52.1	60.5
998.5	12.3	985	49.2	61.3	435.7	20.5	1018	52.1	60.5
998.5	12.2	982	49.1	61.3	523.9	18.5	1096	50.7	60.5
0.6	0.2	46	23.3	23.4	523.9	18.4	1100	50.7	60.5
0.6	0.2	45	23.3	23.4	626.6	15.8	1130	49.2	60.8
12.2	2.1	21	30.5	35.6	626.6	15.8	1132	49.2	60.8
12.2	2.1	21	30.5	35.6	749.4	12.5	1044	48.4	60.8
29.5	3.0	17	39.6	47.8	749.4	12.5	1043	48.5	60.8
29.5	3.0	17	39.5	47.7	773.8	12.0	1008	48.6	61.0
12.3	1.9	20	30.5	35.8	773.8	12.0	1009	48.5	61.0
12.3	1.9	20	30.5	35.8	12.1	1.6	18	30.8	37.2
26.9	2.6	14	39.4	47.9	12.0	1.6	18	30.8	37.3
26.9	2.7	14	39.4	47.8	23.9	2.9	14	40.9	50.8
57.5	6.6	24	50.7	58.1	23.9	2.1	9	40.9	50.5
57.5	6.4	19	50.7	58.1	48.4	6.8	21	52.1	58.5
95.9	15.6	178	55.8	60.5	48.4	6.8	22	52.2	58.5
95.9	15.6	158	55.8	60.6	4.1	0.6	197	22.6	22.4
147.8	22.0	501	56.4	60.8	4.2	0.5	197	22.6	22.4

Table 3-1 Continued.

\dot{q}	\dot{m}	ΔP_f	T_{in}	T_{out}	\dot{q}	\dot{m}	ΔP_f	T_{in}	T_{out}
<i>W</i>	<i>kg/s</i>	<i>Pa</i>	$^{\circ}C$	$^{\circ}C$	<i>W</i>	<i>kg/s</i>	<i>Pa</i>	$^{\circ}C$	$^{\circ}C$
203.2	24.2	692	55.8	60.7	94.0	16.5	429	56.2	60.0
203.2	24.2	691	55.8	60.7	139.2	18.1	636	55.7	59.8
271.6	24.8	836	54.8	60.6	139.2	18.0	642	55.9	59.9
271.5	24.8	836	54.9	60.6	193.0	18.9	743	55.2	59.8
352.4	24.8	944	53.8	60.8	193.0	18.9	741	55.2	59.7
352.3	24.8	937	53.9	60.8	3.9	0.4	192	22.7	22.6
432.8	23.9	1042	52.4	60.5	3.9	0.4	191	22.7	22.6
432.8	24.0	1044	52.4	60.5	337.6	18.1	874	52.3	59.5
540.6	21.7	1171	50.9	60.6	337.5	18.0	875	52.5	59.7
540.6	21.7	1167	50.8	60.6	431.4	16.6	940	50.6	59.8
656.2	18.4	1264	49.4	60.8	535.9	14.2	972	48.2	59.5
656.2	18.4	1262	49.4	60.8	535.9	14.1	973	48.2	59.5
780.1	14.7	1225	48.1	60.7	627.1	11.8	929	47.3	60.0
780.0	14.6	1225	48.1	60.7	627.0	11.8	931	47.3	60.0
890.4	12.3	1065	47.9	60.8					

Pressure Drop Correlations

Several correlations exist that describe two-phase pressure gradients for flow through channels. The conventional two-phase frictional pressure drop correlations considered here are those by Friedal (1979), Muller-Steinhagen (1986), and the homogenous approximation, while that of Lee (2001) is specific to small channels. The Muller-Steinhagen correlation is described in Eqs. 2.8-2.15, while those for Friedal, and Lee are shown below in Eqns. 3-1 through 3-23.

Friedal

$$\left. \frac{dP}{dz} \right|_f = \left. \frac{dP}{dz} \right|_l \Phi_{fr}^2 \quad (3-1)$$

$$\left. \frac{dP}{dz} \right|_l = \frac{2f_l}{d_h \rho_l} \dot{m}^2 (1-x)^2 \quad (3-2)$$

$$f_l = \begin{cases} \frac{16}{\text{Re}} & \text{Re}_d < 2000 \\ \frac{0.079}{\text{Re}^{0.25}} & \text{Re}_d > 2000 \end{cases} \quad (3-3)$$

$$\text{Re}_d = \frac{\dot{m}d}{\mu} \quad (3-4)$$

$$\Phi_{fr}^2 = E + \frac{3.24FH}{Fr_H^{0.045} We_l^{0.035}} \quad (3-5)$$

$$E = (1-x)^2 + x^2 \frac{\rho_l f_v}{\rho_v f_l} \quad (3-6)$$

$$F = x^{0.78} (1-x)^{0.224} \quad (3-7)$$

$$H = \left(\frac{\rho_l}{\rho_v} \right)^{0.91} \left(\frac{\mu_v}{\mu_l} \right)^{0.19} \left(1 - \frac{\mu_v}{\mu_l} \right)^{0.7} \quad (3-8)$$

$$We_l = \frac{\dot{m}d}{\sigma \rho_H} \quad (3-9)$$

$$\rho_H = \left(\frac{x}{\rho_v} + \frac{1-x}{\rho_l} \right)^{-1} \quad (3-10)$$

For $0 < Y < 9.5$

$$B = \begin{cases} \frac{55}{G^{1/2}} & G \geq 1900 \text{ kg/m}^2\text{s} \\ \frac{2400}{G} & 500 < G < 1900 \text{ kg/m}^2\text{s} \\ 4.8 & G < 500 \text{ kg/m}^2\text{s} \end{cases} \quad (3-11)$$

For $9.5 < Y < 28$

$$B = \begin{cases} \frac{55}{YG^{1/2}} & G \leq 600 \text{ kg/m}^2\text{s} \\ \frac{21}{Y} & G > 600 \text{ kg/m}^2\text{s} \end{cases} \quad (3-12)$$

For $Y > 28$

$$B = \frac{15000}{Y^2 G^{1/2}} \quad (3-13)$$

Lee

$$\left. \frac{dP}{dz} \right|_f = \left. \frac{dP}{dz} \right|_l \Phi_{fr}^2 \quad (3-14)$$

$$\Phi_{fr}^2 = 1 + \frac{C}{X} + \frac{1}{X^2} \quad (3-15)$$

$$X = \left(\frac{\left. \frac{dP}{dz} \right|_l}{\left. \frac{dP}{dz} \right|_v} \right)^{1/2} \quad (3-16)$$

$$C = A\lambda^q \psi^r \text{Re}_{lo}^s \quad (3-17)$$

$$\text{Re}_{lo} = \frac{G(1-x)d}{\mu_l} \quad (3-18)$$

$$\lambda = \frac{\mu_{l+}^2}{\rho_l \sigma d} \quad (3-19)$$

$$\psi = \frac{\mu_l u_v}{\sigma} \quad (3-20)$$

$$u_v = \frac{Gx(z)}{\rho_v} \quad (3-21)$$

$$\left. \frac{dP}{dz} \right|_l = \frac{2f_l}{d\rho_l} G^2 \quad (3-22)$$

$$\left. \frac{dP}{dz} \right|_v = \frac{2f_v}{d\rho_v} G^2 \quad (3-23)$$

After computing the frictional pressure drops using each correlation based on the experimentally measured flow rates and vapor qualities, predictions using each model are plotted against the experimentally measured values in Figs. 3-2 through 3-5. The mean relative error, defined as,

$$\varepsilon_{est_p} = \frac{\sqrt{\sum \left(\frac{\Delta P_m - \Delta P_p}{\Delta P_m} \right)^2}}{N}, \quad (3-24)$$

along with the maximum relative error are reported for each correlation in Table 3-2. As shown the Muller Steinhagen (1986) and homogeneous models have the lowest mean relative error while the homogeneous model provides the lowest maximum relative error. The microchannel frictional pressure drop correlation of Lee (2001) significantly over predicts pressure drop at high vapor quality while those for conventional channels provide better overall agreement. This observation however may not be applicable to smaller channels, as the 1 mm x 1 mm cross section of these channels is large enough where it may be modeled as a conventional channel under certain flow conditions, (the 1 mm. x 1 mm. cross section of the channels under investigation are classified by Kandlikar (2001) as minichannels while Mehendal (2000) classifies these at the threshold of mesochannels and conventional channels).

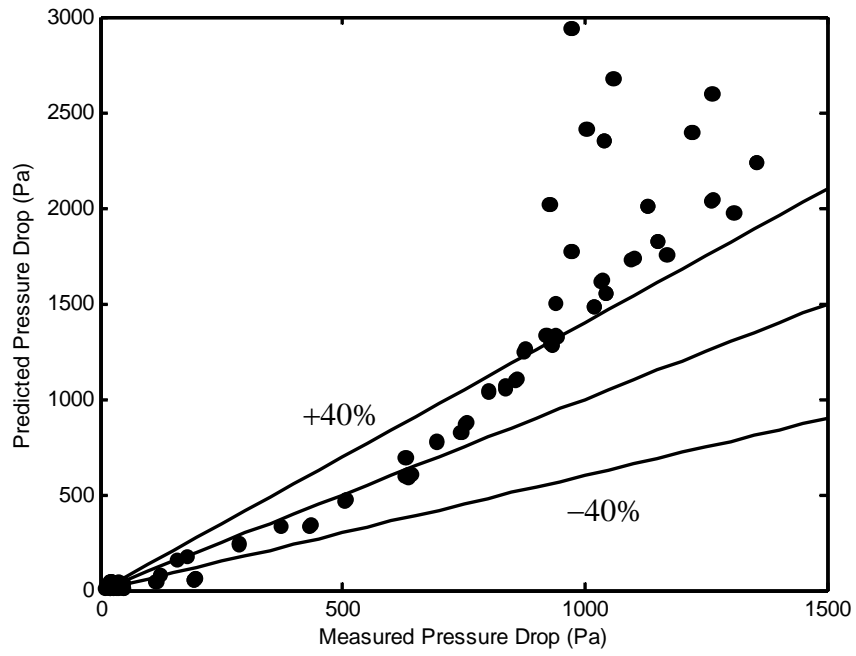


Figure 3-2. Experimental versus predicted frictional pressure drop using Friedal correlation.

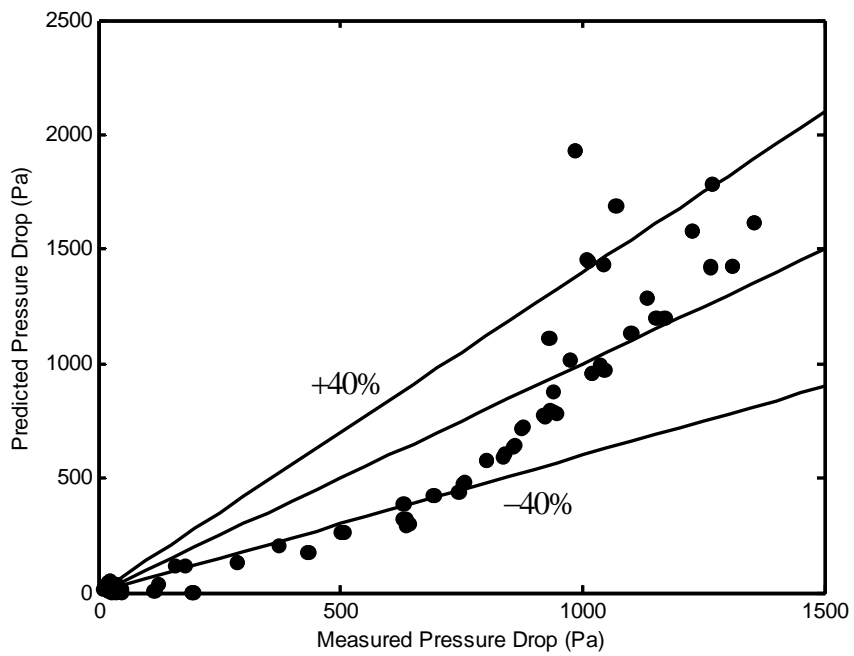


Figure 3-3. Experimental versus predicted frictional pressure drop using Mueller-Steinhagen correlation.

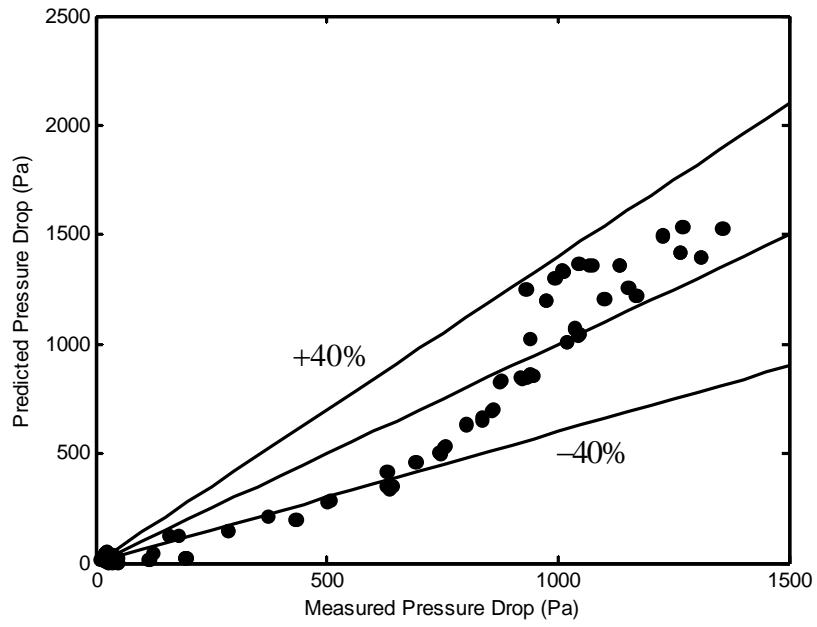


Figure 3-4. Experimental versus predicted frictional pressure drop using homogeneous model.

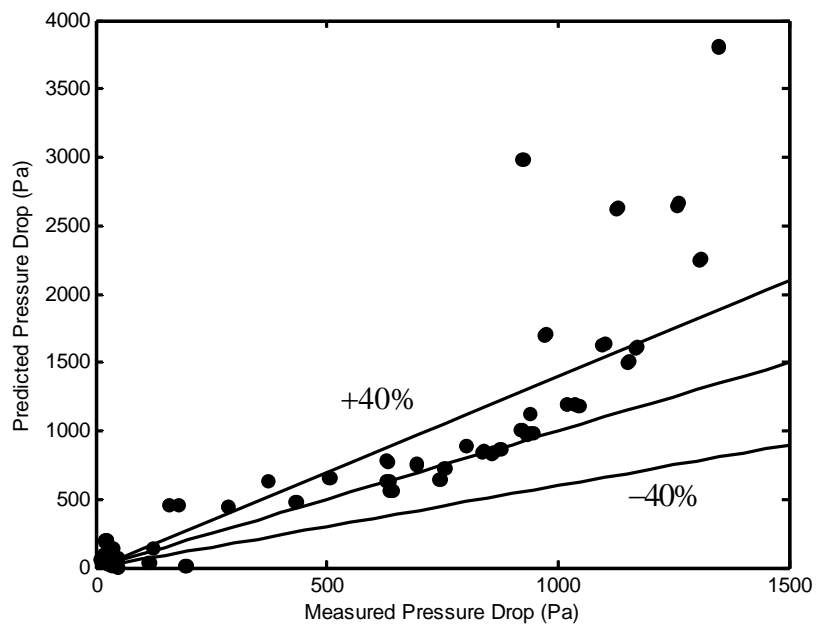


Figure 3-5. Experimental versus predicted frictional pressure drop using Lee correlation.

Table 3-2. Error between measured and predicted frictional pressure drop for various models.

Model	Max Relative Error	Mean Relative Error
Homogeneous	53%	21%
Freidal	318%	64%
Muller-Steinhagen	153%	27%
Lee	867%	82%

Conclusion

The frictional pressure drop has been experimentally measured for two-phase flow through a microchannel plate and compared against various correlations within the literature. The largest error occurs in the correlations obtained from experiment on pressure drop through small channels while the best correlations are those used for conventional size channels. Both the homogenous model as well as the frictional pressure gradient model of Mueller-Steinhagen provide the best overall agreement. Due to the chaotic nature of two-phase flow, along with the uncertainties that arise within small channels, the relative error is still quite large and further work should be done to better correlate two-phase frictional pressure gradient within small channels.

CHAPTER 4 INSTABILITY PHENOMENA IN A TWO-PHASE THERMOSYPHON

Background and Objectives

Two-phase flow system instabilities and thermo-hydraulic oscillations have long been of interest in the energy field since many steam generators operate in the natural circulation mode. The two-phase instability phenomenon was first reported by Ledinegg (1938) when investigating two-phase flow in steam generators. The onset of instabilities can be found in other applications involving passively driven two-phase flow systems, such as thermosyphons for electronic cooling and the present application, fuel cell thermal management. A number of reviews have considered two-phase flow instability phenomena, including those of Boure et al. (1973), Ishi (1970), Bergles (1977), Yadigaroglu et al. (1981), Fukuda & Kobori (1979), and Kakac & Bon (2008). Instabilities in forced convection two-phase flow systems can be categorized as static or dynamic. Static instabilities include Ledinegg, boiling crisis, flow pattern transitions, bumping, chugging, or geysering. Dynamic instabilities include density wave, acoustic, pressure drop, and thermal oscillations, in addition to multi-channel and BWR.

Boure et al. (1973) provides a more detailed description on the various instabilities reported. Numerous studies have been conducted to observe the mechanisms responsible for the onset of instability under natural circulation conditions (Kyung et al. 1996) (Aritome & Chang 1993) (Van Bragt, 1998) (Yang et al. 2005) (Durga Prasad et al. 2007) (Jiang et al. 2000). For natural circulation systems, Yang et al. (2005), Durga Prasad et al. (2007), and Jiang et al. (2000), describe instabilities unique to passively driven flow, which are initially triggered by the static Ledinegg instability prior to transitioning to a pressure drop (Lui et al. 1995) and natural circulation instability. Instability phenomena associated with two-phase flow through narrow spaces is described by Tadrist (2006). It is shown that instability can arise in small channels due

to the onset of local dryout. A more detailed explanation of the instability identification for the current study can be found in Appendix-A.

An experimental investigation that focuses on understanding and predicting the onset of instability within a two-phase microchannel thermosyphon facility is presented. Since it is a passive flow system, the emphasis is on the static Ledinegg instability. The experimental facility incorporates a fixed geometry with variable condenser height. The applied heat flux is the control variable, while the system flow rate is a dependent variable. Under these operating conditions, small scale flow perturbations that occur under quasi-steady state conditions are measured and used to predict the onset of instability. To validate these predictions, both the pressure drop as well as the limiting heat flux are compared against those determined experimentally. The limiting heat flux is satisfactorily predicted to within $\pm 10\%$ uncertainty. The uncertainty in the model prediction arises from uncertainties in the frictional pressure gradient and vapor volume fraction models.

Experimental Considerations

Facility

The experimental two-phase thermosyphon is shown in Figure 2-1. The cooling plate assembly includes 56 microchannels, 115 mm in length, and having a 1 mm x 1 mm cross section. A Minco foil heater is positioned on the backside of the microchannel plate and provides a maximum uniform heat flux of $70 \text{ kW}/\text{m}^2$. A lexan cover plate is stacked on top of the microchannels and allows for flow visualization. During operation, HFE-7100 circulates between the cooling plate and condenser. The condenser may be raised or lowered in order to change the gravitational head driving the flow through the facility. A more detailed description of the experimental facility is reported in Chapter 2.

Experimental Protocol

The condenser is positioned above the evaporator plate at one of four different heights considered for this investigation, 1.33, 1.15, 0.97, & 0.79 ± 0.02 m. HFE-7100 is first added to the system until the liquid height is just below the condenser coils. All pressure lines are then carefully inspected for air bubbles, followed by the purging of all pressure transducers. A heat load is applied to the evaporator plate to generate vigorous boiling. The pressure release valve, located at the top of the condenser, is opened to purge all non-condensable gas from the system and improve condenser performance. The heat load is then reduced to zero so that the flow through the facility ceases. The heat flux is raised in small increments. At each increment the flow rate and temperatures are allowed to reach a quasi-steady state. Measurements of pressure, flow rate, and temperature are made at each heat flux interval. The heat flux is raised until large scale flow oscillations and flow reversal are easily visible; it is this flow condition that is deemed as unstable. The condenser height is then repositioned and the experiment is repeated.

System Subcooling and Manifold Pressure Drop

The temperature of the working fluid leaving the condenser is subcooled to some degree. At relatively low heat flux where no boiling takes place, the fluid is significantly below the saturation temperature, $\Delta T_{\text{sub}}=10\text{-}40\text{ }^{\circ}\text{C}$. With a heat load of approximately $5\text{ kW}/\text{m}^2$, vapor bubbles are observed in the riser. The vapor enters the condenser and back into the bulk liquid. Fig. 2 shows the degree of subcooling measured for each heat flux and condenser height considered. At higher heat flux more vapor comes in contact with the coils, and as the heat flux is increased, the degree of subcooling becomes larger. Since the degree of subcooling affects vapor generation, the onset of instability depends on the inlet temperature to the evaporator.

Measurements of subcooling have been made at each heat flux interval, and are shown in Figure 4-1.

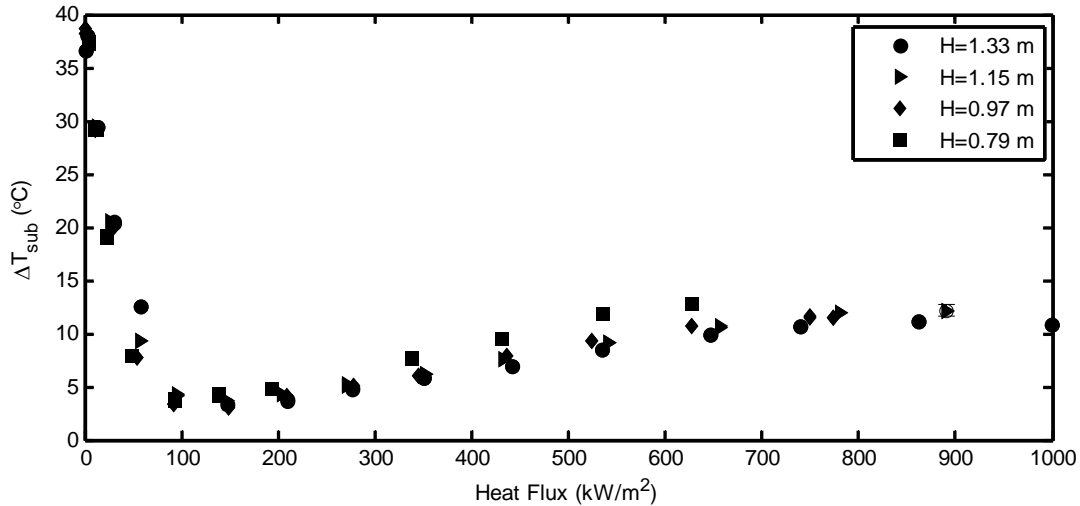


Figure 4-1. Variation of inlet subcooling with heat flux.

The pressure drops across the evaporator plate manifolds contribute significantly to the total pressure drop in the riser portion of the thermosyphon. Since the manifold design is unique to this experiment, direct measurements of pressure drop have been made at each heat load interval and condenser height and are shown in Figure 4-2. The pressure drop through the inlet manifold correlates with liquid velocity and that for the exit manifold correlates with vapor superficial velocity and are shown in Figure 4-2. The vapor superficial velocity is,

$$u_v = \frac{Gx(z)}{\rho_v}, \quad (4-1)$$

where G is the mass flux, $x(z)$ is the vapor quality at an axial location along the evaporator plate and ρ_v is the vapor density. The vapor quality is determined from Eq. (2-1). The vapor quality is determined at the exit of the evaporator plate using the measured exit temperature of the bulk fluid, T_e in order to compute the exit manifold superficial velocity. As shown the inlet manifold pressure drop is larger than the outlet manifold where two-phase flow is present. For

simplification, the pressure taps for the inlet manifold were located so that the pressure drop across the flow meter could be included in the measurement. It should also be noted that the pressure loss across the inlet manifold shown in Fig. 4-2 includes a small amount of tubing and a 90 degree bend.

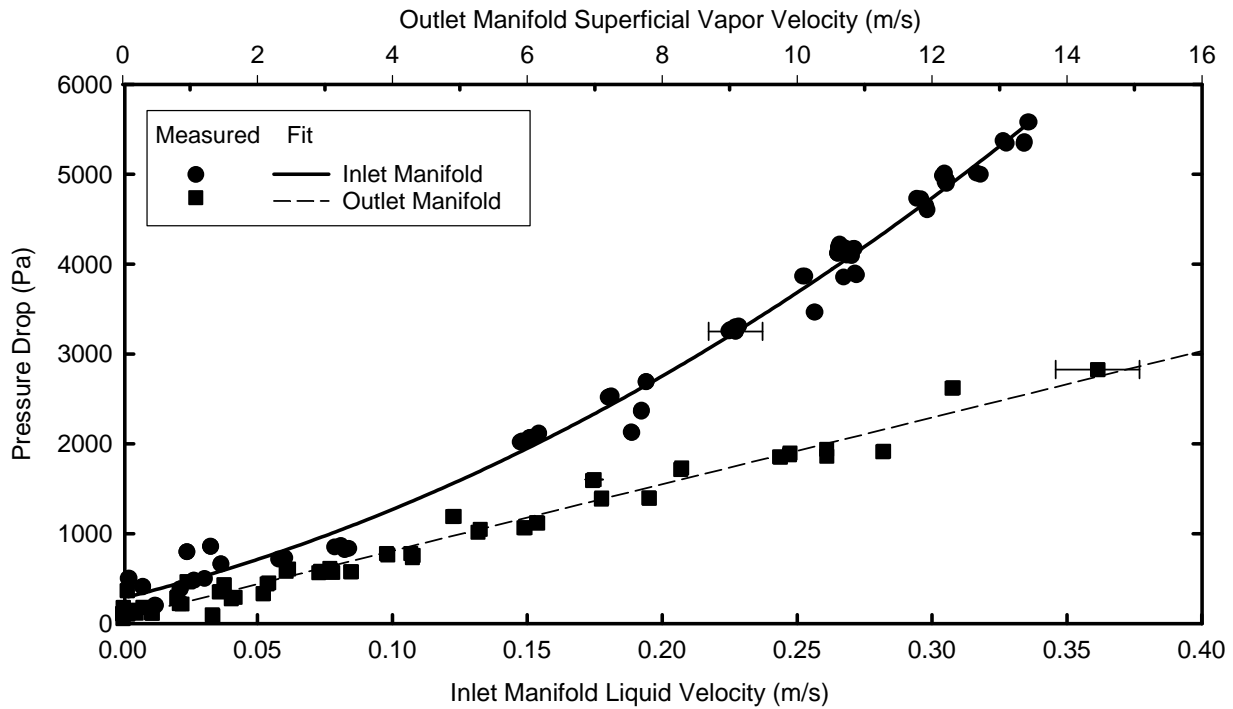


Figure 4-2. Pressure drop across inlet and outlet manifolds.

Flow Modeling

To predict the flow rate circulating through the thermosyphon loop, the momentum equation is used to compute the pressure gradient. The two-phase pressure gradient is comprised of three components: that due to gravity, friction, and acceleration denoted by the respective subscripts g , f , and a in Eq. 2.2.

In the case of a closed circulation loop, the difference in pressure between the discharge and return of the condenser is considered negligibly small. Therefore computing the pressure field throughout the thermosyphon loop allows determination of the mass flow rate, \dot{m} . The

flow rate is computed as that which gives the same pressure at the inlet and outlet of the condenser. The gravitational pressure gradient component depends on the liquid-vapor mixture density and the gravity vector is defined in Eq. 2.3 where ρ_m is the mixture density, g is gravity, and θ is the inclination angle with respect to the horizontal. The mixture density is given in Eq. 2-4. The vapor volume fraction, α , is estimated using the Zuber-Findlay (1965) drift flux model for slug flow is shown in Eqs. 2-5 through 2-6. Here $C_0=1.2$ is the distribution parameter. A momentum balance on a differential element is used to determine the accelerational pressure gradient component as described in Eq. 2.7. As suggested by Garrity et al. (2007), the frictional pressure gradient is computed using the Mueller-Steinhagen and Heck (1986) correlation found in Eqs. 2.8–2.11. Here d is the hydraulic diameter and the Darcy friction factors are computed as shown in Eqs. 2.12–2.15.

To compute the local vapor quality, $x(z)$, from Eq. 2.1, the temperature field, $T(z)$ is computed using the Saha-Zuber (1974) model for subcooled boiling. Using Eqs. 2.1-2.15 and the empirically determined pressure drop across the manifolds, the change in pressure from the condenser discharge to the inlet is computed. The mass flow rate is taken as that which yields no net change in total system pressure, ΔP_s . This is expressed as

$$\Delta P_s = \oint \frac{dP}{dz} \Big|_{2\phi} dz = 0. \quad (4-2)$$

Experimental Results

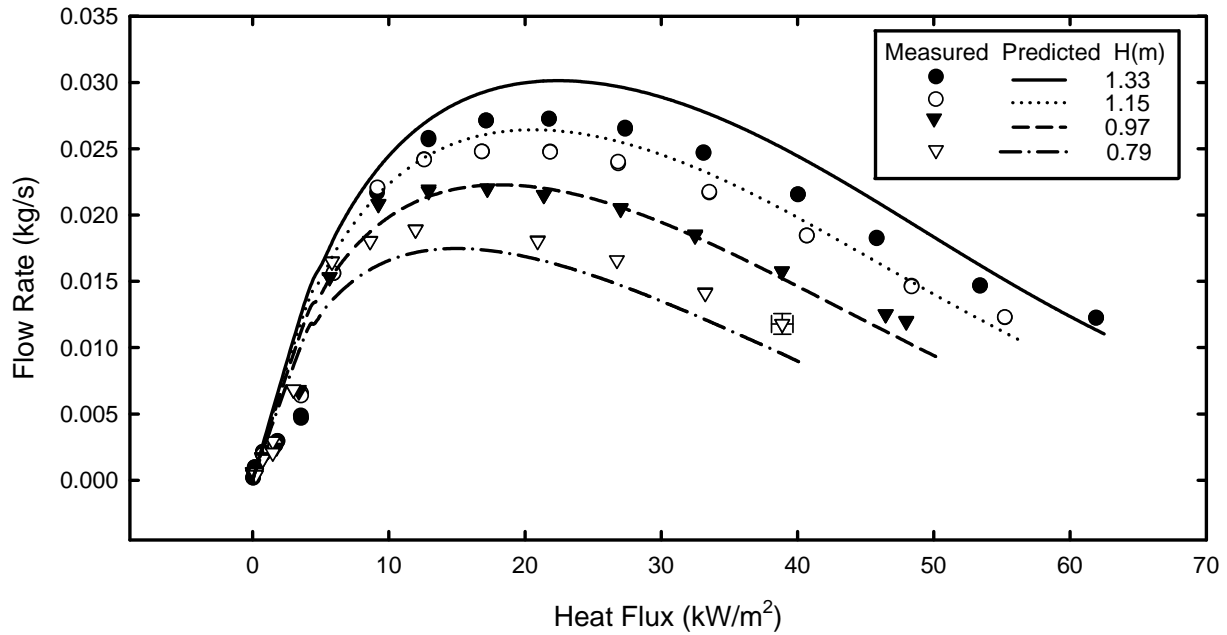


Figure 4-3. Mass flow rate variation with increasing heat flux.

The variation of the steady state mass flow rate of HFE-7100 circulating through the two-phase thermosyphon system with various applied heat fluxes is shown in Figure 4-3 for different condenser elevations. At low heat loads the flow rate increases rapidly with increasing heat flux due to the increasing difference in pressure head between the riser and downcomer. This increase in pressure head results from the increasing vapor volume fraction. At slightly higher heat flux, the vapor quality becomes more significant and an increase in frictional pressure drop is observed. As the frictional pressure drop becomes more substantial, the flow rate begins to decrease. Although the mixture density in the riser is low, the high velocity and frictional dissipation results in a decreasing flow rate. The largest flow rate occurs when the condenser elevation above the microchannel evaporator plate is highest. This is because a larger difference in pressure head between the riser and downcomer is achieved when the condenser elevation is largest. The pressure drop variation across the microchannel plate with respect to mass flow rate

is shown in Figure 4-4. For $H = 0.97$ m and $H = 0.79$ m, the predicted pressure drop decreases with increasing flow rate under relatively low heat flux. This is a result of operating at low vapor quality, where the frictional pressure drop approaches that of single phase flow. Also at low vapor quality, the vapor volume fraction increases significantly with small changes in quality, and the gravitational change in pressure drop is smaller at higher volume fraction. Thus a decrease in pressure drop is predicted. Given the complex nature of two-phase flow, the pressure drop prediction across the microchannel plate is considered to be in reasonable agreement with the measured data.

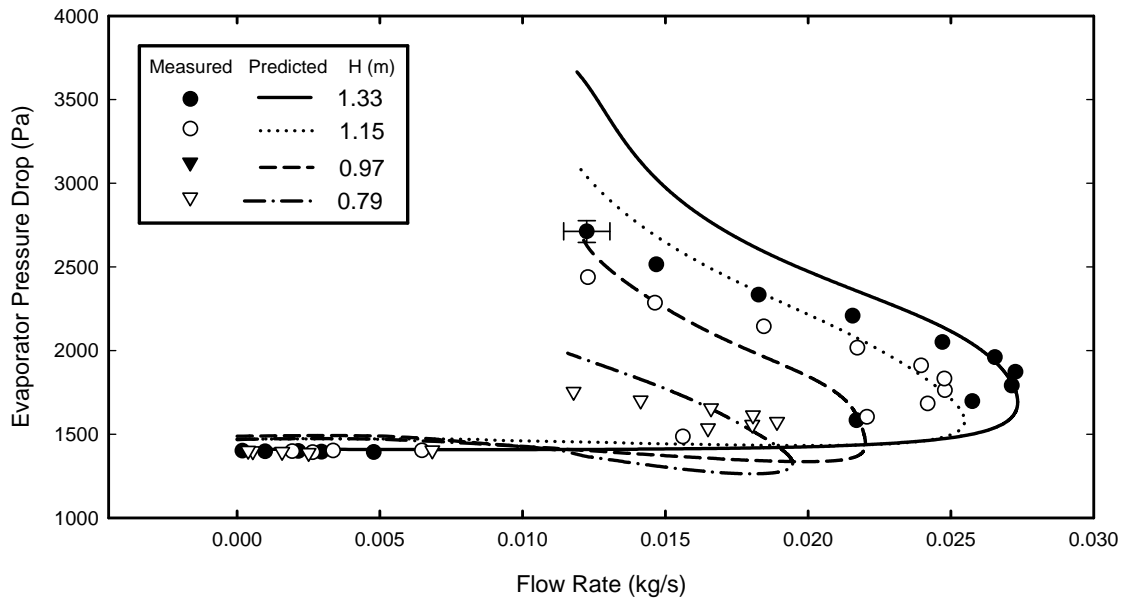


Figure 4-4. Pressure drop variation across the microchannel evaporator plate with respect to mass flow rate.

The reported uncertainty associated with the two-phase frictional pressure drop computed with the Mueller-Steinhagen and Heck (1986) correlation is approximately $\pm 41\%$, while the uncertainty associated with the void fraction computed with the Zuber-Findlay (1965) correlation is approximately $\pm 2.5\%$. In order to determine the uncertainty bounds of the mass flow rate predictions, the mass flow rate is computed using the upper and lower bounds of the frictional

pressure drop and vapor volume fraction. Figure 4-5 shows the upper and lower bounds of the predicted flow rates for $H = 1.33$ m and $H = 1.15$ m. The measured flow rates are compared with those predicted bounds. Only two condenser elevations are presented for discussion purposes. As shown, the measured flow rates generally fall within the predicted bounds, thus providing further confirmation that the agreement between the measured flow rates and those predicted is reasonable.

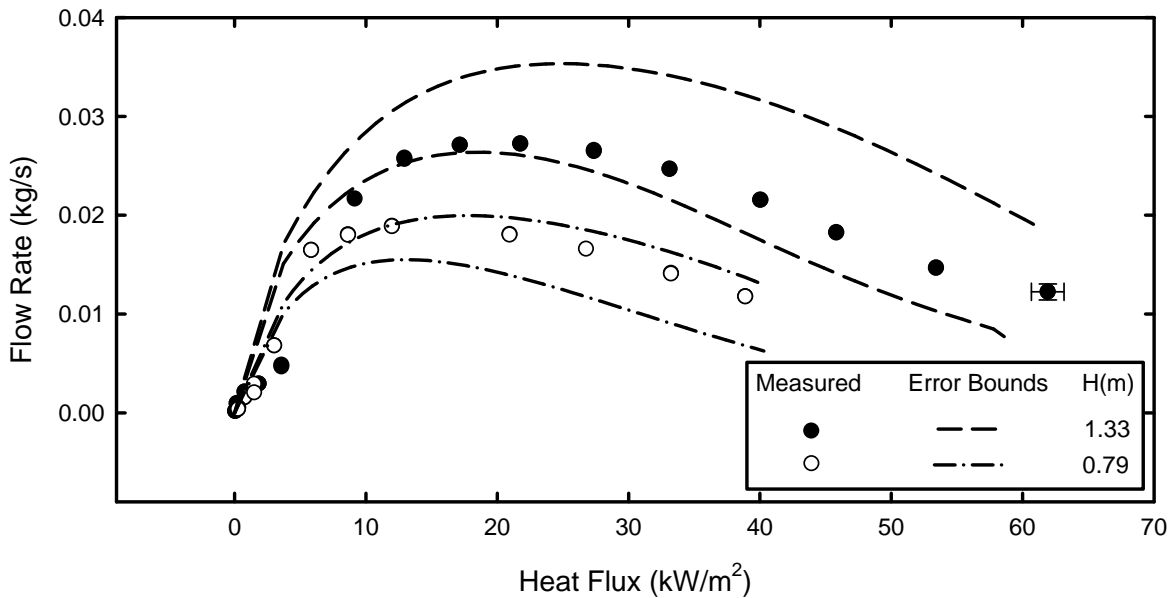


Figure 4-5. Upper and lower bounds for predicted mass flow rates for $H = 1.33$ m and $H = 0.79$ m.

Table 4-1. Experimentally observed limiting heat flux.

Condenser Height, H (m)	Limiting Heat Flux, q_{lim} (kW/m^2)
0.79	61.91
0.97	47.98
1.15	55.20
1.33	61.91

The heat fluxes shown in Figure 4-3 range from zero to a maximum value, at which point the system goes unstable. The system limiting heat flux for each condenser height is tabulated in

Table 4-1. As observed, the limiting heat flux increases with increasing elevation of the condenser above the microchannel evaporator plate.

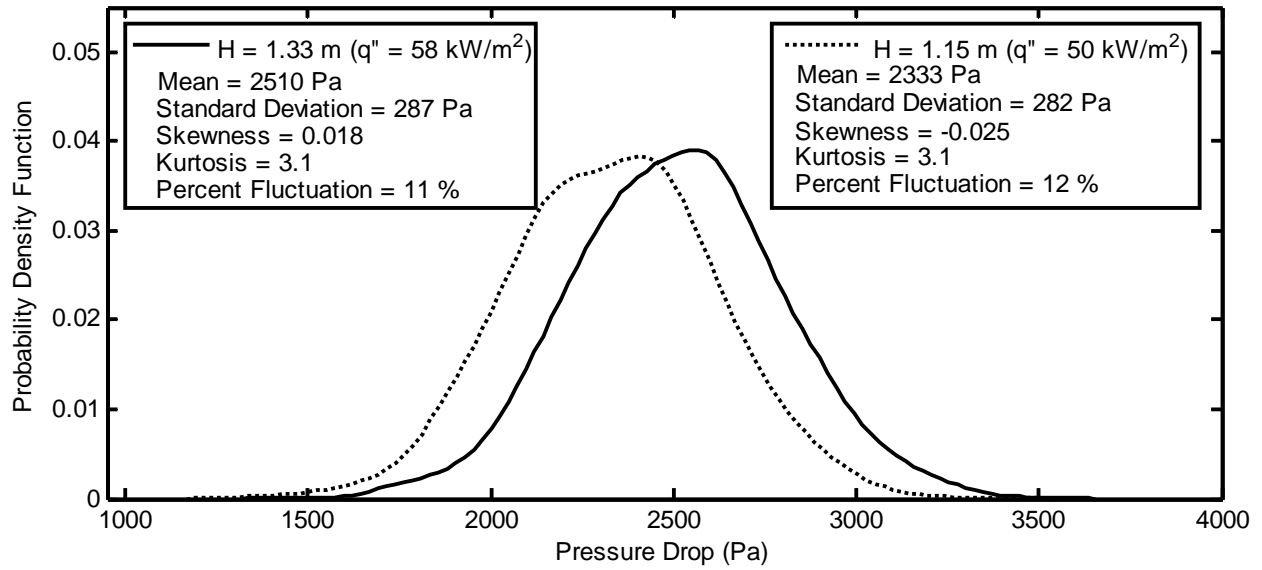


Figure 4-6. Measured probability density function for pressure drop prior to unstable flow.

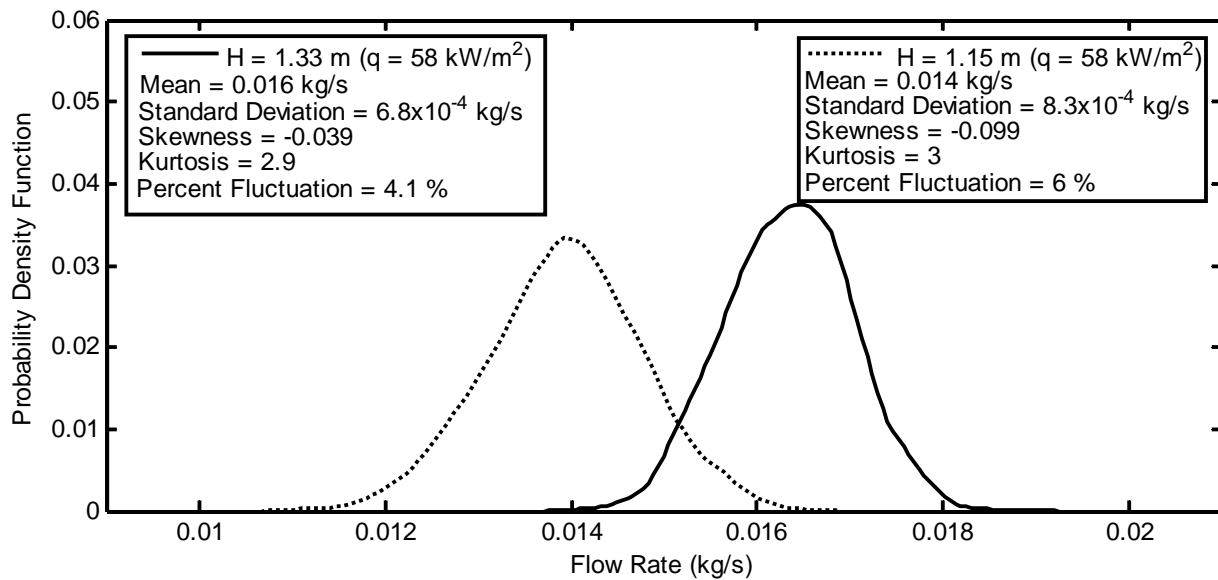


Figure 4-7. Measured probability density function for mass flow rate prior to unstable flow.

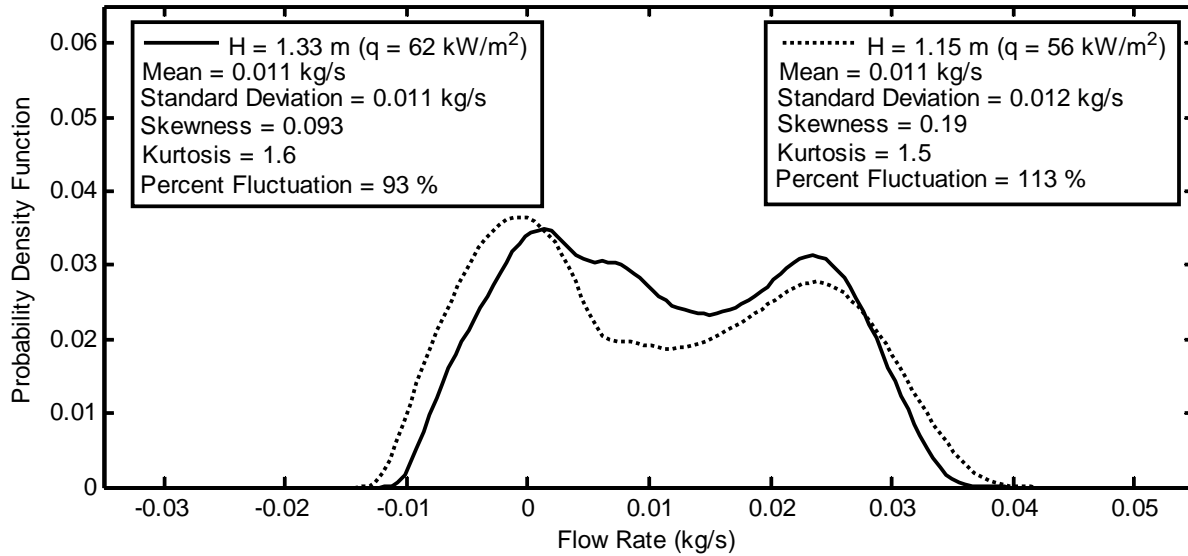


Figure 4-8. Measured probability density function for mass flow rate following the onset of unstable flow.

While the quasi-steady mass flow rate and pressure drop are very important variables for understanding the response of the system to step increases in heat flux, apparent random variations about the quasi-steady variables are equally important. It is the variation from the quasi-steady state that can send the two-phase thermosyphon into an unstable operating mode. Therefore, the stochastic variations in pressure drop and flow rate are examined. Figures 3-6 & 4-7 show the probability density functions for both the pressure drop and flow rate immediately prior to encountering the flow instability for both $H = 1.33$ and $H = 1.15$. In each case the skewness is almost zero and the kurtosis is near to three, suggesting the distribution is close to normal. The percent fluctuation, defined here as the ratio of the standard deviation to the mean, is 11% for the pressure drop and 4.1% for the flow rate for $H = 1.33$ m. For $H = 1.15$ m., the percent fluctuation is 12% for the pressure drop and 6% for the flow rate. The percent fluctuations are not statistically different between the two condenser elevations. At each condenser elevation considered in this study, the flow regime within the riser is observed to be annular immediately prior to instability. Knowing that bubble coalescence and void fraction play

a critical role in the fluctuation, it is quite reasonable that the fluctuations should not vary significantly between condenser elevations as observed in Figures 4-6 and 4-7.

Once the heat flux is increased beyond the limiting heat flux, large scale fluctuations are observed in the flow field. Figures 4-8 & 4-9 show the probability density functions for pressure drop and flow rate for $H = 1.33$ m and $H = 1.15$ m slightly beyond the limiting heat flux. In each case the distributions resemble those for a sinusoidal signal in the time domain. There are two distinct peaks for both the pressure drop and flow rate. The flow rate is observed to go negative which is indicative of flow reversal. The average measured flow rate is 0.011 kg/s for each case. The flow rate has a positive skewness while the pressure drop has a negative skewness. This is most likely a result of the dependency of pressure drop on flow rate within the system. As the flow rate is increased the vapor quality decreases and vice versa. Since pressure drop is strongly dependent on vapor quality, the pressure drop is largest at low flow rates where vapor quality is largest. Therefore, it is expected that a positive skewness in the flow rate would result in a negative skewness in pressure drop as observed in Figures 4-8 & 4-9.

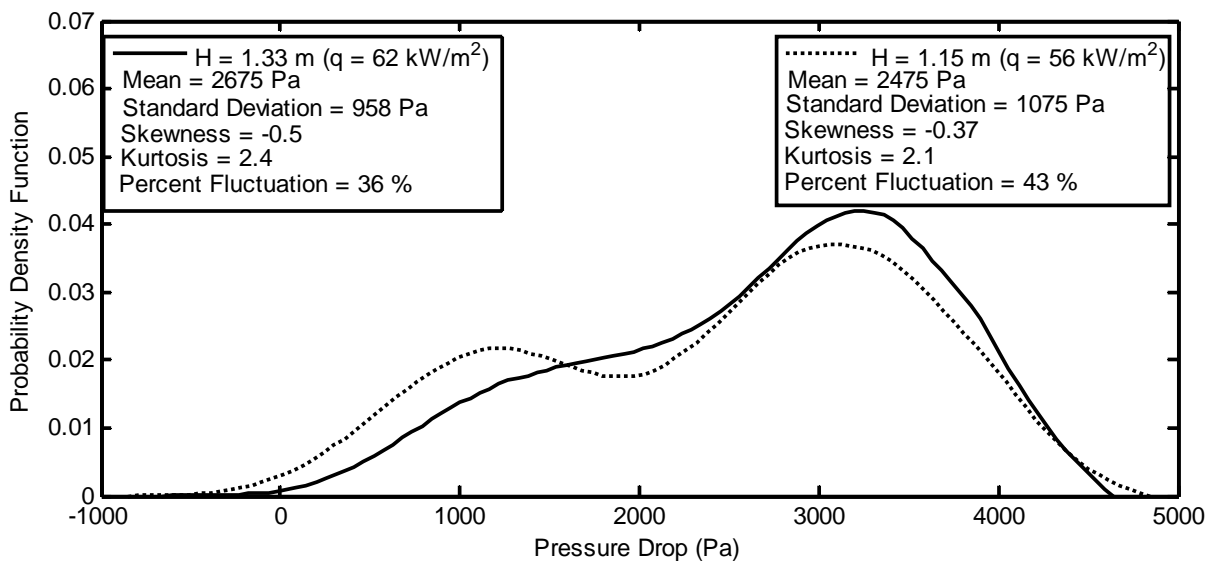


Figure 4-9. Measured probability density function for pressure drop following the onset of unstable flow.

A Fast Fourier Transform (FFT) was applied to the pressure drop and flow rate data taken at $H = 1.33$ m and $H = 1.15$ m. The data were taken for $N = 512$ data points with a sampling frequency, f_s , of 14 Hz, resulting in a period, T , of 37 s. Fig. 11 shows the power spectrum for mass flow rate, and the dominant frequency is approximately 0.8 HZ and 1 Hz, respectively, for $H=1.33$ m and 1.15 m. The measured power spectrum indicates a very strong periodic low frequency fluctuation when the flow becomes unstable.

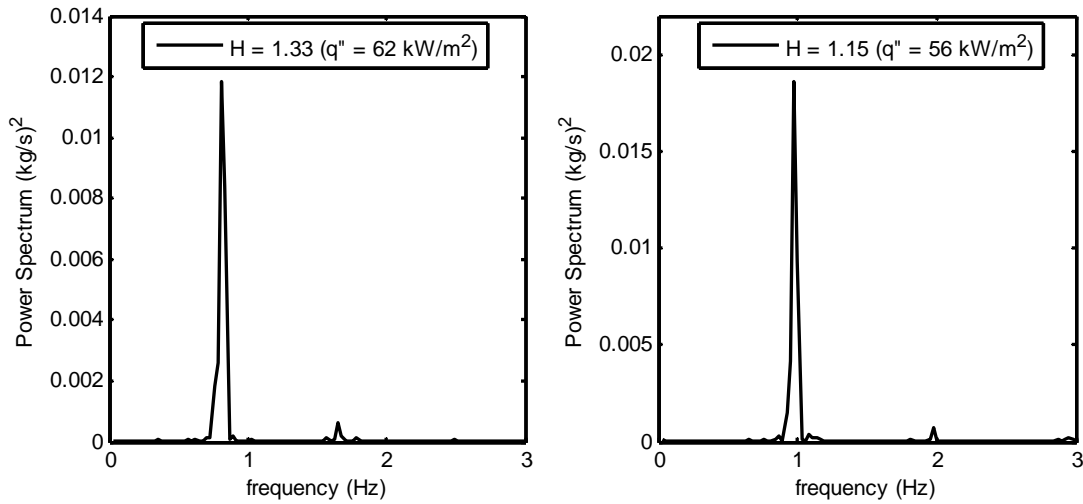


Figure 4-10. Power spectrum for mass flow rate; (a) $H = 1.33$ m, (b) $H = 1.15$ m.

Instability Prediction

In order to reliably predict the onset of instability, it is necessary to identify the controlling mechanism leading to the instability excursion. After giving consideration to the instability mechanisms described by Boure et al. (1973) and Tadrist (2006) it is concluded that the onset of the heat flux limiting instability observed in the thermosyphon facility is due to a static Ledinegg instability. Such an instability involves a sudden change in the flow rate to a lower value followed by oscillations and ultimately system failure. In forced convection, the phenomenon is governed by the slope of pressure gradient with respect to mass flux for both the internal system characteristics (friction, acceleration, and gravity) and the external system

characteristics (the pumping mechanism). In the case of natural circulation, the pumping mechanism itself is the gravitational pressure head exerted by the downcomer. The criterion for unconditionally stable flow is simply,

$$\frac{\partial \Delta P_s}{\partial G} > 0. \quad (4-3)$$

For the current facility, ΔP_s is the change in pressure between the condenser outlet and inlet and is zero for quasi-steady state operation. In order to investigate whether the system operation is stable, ΔP_s is first computed at each heat flux interval using Eq. 2.2. The quasi-steady state mass flux is that which gives zero pressure drop between the condenser inlet and exit and is determined for each heat flux interval. A perturbation in mass flux from the quasi-steady state, ΔG , of 5% is used based on the percent fluctuations revealed experimentally in Figure 4-7. The change in system pressure drop resulting from a 5% perturbation in mass flux is approximated as follows,

$$\frac{\partial \Delta P_s}{\partial G} \approx \frac{\Delta P_s|_{G+\Delta G} - \Delta P_s|_G}{\Delta G}. \quad (4-4)$$

The system heat flux for which $\frac{\partial \Delta P_s}{\partial G}$ is negative is associated with unstable flow, and thus the limiting heat flux is that for which $\frac{\partial \Delta P_s}{\partial G} = 0$.

For the flow to transition to the unstable regime, the sum of the frictional, gravitational, and accelerational pressure change with respect to mass flux must be less than zero. Throughout the thermosyphon loop, the accelerational component of pressure drop is an order of magnitude smaller than the frictional and gravitational components and can be considered negligible here for discussion purposes. At high heat flux, where the instability occurs, the frictional pressure gradient within the microchannel plate is approximately 50 times the pressure gradient in the

frictional pressure drop is reduced, and further increases in flow rate and decrease in vapor quality can result, until the flow swings back to region I. However, the flow state does not remain in region I for long due to the high heat flux and rapid increase in vapor quality. This behavior continues back and forth in an oscillatory mode until eventual dryout. It is noted that the flow in region II may be stable as long Equation 4-3 is satisfied.

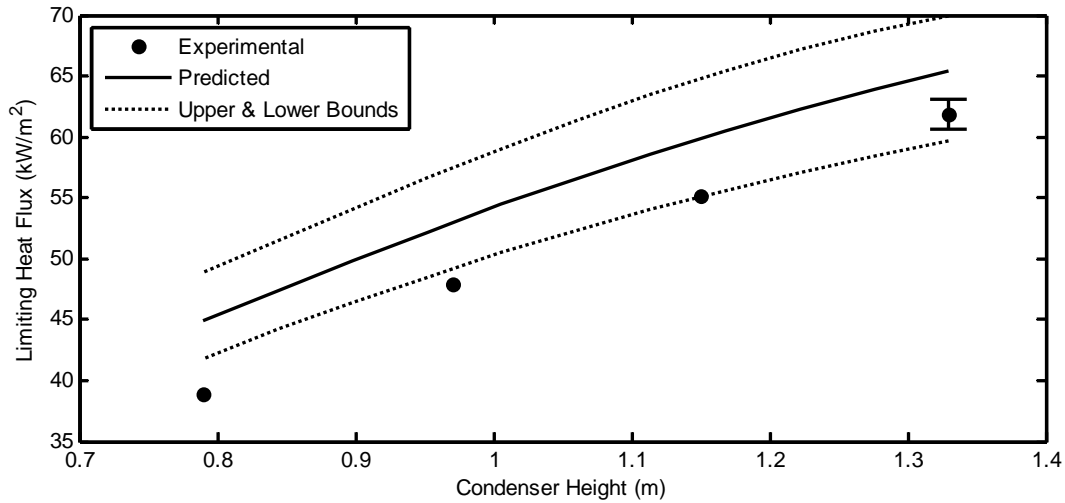


Figure 4-12. Comparison of measured and predicted heat flux at the onset of instability.

Figure 4-12 shows the computed limiting heat fluxes compared with those determined experimentally. Also shown are the upper and lower bounds of the computed limiting heat fluxes based on the uncertainties associated with the frictional pressure drop and vapor volume fraction predictions. To compute the upper and lower bounds, the model was run using the upper and lower bounds of both the frictional pressure drop and the vapor volume fraction, based on the associated error in the correlations, and the highest and lowest predicted limiting heat flux were taken as the bounds. The experimental measurements tend to fall on the lower bound of uncertainty. Given the complex nature of two-phase flow, the agreement is considered to be satisfactory.

CHAPTER 5
PERFORMANCE OF ALUMINUM AND CARBON FOAMS FOR AIR SIDE HEAT
TRANSFER AUGMENTATION

Background and Objectives

Improving condenser and evaporator performance has been a widely studied topic in the context of compact and efficient heat exchanger design. It has been a subject of interest in the process, cryogenic, power, refrigeration and air conditioning industries among others. While air flow heat exchangers have been in use by industry for many years, new challenges arise and opportunities for performance enhancement persist. Since most air cooled heat exchangers are limited in performance by the thermal resistance on the air side, focus has been on advancing the air side capabilities. This is achieved by increasing the heat transfer surface area in contact with the flowing air, or by increasing the heat transfer coefficient. In many applications it is common to use a louvered fin that acts to break up the thermal boundary layer and improve net heat transfer with an increase in both surface area and heat transfer coefficient (Chang and Wang, 1997). While densely packed louvered fins will greatly enhance heat transfer, the increased pressure drop can make such a configuration undesirable due to increased pumping power. Typically there is an optimum spacing that represents a tradeoff between enhanced heat transfer and increased pumping power requirements.

Another approach to enhancing the air side heat transfer rate is to replace the fins with a high thermal conductivity porous structure. These structures are capable of increasing the heat exchange surface area while producing a tortuous flow path that breaks up the thermal boundary layer and enhances the heat transfer coefficient. However, the pressure drop across the porous media is amplified as a result, and increased pumping power is required.

Numerous experiments have considered forced convective air heat transfer enhancement associated with porous metal foams. In general the experiments can be categorized as those that

measure a bulk heat transfer coefficient and those that measure the interstitial heat transfer coefficient. The bulk heat transfer coefficient is defined as the ratio of the surface heat flux to the difference in temperature between the heater wall and inlet air temperature. Convective air bulk heat transfer coefficient measurements for porous metal foams have been reported by Hsieh et al. (2004), Haak et al. (2001), Kim et al. (2000), and Tzeng (2007). While such measurements may be useful to test a specialized geometry and flow configuration, their utility is generally limited.

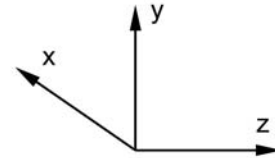
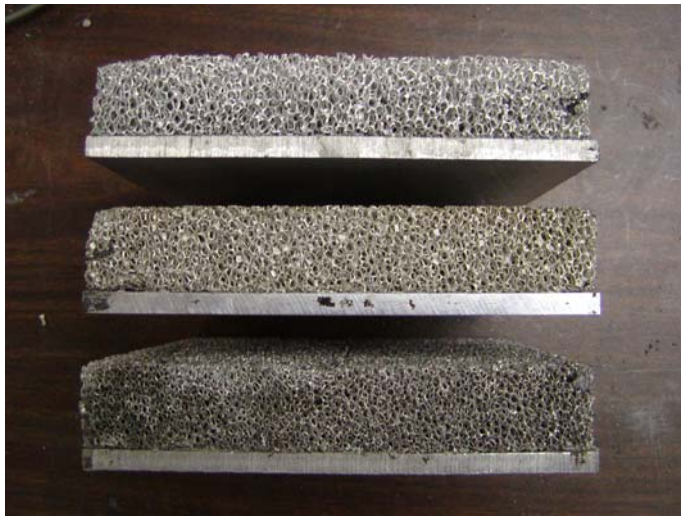
The other approach is to treat the metallic foam as flow through a porous media and solve the solid and fluid coupled energy equations to extract the interstitial heat transfer coefficients from the measured thermal fields. This approach has been pursued by Calmidi and Mahajan (2000), Jeng et al. (2005) and Hwang et al. (2002). The advantage to this approach is that the interstitial heat transfer coefficient only depends on the local interstitial geometry of the metallic foam. Thus, the results may be combined with a solution of the solid and fluid coupled energy equation to analyze porous foam heat exchangers with any arbitrary geometry. Analyses of this type are reported by Lu et al. (2006) and Zhao et al. (2006).

This paper considers the heat transfer augmentation provided by porous metal foams and compares them against conventional louvered fins. Three types of aluminum and three types of carbon foam are considered. An experimental facility has been set up to measure the pressure drop and volumetric heat transfer coefficient with air flow velocities ranging from 1 to 6 m/s. The Darcy-Forcheimer equation is used to correlate the pressure drop data. The Nusselt number is correlated with Reynolds number based on appropriate length scales. Due to very significant differences in the porous structures, different correlations are used for the aluminum and carbon foams. For comparison against conventional louvered fins, a hypothetical heat exchanger is

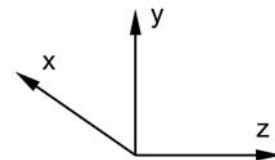
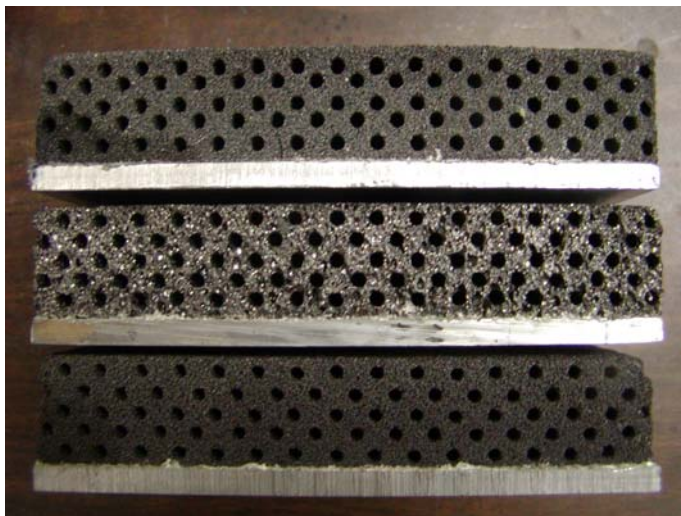
analyzed and the performance is determined based on a Coefficient of Performance (COP), Compactness Factor (CF), and Power Density (PD).

Experimental Facility

Three different aluminum foam samples manufactured by Energy Research and Generation Inc. are studied here along with three carbon foam samples manufactured by Koppers Inc. The samples are shown below in Figs. 5-1 a & b and the properties are given in Table 5-1. The aluminum foams are identified by the manufacturer according to pore density, with values of 10, 20, and 40 pores per inch (PPI). The bulk density of all aluminum foam samples is 216 kg/m^3 . The pore sizes for the 10, 20, and 40 PPI aluminum foams are 0.5, 1, and 2 mm, respectively. The three carbon foam samples are identified by the manufacturer as L1, D1, and L1A. The respective pore sizes according to the manufacturer are 600, 650, and 500 μm . Due to the small pore size and large pressure drop required to convey air through the foams, they were modified by machining cylindrical air passages in the axial direction. In each case, 80 passages, 6.7 mm apart, each with a diameter of 3.2 mm, were machined into the foam providing for a uniform, homogeneous geometry. The modified L1, D1 and L1-A, foams have bulk densities of 317, 400, and 284 kg/m^3 , respectively. Due to the large ratio of passage diameter to pore diameter, there is not a large pressure drop variation between carbon foam samples. It is assumed throughout the analysis that convection heat transfer is dominated by air flow through the machined passages. Therefore the same surface area per unit volume, a , for each carbon foam sample is 5.24 m^{-1} and the porosity based on the flow passages is 0.166.



(A)



(B)

Figure 5-1. A) Carbon foam samples, from top to bottom: L1A, D1, & L1. B) Metal foam samples, from top to bottom: 10PPI, 20PPI, & 40 PPI.

The experimental facility displayed in Fig. 5-2 is used to measure the pressure drop and heat transfer coefficient with air blowing through the foam. As shown, a variable speed blower forces air through the foam sample in which a 15.24 cm. x 15.24 cm. aluminum plate is bonded to the foam using S-bond material. A 15.24 cm. x 15.24 cm. foil heater is in contact with the bottom side of the aluminum plate. Five type E thermocouples are embedded into the aluminum

plate to measure the lower wall temperature while five more type E thermocouples are located axially along the top surface of the foam to measure the upper wall temperature. The upper wall temperature is used in this analysis instead of the lower wall temperature in order to eliminate the error associated with contact resistance between the heater and the foam. The foam sample is 15.24 cm. x 15.24 cm. x 2.54 cm. in volume. Validyne differential pressure transducers measure the pressure drop across the foam. Seven pressure taps are located axially along the foam sample to measure the pressure variation along the channel. Another Validyne differential pressure transducer measures the pressure drop from a pitot tube to obtain the mean air velocity. All analog signals were captured using a digital data acquisition system consisting of a Measurement and Computing CIO-EXP32 multiplexer and PCIM-DAS1602 16 bit analog to digital converter. A custom algorithm was developed to convert measured voltages to pressure, temperature, and velocity.

The experimental facility is used to measure the heat transfer coefficient and pressure drop for each foam sample at different velocity increments. The pressure drop is measured adiabatically. Throughout the heat transfer experiments the heat flux remains fixed at 9.77 kW/m^2 , and the air velocity is increased in increments. The mean velocity ranges from approximately 1 to 6 m/s for the pressure drop and heat transfer experiments, beyond which point there is a substantial increase in pressure drop and only a marginal increase in the heat transfer rate. At each velocity increment, the upper foam temperature is observed until steady state is reached, at which point 500 data points are sampled at 1 Hz. The measurement is repeated 5 times to insure repeatability. The air velocity is then increased and the procedure is repeated. The uncertainty in temperature and pressure drop is explained in detail in Appendix – B.

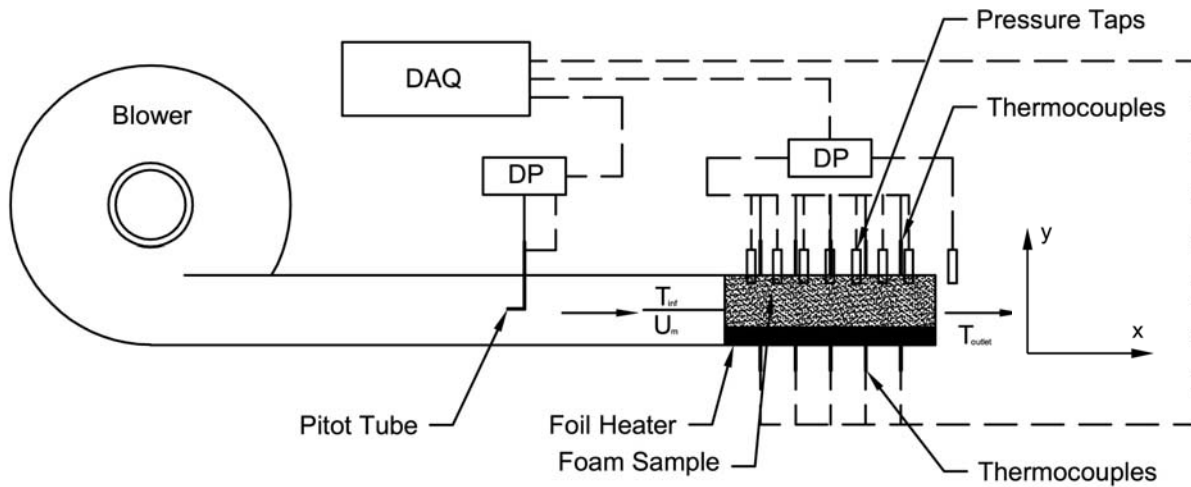


Figure 5-2. Porous media experimental facility.

Experimental Results

For each foam sample considered, the measured pressure drop and foam upper wall temperature are tabulated in Tables C1 and C2 in Appendix-C. The axial pressure variation is shown in Fig. 5-3 for the 10 PPI sample operating at $u_m = 1.13 \text{ m/s}$. The observed linear variation is indicative of fully developed flow. dp/dx , provided for each foam sample in Table-C1, gives the pressure gradient. The measured pressure gradient is shown in Fig. 5-4 & 5-5 with varying air velocity. As observed, the pressure gradient increases parabolically with increasing air velocity. The foam upper wall axial temperature profile is shown in Fig. 5-3 for the 10 PPI sample operating at $u_m = 1.13 \text{ m/s}$. The wall temperature gradient shown in Fig. 5-3 is used to determine the sensible heat transfer to the fluid, which is compared against the measured heat input confirm an energy balance. The upper wall temperature of the upper foam at $x = 7.62 \text{ cm}$. is plotted versus mean fluid velocity in Fig. 5-6. As observed, the temperature drop decreases with increasing air velocity. The upper wall temperature profiles of the three aluminum foams appear to be similar. At low velocity an incremental increase in velocity results in a large drop

in foam wall temperature and a moderate increase in pressure drop. However, at relatively high air velocities, an incremental change in velocity results in a large increase in pressure drop and only moderate decrease in foam temperature.

Table 5-1. Foam properties.

Foam Sample	K (m^2)	C_F	ε	ε_p	d_p (m)	k_{se} ($\frac{W}{mK}$)	a (m^{-1})
40 PPI	6.98×10^{-9}	0.020	0.918	NA	5.08×10^{-4}	9.78	2760
20 PPI	1.21×10^{-8}	0.021	0.918	NA	1.02×10^{-3}	9.78	1770
10 PPI	1.98×10^{-8}	0.027	0.918	NA	2.03×10^{-3}	9.78	804
L1-A	1.66×10^{-8}	0.034	0.166	.806	5×10^{-4}	48.6	5.24
D1	1.66×10^{-8}	0.034	0.166	.752	6.5×10^{-4}	97.2	5.24
L1	1.66×10^{-8}	0.034	0.166	.735	6×10^{-4}	61.8	5.24

The pressure gradient for carbon and aluminum foams may be correlated using the Darcy-Forcheimer equation (Vafai and Kim, 1989),

$$-\frac{dP}{dx} = \frac{\mu_{fl}}{K} u_m + \frac{\rho_{fl} C_F}{\sqrt{K}} u_m^2, \quad (5-1)$$

where K is the permeability, C_F is a dimensionless parameter that accounts for inertia effects, and u_m is the mean velocity. C_F and K are determined from the tabulated pressure drop data shown in Table 4-1 by fitting the data to Eqn. (5-1) and extracting C_F and K . The measured K and C_F are listed in Table 5-1 for each foam. In the case of carbon foam, the difference in the pressure drop between data samples is not large because the majority of air flows through the machined passages. The small difference is attributed to flow through the interstitial pores.

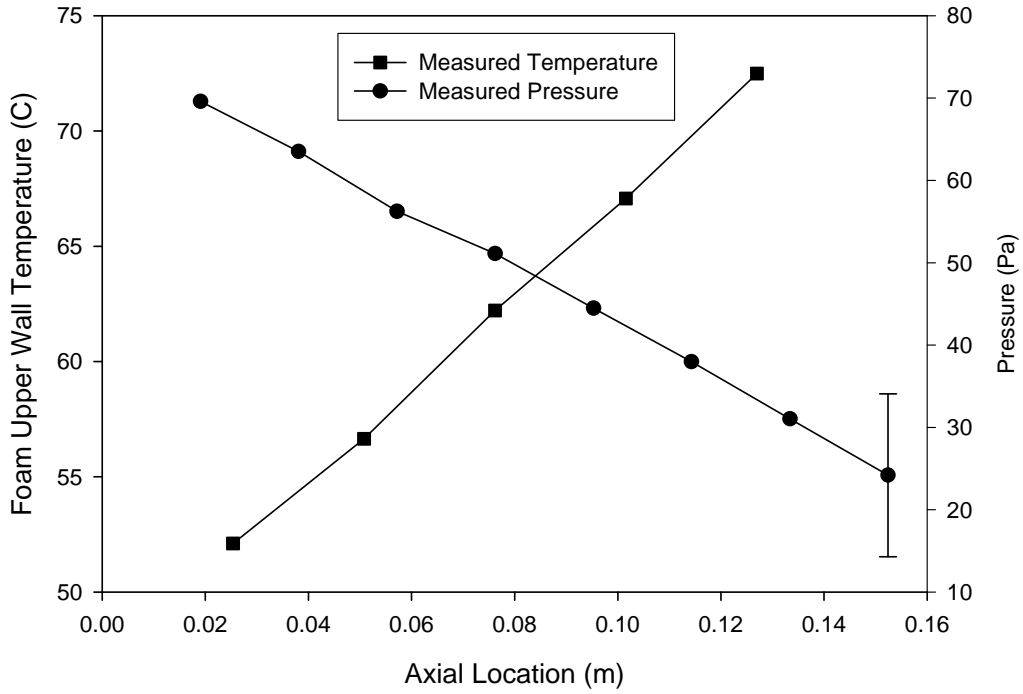


Figure 5-3. Axial pressure upper wall temperature variation for 10 PPI aluminum foam sample, $u_m = 1.13 \text{ m/s}$.

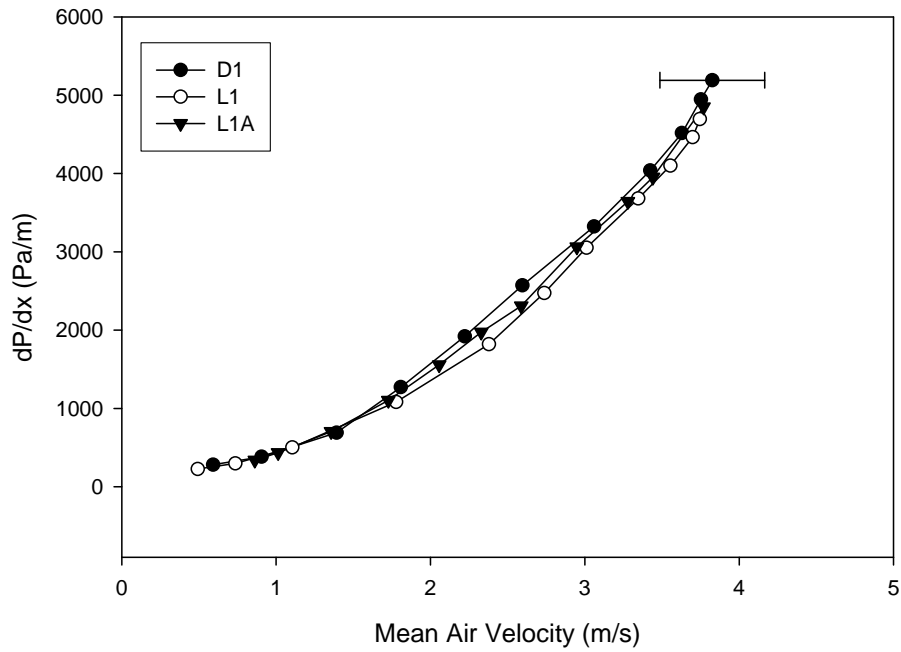


Figure 5-4. Carbon foam pressure gradient variation with mean air velocity.

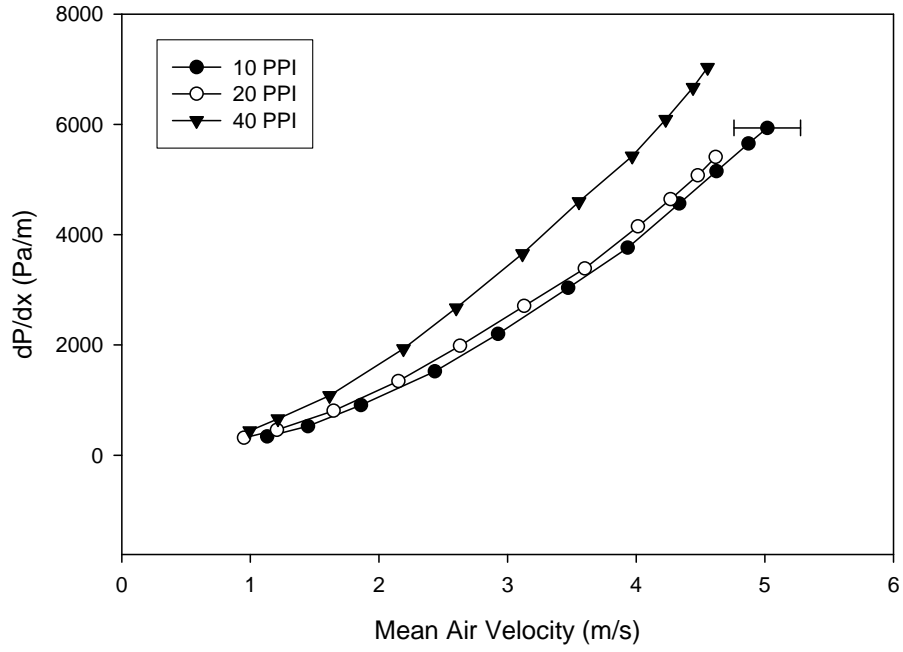


Figure 5-5. Aluminum foam pressure gradient variation with mean air velocity.

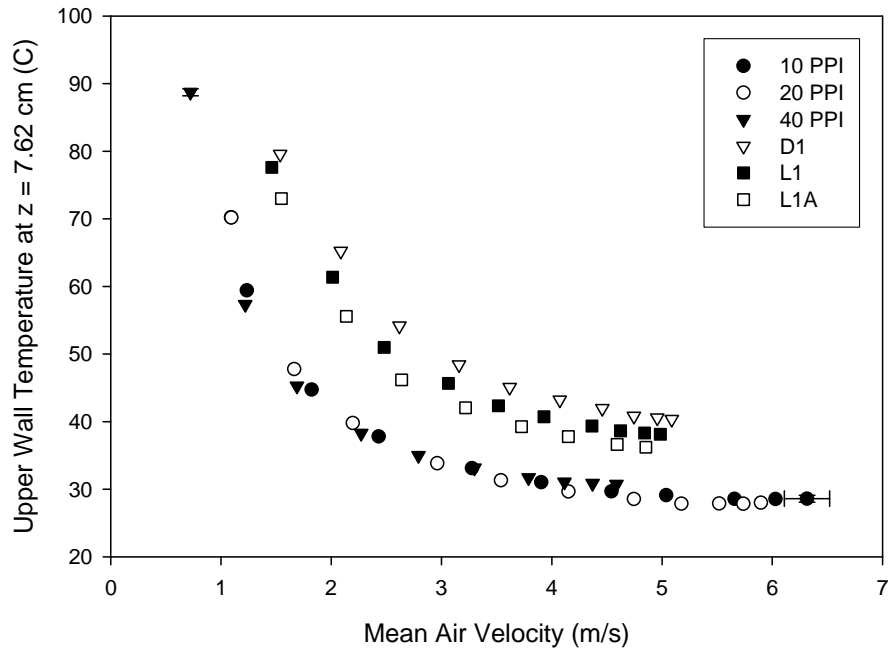


Figure 5-6. Foam upper wall temperature variation with mean air velocity.

Heat Transfer Analysis

In order to extract the local heat transfer coefficient from the measured foam temperatures, the steady volume-averaged momentum equation and a two equation non-equilibrium heat transfer model proposed by Calmidi and Mahajan (2000) are employed.

In this analysis it is assumed that all thermo-physical properties of the solid and fluid are independent of temperature. The foams are modeled as homogenous porous media, and the effects of radiation, natural convection, and thermal dispersion are negligible (Jeng, 2005). The governing conservation equations can be expressed as (Lu et al, 2006),

Momentum

$$-\nabla P - \frac{\mu}{K} \bar{V} + \frac{\mu}{\varepsilon} \nabla^2 \bar{V} - \frac{\rho_{fl} C_F}{\sqrt{K}} |\bar{V}| \bar{V} = \frac{\rho_{fl}}{\varepsilon^2} \bullet \bar{V} \bar{V}, \quad (5-2)$$

Energy (Solid)

$$(1 - \varepsilon) k_s \nabla^2 T_s + h_{sf} a (T_{fl} - T_s) = 0 \quad (5-3)$$

Energy (Fluid)

$$\rho_{fl} C_{p,fl} \bar{V} \bullet \nabla T_{fl} = \varepsilon k_{fl} \nabla^2 T_{fl} + h_{sf} a (T_s - T_{fl}), \quad (5-4)$$

where μ_{fl} is the dynamic viscosity of the fluid, ε is the porosity, K is the permeability, h_{sf} is the interstitial heat transfer coefficient, and a is the surface area per unit volume for the porous material. The product of h_{sf} and a is the volumetric heat transfer coefficient, h_v . Here ρ_{fl} and $C_{p,fl}$ are the respective density and specific heat of the fluid, while k_{fl} and k_s are the thermal conductivity of the fluid and solid, respectively.

During the experiments, the upper wall of the foam test section is insulated. The boundary conditions are, $u(y=0) = 0$, $u(y=H) = 0$, $-k_{se} \frac{\partial T_s}{\partial y} \Big|_{y=0} - k_{fe} \frac{\partial T_f}{\partial y} \Big|_{y=0} = q_w$,

$$k_{se} \frac{\partial T_s}{\partial y} \Big|_{y=H} + k_{fe} \frac{\partial T_f}{\partial y} \Big|_{y=H} = 0, T_f(x=0) = T_\infty, \frac{\partial^2 T_f}{\partial x^2} \Big|_{x=0} = 0, \frac{\partial^2 T_s}{\partial x^2} \Big|_{x=0} = 0, \text{ and } \frac{\partial^2 T_s}{\partial x^2} \Big|_{x=L} = 0. \text{ The}$$

following dimensionless variables are introduced (Calmidi and Mahajan, 2000)(Lu et al., 2006)

$$\theta = \frac{T - T_\infty}{q_w L / k_{se}}, x' = \frac{x}{L}, y' = \frac{y}{L}, U = \frac{u}{u_m}, Da_K = \frac{4K}{\varepsilon H^2}, \lambda = \varepsilon^{3/2} C_F \frac{u_m H}{2\nu_{fl}}, Bi = \frac{ha_{sf} L^2}{k_s},$$

$$Re_L = \frac{u_\infty L}{\nu_{fl}}, Re_K = \frac{u_m \sqrt{K}}{\nu_{fl}}, Pr = \frac{\nu_{fl}}{\alpha_{fl}}, \text{ and } St = \frac{ha_{sf} L}{\rho_{fl} C_{p,fl} u_m}$$
 where u and u_m are the respective

local and mean velocities, q_w is the applied heat flux along the lower wall, and $k_{fe} = \varepsilon k_{fl}$ and

$k_{se} = (1 - \varepsilon) k_s$ are the effective thermal conductivities of the respective fluid and solid.

Conservation equations (5-2 through 5-4) are non-dimensionalized as

$$\frac{\partial^2 U}{\partial y'^2} = \frac{\varepsilon}{\sqrt{Da_K}} (U - 1) + \frac{Re_K}{Da_K} C_F \sqrt{\varepsilon} (U^2 - 1) \quad (5-5)$$

$$\frac{\partial^2 \theta_s}{\partial x'^2} + \frac{\partial^2 \theta_s}{\partial y'^2} + Bi(\theta_{fl} - \theta_s) = 0 \quad (5-6)$$

$$\frac{1}{\varepsilon} U \frac{\partial \theta_{fl}}{\partial x'} = \frac{1}{Re_L Pr} \left(\frac{\partial^2 \theta_{fl}}{\partial x'^2} + \frac{\partial^2 \theta_{fl}}{\partial y'^2} \right) + \frac{St}{\varepsilon} (\theta_s - \theta_{fl}) \quad (5-7)$$

with boundary conditions, $U(y'=0) = 0, U(y'=H/L) = 0, \frac{\partial \theta_s}{\partial y'} \Big|_{y'=0} + \frac{k_{fe}}{k_{se}} \frac{\partial \theta_f}{\partial y'} \Big|_{y'=0} = -1,$

$$\frac{\partial \theta_s}{\partial y'} \Big|_{y'=H/L} + \frac{k_{fe}}{k_{se}} \frac{\partial \theta_f}{\partial y'} \Big|_{y'=H/L} = 0, \theta_{fl}(x'=0) = 0, \frac{\partial^2 \theta_{fl}}{\partial x'^2} \Big|_{x'=0} = 0, \frac{\partial^2 \theta_{fl}}{\partial x'^2} \Big|_{x'=1} = 0, \text{ and } \frac{\partial^2 \theta_s}{\partial x'^2} \Big|_{x'=1} = 0.$$

The exact solution to the momentum equation has been provided by Vafai and Kim (1989) and is given below,

$$U = \frac{u_c}{u_m} \left[1 - \left(\frac{A+B}{A} \right) \left(sech(D(|y'|+C)) \right)^2 \right] \quad (5-8)$$

$$A = \frac{2\lambda}{3Da_K^{1/2}} \quad (5-9)$$

$$B = \frac{1}{Da_K} + \frac{4\lambda}{3Da_K^{1/2}} \quad (5-10)$$

$$C = -\frac{1}{D} \operatorname{sech}^{-1} \left(\sqrt{\frac{A}{A+B}} \right) - 1/2 \quad (5-11)$$

$$D = \frac{\sqrt{A+B}}{2} . \quad (5-12)$$

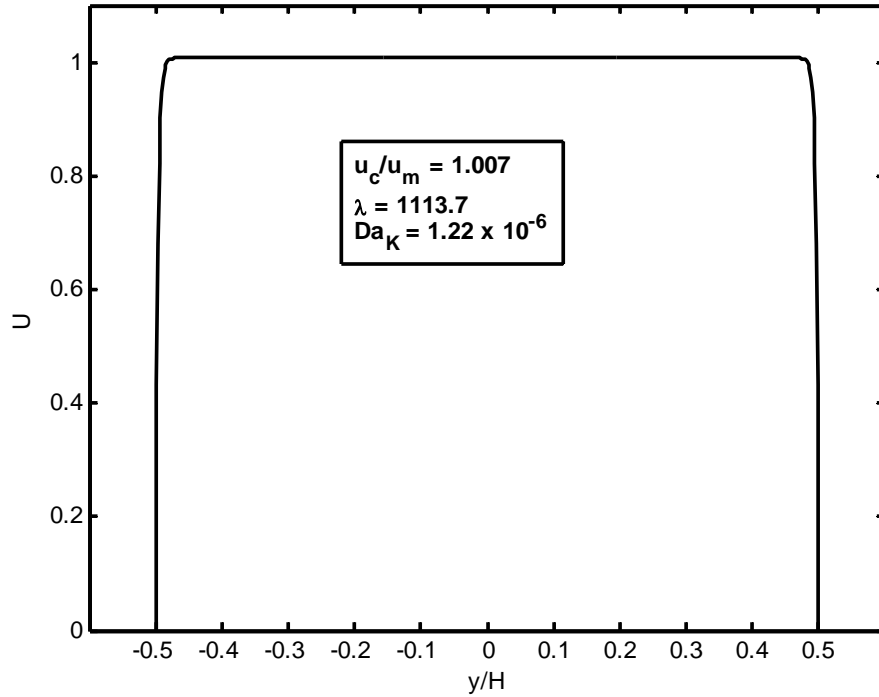


Figure 5-7. Dimensionless velocity profile.

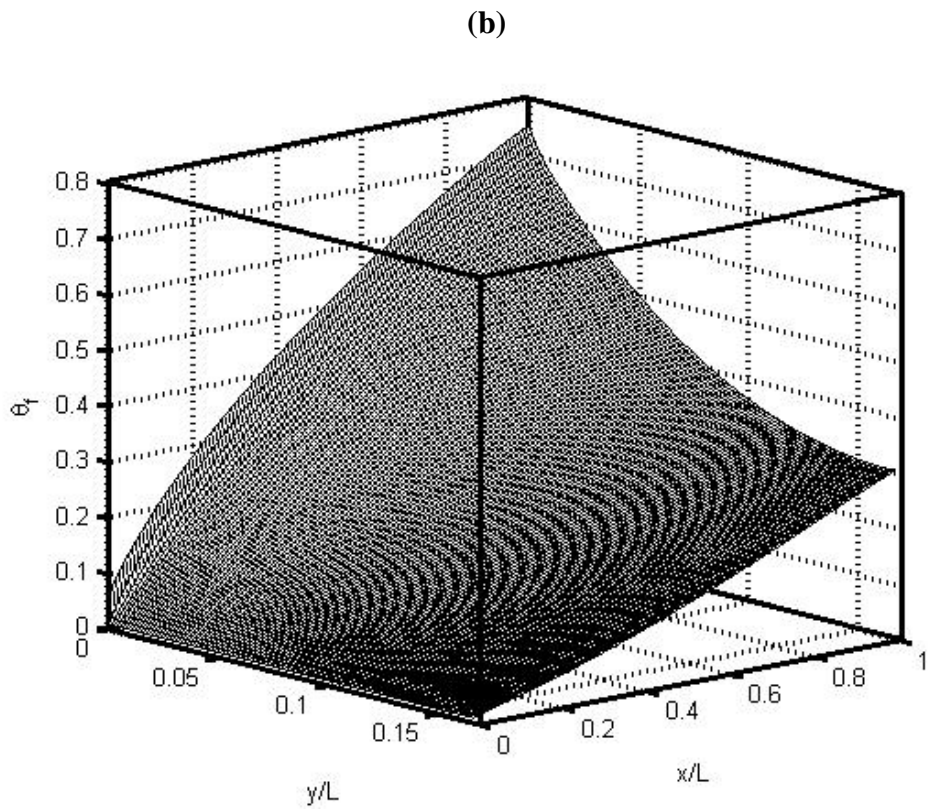
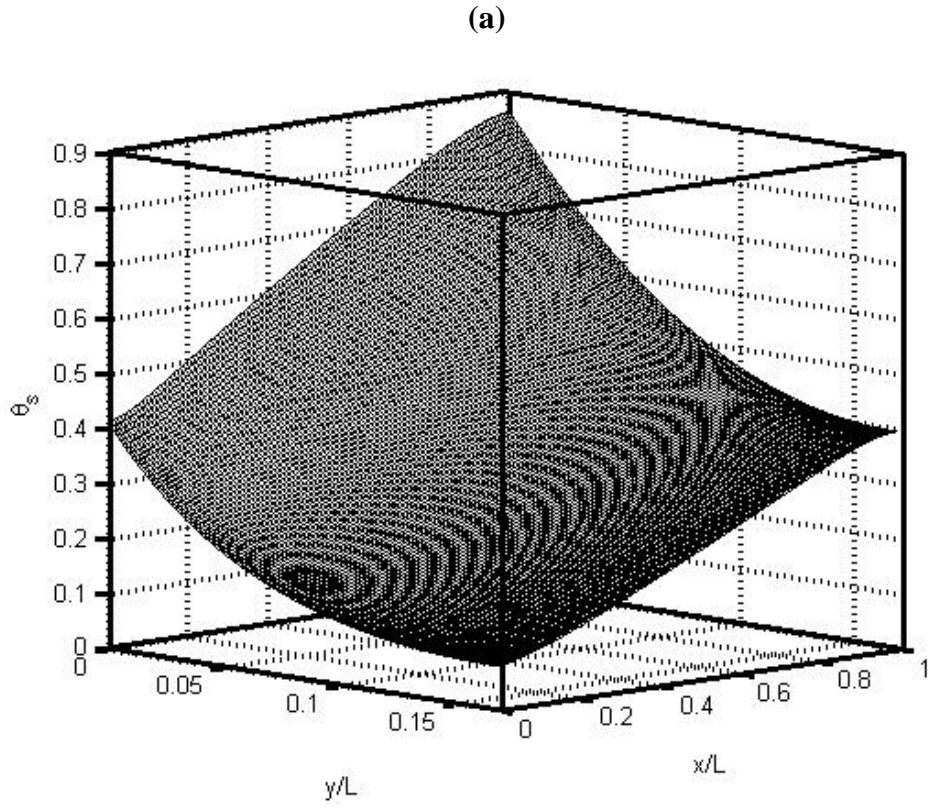


Figure 5-8. Dimensionless temperature profile. a) solid. b) fluid.

In order to compute the velocity field, a guess is made for u_c/u_m , The velocity profile is then computed from Eq. (5-8), and a check is made to insure mass conservation, $\frac{1}{A} \int U dA = 1$. If mass conservation is satisfied the solution is complete, otherwise a new guess is made for u_c/u_m and the procedure is repeated until the integral is satisfied.

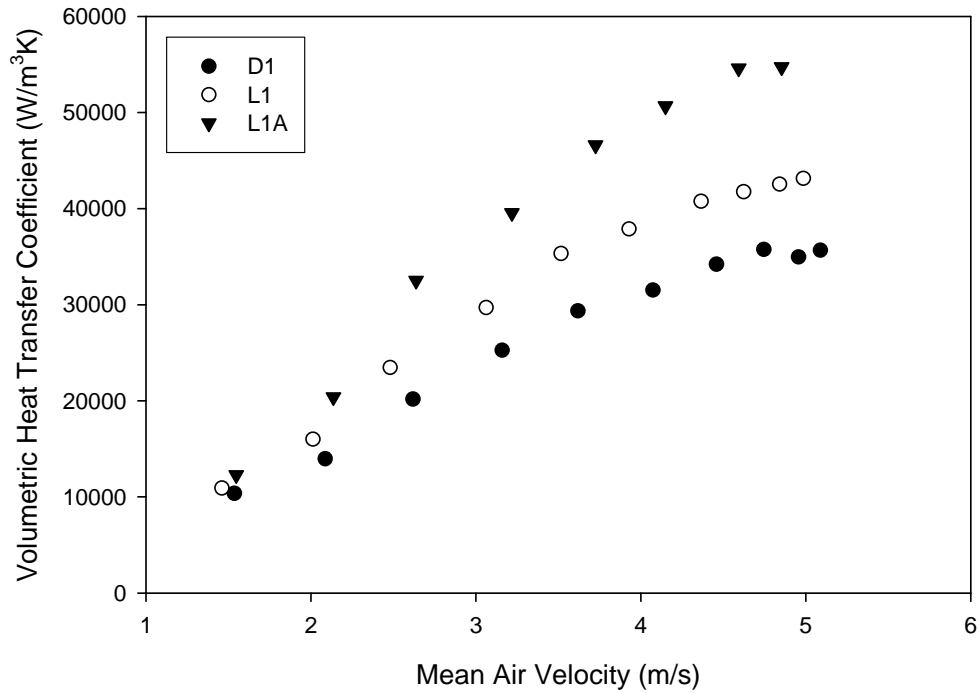


Figure 5-9. Carbon foam volumetric heat transfer coefficient variation with mean fluid velocity.

Solutions to the energy conservation equations were obtained using the Thomas algorithm. For $u_c/u_m = 1.007$, $\lambda = 1113.7$, $Da_K = 1.22 \times 10^{-5}$, $Re = 7,3048$, $Pr = 0.71$, $St = 0.54$, $\varepsilon = 0.92$, and $Bi = 7.56$, the computed dimensionless velocity profile is shown in Fig. 5-7 while that for temperature is shown in Figs. 5-8 a & b.

As observed, the velocity is uniform along the centerline with a value close to the mean velocity. The solid foam temperature decreases monotonically in the y-direction and increases

linearly in the x-direction. The fluid temperature initially decreases in the y-direction while increasing in the x-direction.

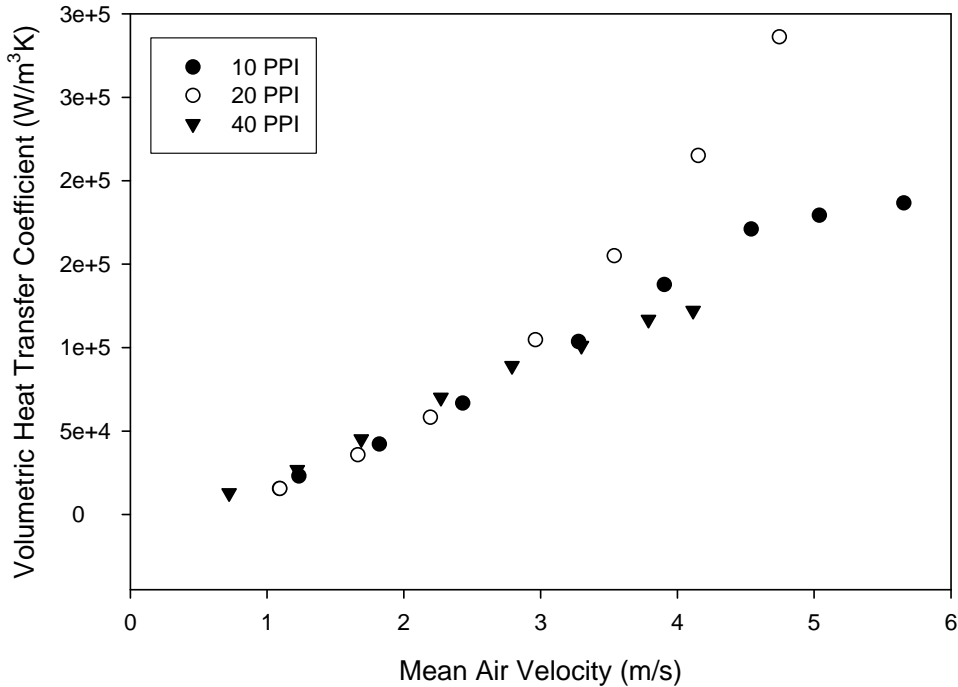


Figure 5-10. Aluminum foam volumetric heat transfer coefficient variation with mean fluid velocity.

When solving Eqs. 5-6 and 5-7 the heat transfer coefficient is not known a priori. Therefore, a guess is made for the heat transfer coefficient, h_{sf} , and solutions for Eqs. (5-6 & 5-7) yield θ_s and θ_{fl} . The upper foam temperature measured at $x = L/2$ is compared to that computed using the guessed value for h_{sf} . If agreement is achieved, the guessed heat transfer coefficient is correct. If they do not agree, a new guess is made for the heat transfer coefficient and the computation is repeated until agreement is achieved. In cases where the mean air velocity is large, the solid foam and air are in near thermal equilibrium. Thus large errors arise when extracting the volumetric heat transfer coefficients since most thermal transport is due to conduction through the porous medium. In such cases, a small change in the measured foam

upper wall temperature can result in a large change in the computed volumetric heat transfer coefficients.

Results

The volumetric heat transfer coefficients, $h_v = h_{sf} a$, are computed for each of the six foams and are summarized in Table C2 in the Appendix. Their variations with mean air velocity are shown in Figs. 5-9 & 5-10. The aluminum foams have the largest volumetric heat transfer coefficient. The aluminum foams are capable of handling a large heat load because they have large specific surface areas and large effective thermal conductivities. In order to correlate the volumetric heat transfer data, the permeability based Nusselt number is introduced,

$Nu_K = \frac{h_v \sqrt{K}/a}{k_{fl}}$. Fig. 5-11 shows the Nusselt number as a function of the Reynolds number,

$Re_K = \frac{u_m \sqrt{K}}{\nu_{fl}}$, for the three aluminum foams. It is observed that the data are well collapsed for

relatively low air velocity. At high air velocity, the solid and fluid are in near thermal equilibrium, and a large change in heat transfer coefficient results in only a small change in the solid foam temperature. Therefore, the error in the correlation at high velocities has a minimal effect on the computed solid temperature profile. Overall, the correlation allows for an accurate prediction of wall temperature for the full range of air velocities investigated here. The aluminum foam Nusselt number may be expressed as,

$$Nu_K = \frac{d_p}{\sqrt{K}} \left[\frac{Re_K}{4887} - 0.01 \right]. \quad (5-13)$$

For the carbon foam samples, if it is assumed that all of the air passes through the machined channels, and ideally each foam sample should have the same volumetric heat transfer coefficient at the same Reynolds number. However, variations in the data are observed. These

are explained by the fact that some air passes through the smaller interstitial pores of the foam.

Thus, it is reasonable to expect that the data can be correlated using the pore diameter. Fig. 5-12

shows the product of the Nusselt number, $Nu_D = \frac{h_v D^2}{k_{fl}}$, and $\left(\frac{D}{d_p}\right)^{-3/2}$ as a function of Reynolds

number, $Re_D = \frac{u_m D}{v_{fl}}$, for the three carbon foams. As observed, the data are also well correlated,

and the carbon foam Nusselt number may be expressed as

$$Nu_D = \left(\frac{D}{d_p}\right)^{3/2} \left(511 - \left(\frac{Re_D}{90} - 108\right)^{1.4} \right) \quad (5-14)$$

The standard error between the measured and predicted pressure drops and volumetric heat transfer coefficient for the aluminum and carbon foams are summarized in Table 5-2. As

observed, the volumetric heat transfer coefficient is predicted with reasonable accuracy.

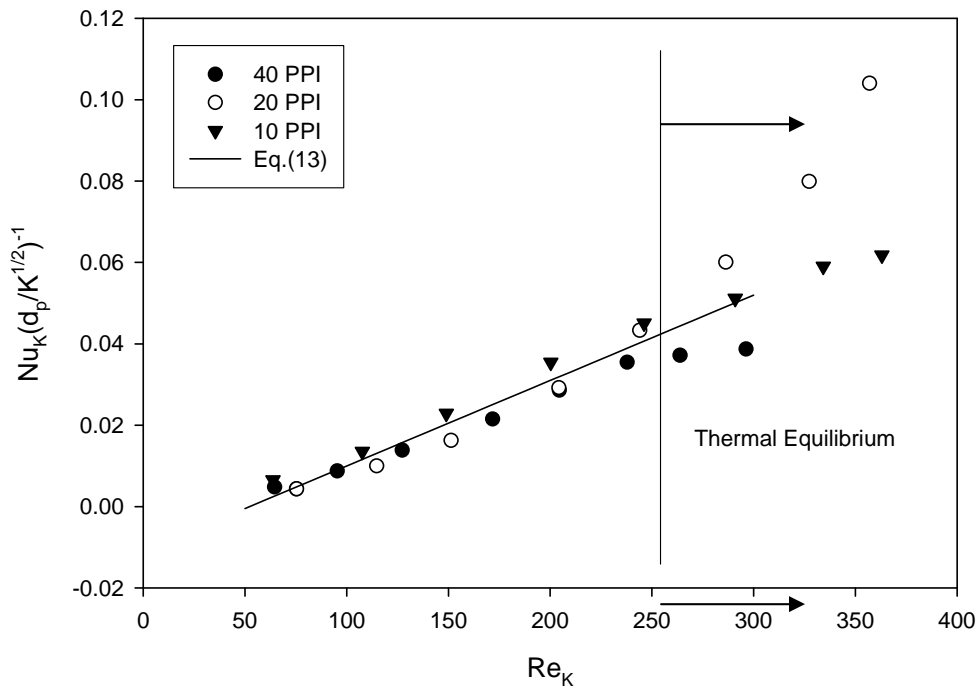


Figure 5-11. Nusselt number correlation for aluminum foams.

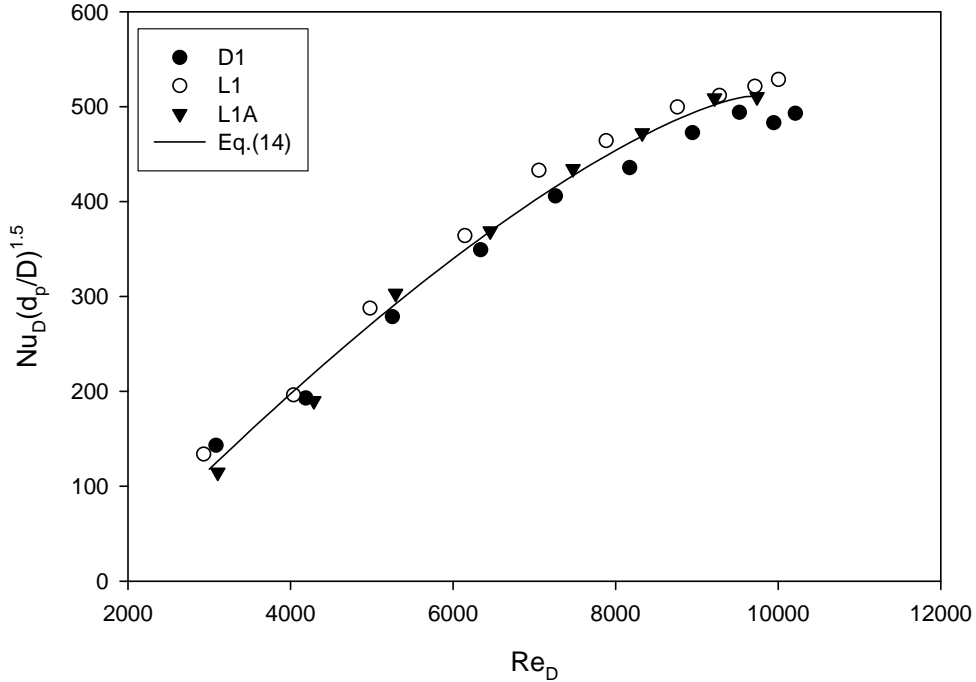


Figure 5-12. Nusselt number correlation for carbon foams.

Table 5-2. Relative error for pressure drop and Nusselt number correlations.

Foam Sample	Relative Error (ΔP)	Relative Error (Nu_k)
10 PPI	4%	5%
20 PPI	3%	19%
40 PPI	5%	5%
L1A	2%	4%
D1	9%	5%
L1	9%	9%

Hypothetical Heat Exchanger Performance

For comparison purposes, a hypothetical heat exchanger having specified dimensions is analyzed for each foam sample as well as for louvered fins. An illustration of the geometry is provided in Fig. 5-13.

The louvered fin geometry shown in Fig. 5-13a is common in compact heat exchangers and can be further classified as multi-louvered. The flat tube configuration has been chosen because it allows for enhanced performance. Fiebig et al. (1994) shows that the heat exchanger element with flat tubes gives nearly twice as much heat transfer and only half as much pressure

loss as the corresponding heat exchanger element with round tubes allowing for a more compact, efficient design.

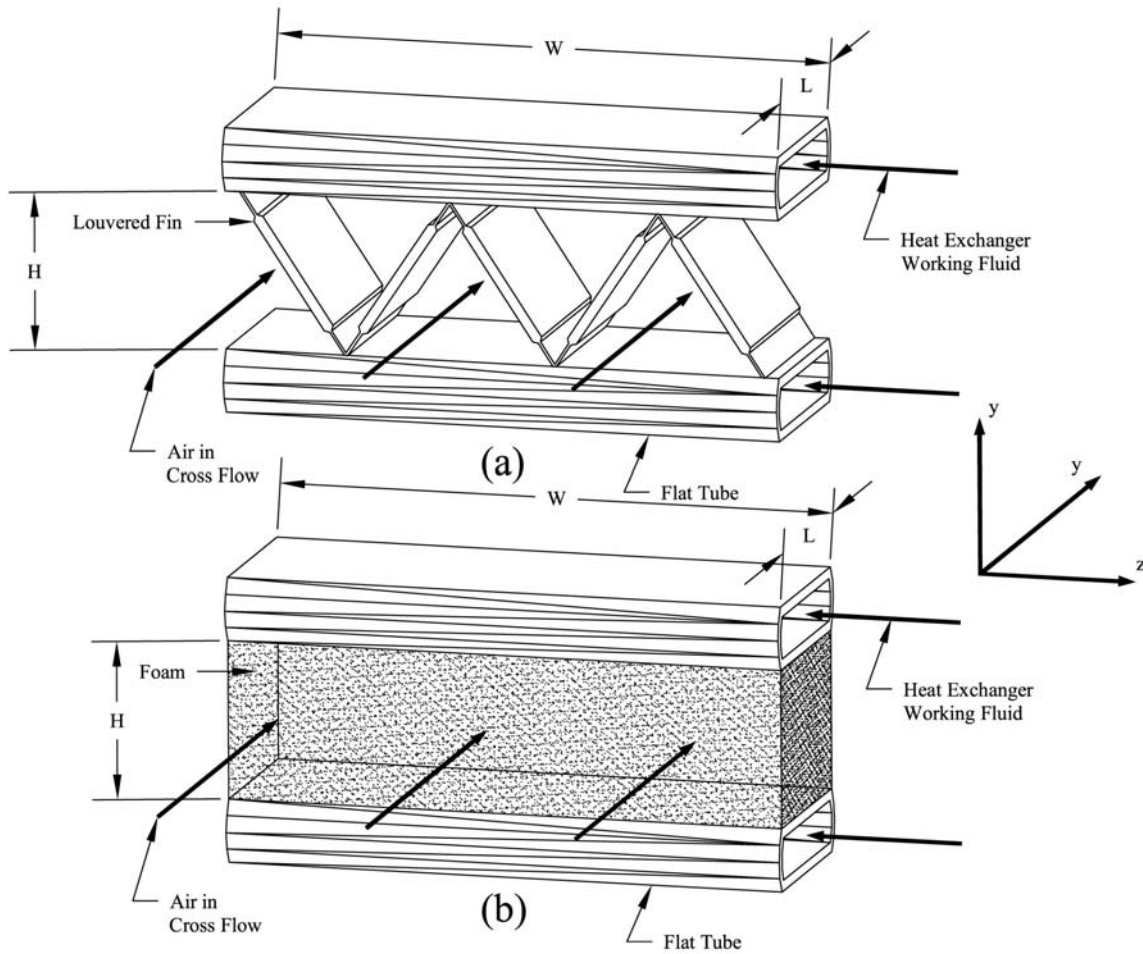


Figure 5-13. Hypothetical heat exchanger in cross flow. a) louvered fin. b) carbon/metal foam configurations.

The foam geometry shown in Fig. 4-13b constitutes the same flat tube arrangement as the louvered fin case and is oriented such that the heat exchanger working fluid is in cross flow with the ambient air, as is the case with the louvered fins. Since the only difference in the two designs is the extended surface area between tubes, the configuration allows for a quantitative comparison between each foam sample and the louvered fins.

To determine which configuration or enhanced surface yields the best, it is important to first have a clear definition of what constitutes good performance. The ideal heat exchanger will be compact in size and capable of removing the required heat load, while consuming a minimal amount of electric energy from the blower. Since a more compact heat exchanger must often consume more energy than a less compact heat exchanger under the same heat load, it is important to base the performance on both efficiency and compactness so that the designer can choose an optimal configuration that best suits each specific application. This paper evaluates the performance of each sample based on a Coefficient of Performance (COP; defined as the ratio of the total heat removed to the electrical input of the blower), Compactness Factor (CF; defined as the total heat removed per unit volume), and Power Density (PD; defined as the total heat removed per unit mass).

Numerical Model

In order to predict the heat removal capabilities of the hypothetical heat exchanger shown in Fig. 14b, the momentum equation for the fluid as well as the coupled energy equations for the solid and fluid are solved using Eqs. 5-2 through 5-4. The equations can be normalized by the following scales, $\theta = \frac{T - T_\infty}{T_w - T_\infty}$, $x' = \frac{x}{L}$, $y' = \frac{y}{L}$, $U = \frac{u}{u_m}$, and reduced to the following for two-dimensional rectangular coordinates,

$$\frac{\partial^2 U}{\partial y'^2} = \frac{\varepsilon}{\sqrt{Da_K}}(U - 1) + \frac{Re_K}{Da} C_F \sqrt{\varepsilon} (U^2 - 1) \quad (5-15)$$

$$\frac{\partial^2 \theta_s}{\partial x'^2} + \frac{\partial^2 \theta_s}{\partial y'^2} + Bi(\theta_{fl} - \theta_s) = 0 \quad (5-16)$$

$$\frac{1}{\varepsilon} U \frac{\partial \theta_{fl}}{\partial x'} = \frac{1}{Re Pr} \left(\frac{\partial^2 \theta_{fl}}{\partial x'^2} + \frac{\partial^2 \theta_{fl}}{\partial y'^2} \right) + \frac{St}{\varepsilon} (\theta_s - \theta_{fl}) \quad (5-17)$$

$$\text{Where } Da_K = \frac{4K}{\varepsilon H^2}, \lambda = \varepsilon^{3/2} C_F \frac{u_m H}{2\nu_{fl}}, Bi = \frac{ha_{sf} L^2}{k_s}, Re_L = \frac{u_\infty L}{\nu_{fl}}, Pr = \frac{\nu_{fl}}{\alpha_{fl}}, \text{ and } St = \frac{ha_{sf} L}{\rho_f C_{p,fl} u_m}.$$

The hypothetical heat exchanger described here will have a constant wall temperature of 100°C and an ambient air stream entering at 25°C . By implementing a constant wall temperature, the hypothetical heat exchanger will emulate a configuration with zero thermal resistance between the tubular inner working fluid and the tube wall. Assuming a no-slip condition at the wall, the boundary conditions along the tube wall and the fluid at the inlet are as follows, $U(y'=0)=0$, $U(y'=H/L)=0$, $\theta_{fl}(x', y'=0) = \theta_s(x', y'=0) = 1$,

$$\theta_{fl}(x', y'=H/L) = \theta_s(x', y'=H/L) = 1, \theta_{fl}(x'=0, y') = 0, \left. \frac{\partial^2 \theta_{fl}}{\partial x'^2} \right|_{x'=1} = 0, \text{ and } \left. \frac{\partial^2 \theta_s}{\partial x'^2} \right|_{x'=1} = 0. \text{ To}$$

simplify this analysis, two tubes are to be considered, with heat transfer taking place along both boundaries of the foam.

Using the volumetric heat transfer coefficient taken from Eqs. 5-13 through 5-14, along with the permeability, K , and the inertia coefficient, C_F , taken from Table 5-1, the governing equations are solved and the temperature field is obtained.

The total heat removed, $\dot{Q}_{removed}$, is computed from

$$\dot{Q}_{removed} = \dot{m} C_{p,f} (T_{f,out} - T_{f,in}) = 2 \left(-W \int_0^L (1-\varepsilon) k_s \frac{\partial T_s}{\partial y} \Big|_{y=0} dz - W \int_0^L (\varepsilon) k_f \frac{\partial T_f}{\partial y} \Big|_{y=0} dz \right), \quad (5-18)$$

while the pressure gradient is evaluated from Eq. (5-1). The electrical input to the blower is estimated as the product of the volumetric flow rate of air and the pressure drop:

$$\dot{E}_{input} = u_m A_c \Delta P, \quad (5-19)$$

where A_c is the frontal area of the heat exchanger seen by the ambient air stream. Finally the COP, CF, and PD are evaluated:

$$COP = \frac{\dot{Q}_{removed}}{\dot{E}_{input}} \quad (5-20)$$

$$CF = \frac{Q_{removed}}{V} \quad (5-21)$$

$$PD = \frac{Q_{removed}}{m} \quad (5-22)$$

Where V is simply the volume of the hypothetical heat exchanger and m is the mass.

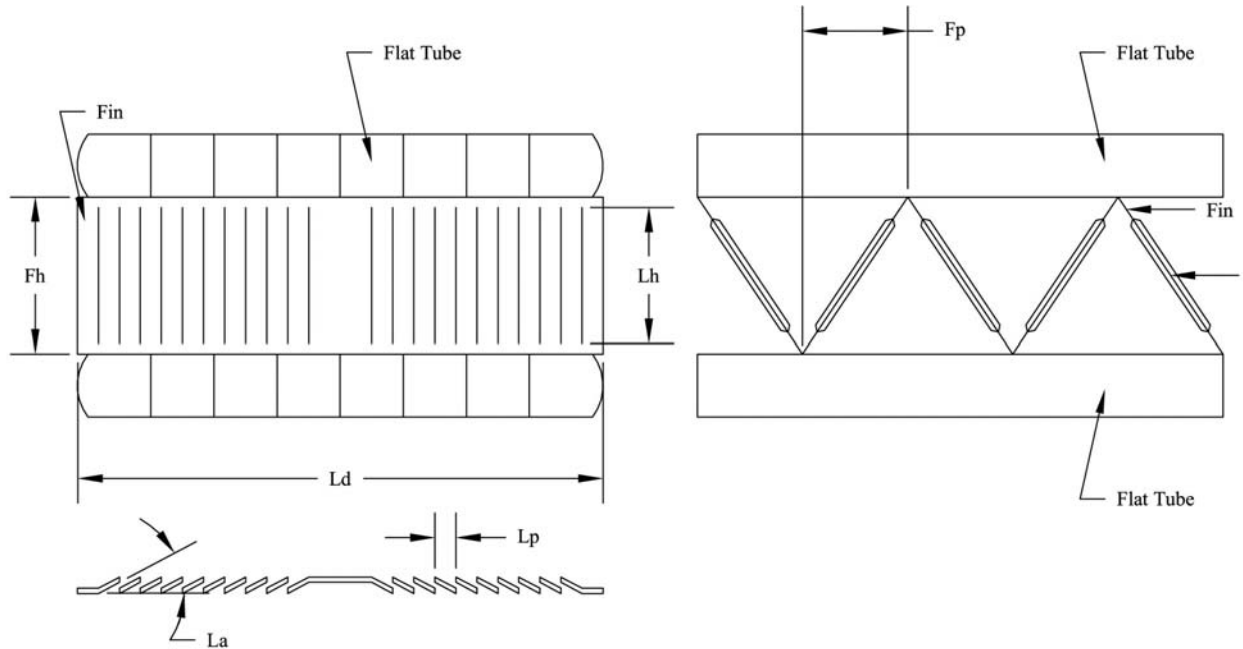


Figure 5-14. Geometric comparison of louvered fin and foam heat exchanger configurations.

For proper comparison, the heat removal capabilities of the louvered fins are to be obtained as well. Since there have been numerous experiments conducted on this subject, several correlations exist in the literature that provide accurate approximations for the interstitial heat transfer coefficient and pressure drop. Dong et al. (2007) have provided a correlation for interstitial heat transfer coefficient as well as pressure drop based on a large data base for multi-louvered fins.

Table 5-3. Geometric parameters for louvered fin configuration

Fh (mm)	60	Fp (mm)	4
Lh (mm)	58	Lp (mm)	1.2
Ld (mm)	100	La (degrees)	22

Using the correlations provided by Dong et al. (2007), the COP, CF, and PD are computed for the louvered fin heat exchangers and compared against those for each foam sample at different air velocities. The geometric parameters chosen to describe the louvered fin configuration are provided in Table 5-3 and illustrated in Fig. 5-14. The bulk density of the louvered fins is estimated based on these geometric parameters to be 128 kg/m^3 . The results of the comparison are illustrated below in Figs. 5-15 through 5-17.

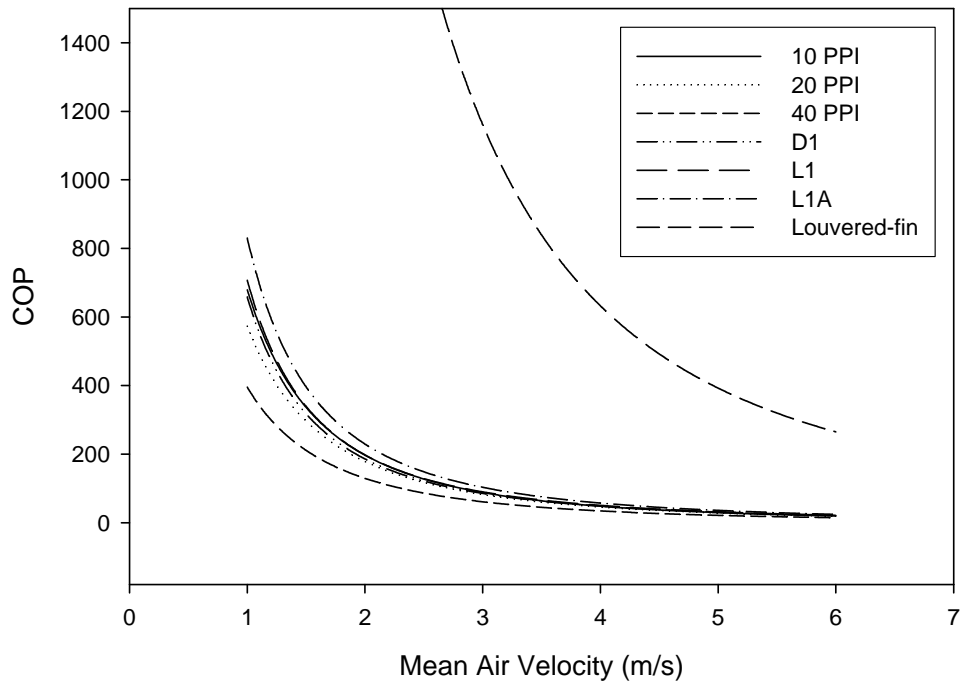


Figure 5-15. Comparison of coefficient of performance for louvered fin and foam configurations

Fig. 5-15, shows that the multi-louvered fin configuration is favorable over both the carbon and aluminum foam samples when COP is the main consideration. This is due to the added pressure drop resulting from the tortuous flow path characteristic of the foam. In the case of a louvered fin, several independent length scales exist that have an effect on COP including the fin pitch and louver pitch. A small fin pitch will increase surface area, while a small louver pitch will break up the thermal boundary layer more frequently. By reducing both of these length

scales, the heat removal should increase due to the increase in both surface area and heat transfer coefficient. However, this will also constrict the flow path and induce mixing, giving rise to an increase in pressure drop.

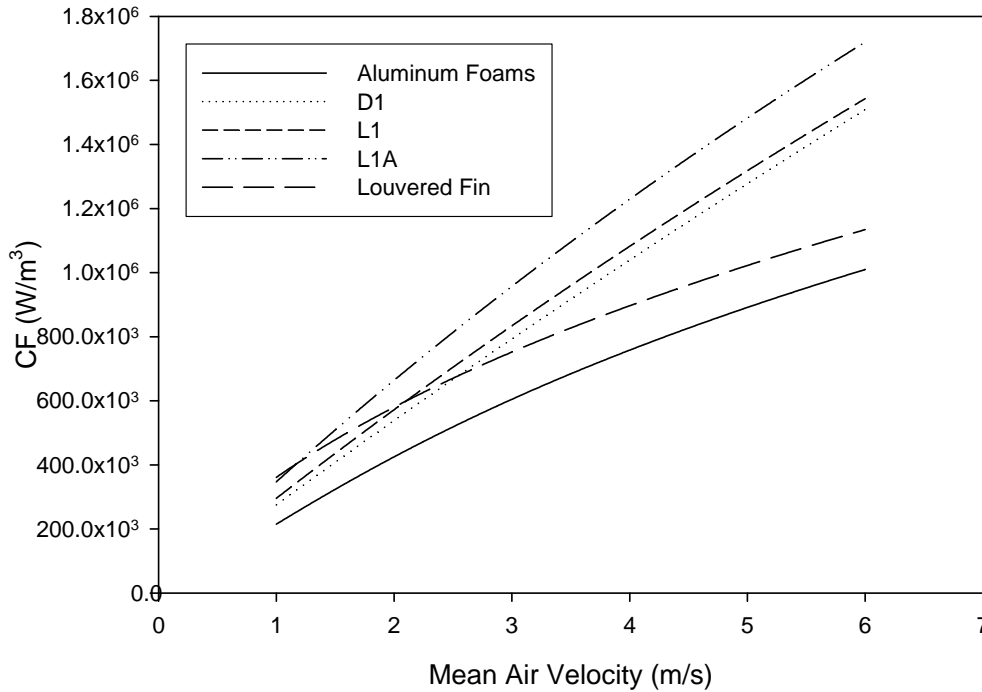


Figure 5-16. Comparison of compactness factor for louvered fin and foam configurations

In the case of flow through a homogeneous porous structure such as aluminum foam, the length scales of importance are the pore diameter, and the ligament diameter, or more importantly the square root of permeability. A more fundamental study on the flow structure within porous media is needed in order to develop a designer foam, capable of producing COP comparable to conventional louvered fin configurations. A comprehensive study using the Lattice-Boltzmann method may provide insight into the optimal geometric length scales needed to improve overall foam performance, as the current foam structures do not provide adequate COP when compared to louvered fins.

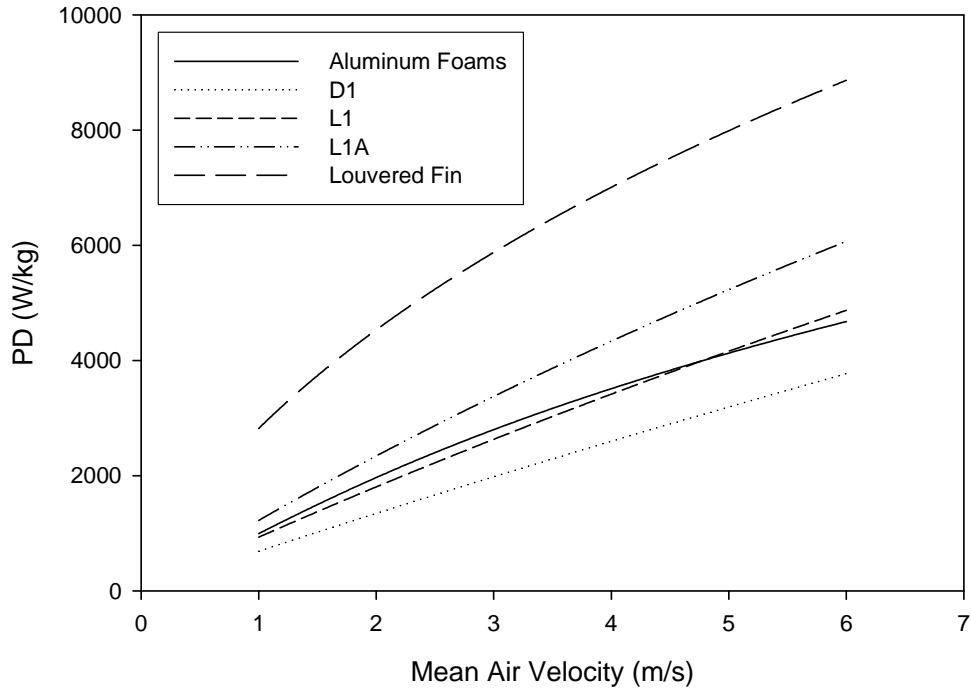


Figure 5-17. Comparison of power density for louvered fin and foam configurations

Fig. 5-16 shows that the CF is highest for the D1 carbon foam sample. This is a result of several factors. One is the high thermal conductivity of the carbon foam that helps to increase the fin efficiency. Another is due to finite leakage through the pores, which provides a large surface area in contact with the air and a tortuous flow path that induces mixing. As seen in Fig. 5-17 however, the power density is largest for the louvered fins. This is due to the relatively low density of the louvered fin configuration. It is interesting to note that the CF for the louvered fin configuration drops off more rapidly than the foam samples at low air velocity. This could be because at low fluid velocity, or low Reynolds number, the thermal boundary layer will be largest, at which point it is advantageous to break up the boundary layer frequently. At high Reynolds number however, the boundary layer will be smaller, and the effects of the added mixing will be marginal. Therefore it should be expected that a foam structure with a tortuous flow path will provide better heat transfer rates at low Reynolds number than a louvered fin configuration that is less effective in breaking up the thermal boundary layer.

CHAPTER 6 CONCLUSIONS

The work presented here encompasses the development of an advanced high power density thermal management system for PEM fuel cells that significantly increases the heat removal capacity while decreasing the required pumping power compared with other state of the art techniques. Analytical design tools have been developed for two-phase thermosyphon thermal management systems, which should prove useful to designers to optimize for power and energy density. An extensive investigation into the performance of a microchannel evaporator plate has contributed significantly to the overall understanding of the thermal hydraulics encountered in small channels. It is envisioned that this work will prove very useful to NASA for the development and implementation of innovative thermal management systems suitable for space exploration.

A microchannel evaporative cooling plate thermosyphon facility has been developed to remove waste heat from PEM fuel cell stacks. The overall performance of the evaporator plate is excellent. The plate operates in a natural circulation two-phase thermosyphon, and the thermal capacity for the current microchannel plate varies between 39 and 62 kW/m², depending on the condenser height, which far exceeds the heat flux currently being rejected from PEM fuel cell stacks. The plate wall temperatures range from 66-82 °C, depending on heat flux and position on the plate. A thermal hydraulic model has been presented which gives a satisfactory prediction of the mass flow rate, pressure drop, and microchannel plate thermal field. Similarly, the quasi-steady behavior of a two-phase microchannel thermosyphon has been investigated to obtain a quantitative understanding of the onset of unstable flow phenomenon observed at large heat fluxes. Static instabilities are largely influenced by the height of the condenser and stochastic variations in flow rate. A one-dimensional momentum equation-based model has been presented

to provide a framework for predicting the onset of the instability. Reasonable agreement is obtained between the observed and predicted instability limiting heat flux. The overall thermal hydraulic model describing the microchannel evaporator plate is found to be suitable for design and analysis applications.

In order to improve overall power/energy density of a PEM fuel cell, it is beneficial to integrate an air cooled condenser with a large COP, CF, and PD within the thermosyphon. This work evaluated the air side heat transfer performance of three aluminum foam and three carbon foam samples to gain insight into the heat removal capabilities and pressure drop requirements of the various foam samples and to compare against conventional louvered fin configurations. Correlations for computing the pressure drop and volumetric heat transfer coefficient based on the geometric properties of the foam have been provided. To better quantify the heat transfer performance of these foam samples, comparison with conventional louvered fin geometries has been made using a COP, CF, and PD as the basis for comparison. Results show the carbon foam samples provide significant improvement in CF but the COP and PD are considerably lower. The highest COP and PD are achieved with the multi-louvered fin configuration; however the resulting CF is substantially lower than that for carbon foam. In conclusion, carbon foam performs better than conventional plate-fin heat exchangers in applications where a reduced heat exchanger volume is favored over reduced mass and/or COP, but in cases where reduced mass and/or enhanced COP are important, a multi-louvered fin type configuration proves to be more advantageous. In conclusion, these correlations, along with the thermal hydraulic model of the evaporator plate are expected to contribute to further optimization of the microchannel thermosyphon with respect to both power and energy density.

APPENDIX A INSTABILITY IDENTIFICATION

In order to accurately predict the onset of instability, it is first important to identify the mechanism causing the phenomenon. By ruling out various instabilities one by one, identification can be achieved. Using the classification of Boure et al. (1973), several mechanisms can be ruled out. For instance the boiling crisis has been observed to occur simultaneously with flow oscillations (Boure et al. 1973) and does not occur prior to any instability. Since oscillations in flow rate themselves result in oscillations in vapor quality, the critical heat flux (CHF), may occur at a lower heat flux than would occur under constant flow rate conditions. In general, the boiling crisis is an unfavorable consequence of flow instability and therefore is not in itself a mechanism for the onset of instability. However, special consideration must be made when considering two-phase flow in narrow spaces. Since the channels under investigation have a 1 mm x 1 mm cross section, it possible that the CHF occurs at a lower heat flux than found in larger channels. Brutin & Tadrist (2004) show that the instability does not occur when the slope of pressure drop versus flow rate is negative as is the case in the current investigation.

Flow pattern transition occurs near the transition from bubbly to slug flow. Since the pressure drop in annular flow is less than that for bubbly flow, the transition can result in a sudden increase in flow rate. This in turn will cause a decrease in void fraction and the flow will revert back to a bubbly regime and the cycle is repeated. This phenomenon is not observed in the current experiments. The riser section of the system is observed to be in the annular flow regime prior to instability, and does not oscillate between regimes until after the flow goes unstable. Another possible mechanism for instability is bumping, chugging, or geysering. These phenomenons are a result of a lack of nucleation sites. Under these conditions, large quantities

of superheat build up. At this point, nucleation sites appear and the wall temperature is reduced. If the working fluid has a good wettability, the nucleation sites will diminish and the cycle repeats. This frequent change in the number of nucleation sites causes a fluctuation in vapor quality, and in turn causes oscillations in flow rate. This can be ruled out in the current experiment since vigorous boiling is observed at heat fluxes relatively far below the heat flux at the onset of instability.

Acoustic oscillations are a result of the propagation of pressure disturbances along the heated channel. The frequencies of these oscillations are generally large, and the amplitude small (Boure et al. 1973) compared to those found in the current experiment. These low amplitude high frequency fluctuations may be occurring prior to the large scale instabilities but are of no real interest here. This paper focuses on large scale, system instabilities that can cause a boiling crisis and eventually system failure.

Density wave oscillations are explained by propagation time lags describing the flow rate, vapor generation rate, and pressure drop within the system. A more detailed description of density wave oscillations is described by Yadigaroglu and Bergles (1981). Kakac and Bon (2008) provide an instability map, and show that density wave oscillations occur when the slope of pressure drop versus flow rate is positive. The current investigation shows that the instability arises when the slope of pressure drop versus flow rate is negative. Therefore, the density wave oscillations can be ruled out.

Thermal oscillations have been identified by Stenning and Veziroglu (1967) to be associated with the thermal response of the heated wall after dryout much like the CHF type instabilities found in small channels. Boure (1973), Kakac & Bon (2008), have shown that this type of oscillation requires an interaction with high frequency density wave oscillations that act

as disturbances to destabilize film boiling. Since density wave oscillations are not present in the current experiments, thermal oscillations can be ruled out as well. BWR type instabilities are specific to nuclear reactors and involve the coupling of fuel dynamics. It is obvious that these phenomena do not occur in the thermosyphon facility used here for testing. Finally, parallel channel instabilities occur when the test section is comprised of two or more parallel channels. The test section used in this experiment is not susceptible to this phenomenon since each channel is connected. Due to the fabrication process used to manufacture the test section to allow for flow visualization, a small amount of fluid is able to flow between channels, eliminating the possibility of any parallel channel instability.

After ruling out several mechanisms for the onset of instability, the remaining possibilities include Ledinegg instability, pressure drop oscillations, and natural circulation instability. Both pressure drop oscillations and natural circulation instability are first triggered by the static instability (Ledinegg) before becoming dynamic. Since both pressure drop oscillations and natural circulation instability are a direct result of Ledinegg instability, the onset of these types of instability can be determined by successfully predicting the onset of Ledinegg instability. However, it is reasonable to assume that the observed dynamics are not largely due to pressure drop oscillations since the compressible volume is rather small. Throughout the loop there exists a compressible volume in both the condenser and the riser. Therefore, in order for the vapor to compress within the condenser an equal amount of vapor will have to expand within the riser in order to obtain a mass balance. Therefore even for the case where the density fluctuations within the riser and condenser are perfectly out of phase, the overall compressibility of the system is limited by the compressibility within the riser.

APPENDIX B UNCERTAINTY AND CALIBRATION

In order to gage the accuracy of the various measurements, such as temperature, pressure drop, flow rate, heat flux, and vapor quality, the uncertainty in these parameters must be estimated. Uncertainties exist in the various devices, such as thermocouples, pressure transducers, volt meters and amp meters, along with uncertainties from the data acquisition board and calibration curves. This section focuses on both the calibration procedures as well as the associated errors relating to each measurement.

Data Acquisition (DAQ)

The data acquisition signal is read using a Measurement and Computing CIO-EXP32 multiplexer and a PCIM-DAS1602/16 bit analog to digital (AD) converter. For each measurement 500 samples are taken at 1 Hz, the data are averaged, and voltage is recorded. The measurement is repeated 3 times to insure repeatability. When measuring voltage for thermocouples, the voltage input is on the order of mV. The multiplexer takes the millivolt signal and applies an appropriate gain before it is sent to the AD board. The absolute error associated with this process is estimated by the manufacturer to be $\varepsilon_{MP}/V = 0.2\%$. The maximum voltage signal recorded after the gain is applied for the range of temperatures measured in these experiments is 3 V. Therefore the maximum error associated with the thermocouples from the multiplexer is $\varepsilon_{MP} = .006V$. After the signal passes through the multiplexer it is sent to the AD board where quantization error arises. The quantization error of the AD board is defined as,

$$\varepsilon_{qe} = \pm \frac{1}{2} \left(\frac{V_{\max} - V_{\min}}{2^N} \right), \quad (\text{B-1})$$

where $V_{\max} - V_{\min}$ is the voltage range given to that specific channel and N is the number of bits which in this case is 16. The highest voltage range assigned to any channel is 20 volts, and the resulting quantization error is approximately, $\varepsilon_{qe} = 1.53 \times 10^{-4} V$. Due to the high resolution of the AD board, the quantization error is negligible. Using the Kline-Mcclintock method, the total voltage error from the DAQ is shown to be,

$$\varepsilon_V = \sqrt{\varepsilon_{qe}^2 + \varepsilon_{MP}^2} = 0.006V . \quad (\text{B-2})$$

For all channels that do not require gain, the error associated with the DAQ system is estimated to come only from the quantization error. Since the quantization error is so small, it is neglected for simplicity.

Pressure Drop

The pressure drop is measured using a Validyne differential pressure transducer model # DP-15-32. For each pressure measurement a different diaphragm was used, all having a different range. The manufacturer specified relative uncertainty of the transducer is $\varepsilon_{PT} / \Delta P = .25\%$ of full scale. The pressure transducer is directly calibrated to a monometer using R827 oil as the fluid. The smallest increment on the monometer is 1 mm, therefore the error associated with reading the monometer, ε_H , is estimated to be 0.5 mm. Since $P = \rho g H$, the Kline-Mcclintock method shows that the uncertainty in the monometer is, $\varepsilon_m = \rho g \varepsilon_H$.

The calibration process involves adding pressure to the monometer, recording the voltage signal and pressure drop, increasing the monometer pressure incrementally and repeating the process until sufficient data is recorded. The resulting pressure drop versus voltage calibration curves are shown for each pressure transducer below in Figs. B-1a – B-1c.

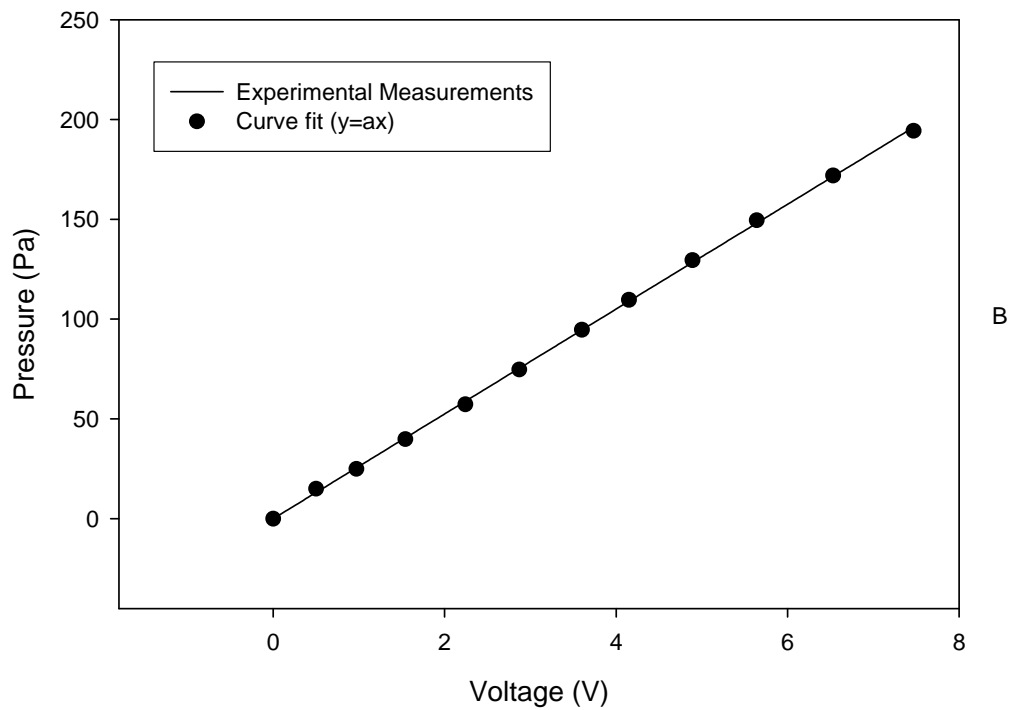
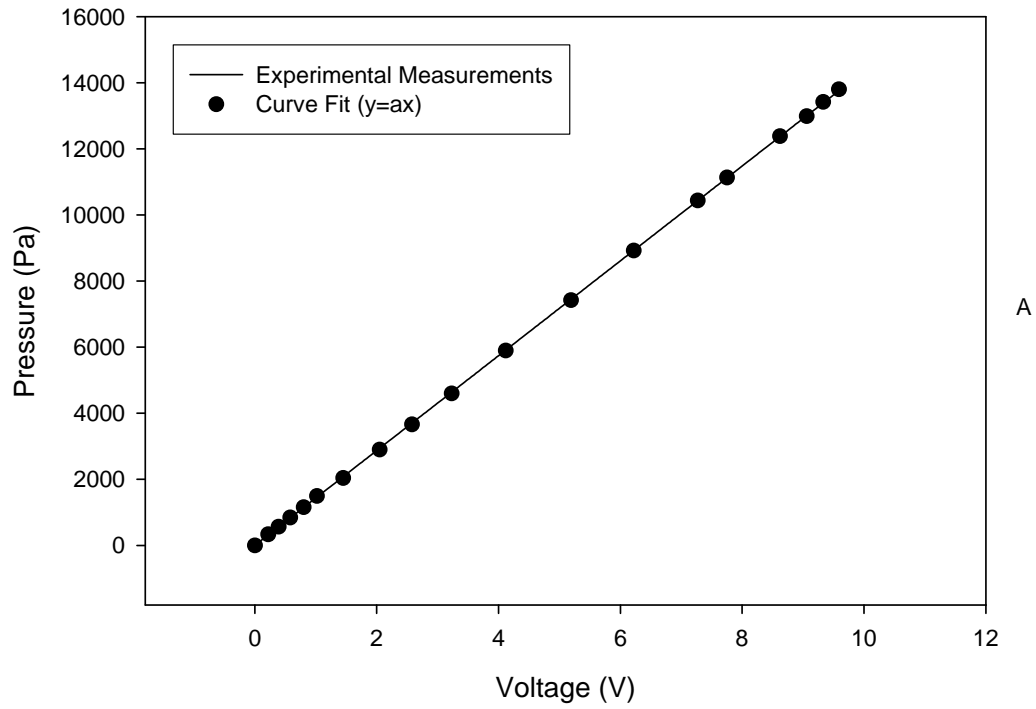


Figure B-1. Pressure drop calibration curve used for measurement of pressure drop. A) Venturi flow meter (PT1). B) Pitot tube (PT2). C) Pressure drop across both microchannel plate and foam samples (PT3).

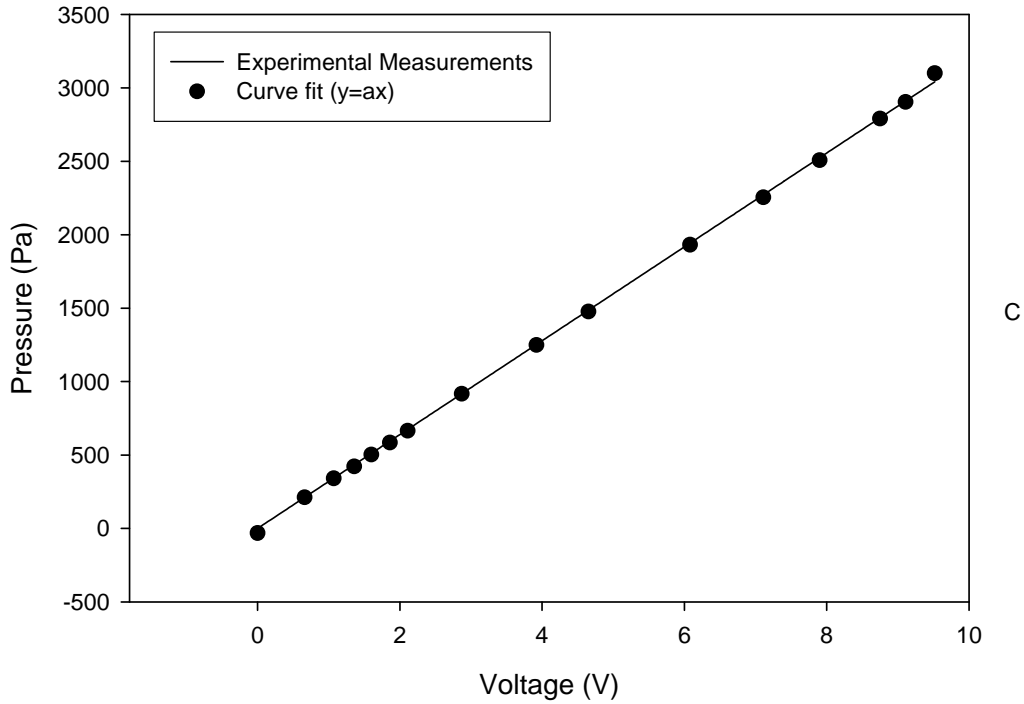


Figure B-1 Continued.

The standard error of the estimate, ε_{est_p} , is computed from the following equation,

$$\varepsilon_{est_p} = \sqrt{\frac{\sum (P_m - P_c)^2}{N}}, \quad (B-3)$$

where P_m is the measured pressure and P_c is the pressure estimated by the calibration curve.

The total error is taken as the root sum of squares of the standard error of the estimate, the error of the monometer and the error of the pressure transducer,

$$\varepsilon_p = \sqrt{\varepsilon_m^2 + \varepsilon_{est_{\Delta P}}^2 + \varepsilon_{PT}^2}. \quad (B-4)$$

The sensitivity, a , of each pressure transducer is listed below in table B-1, where PT1 is the pressure transducer used for measurement of pressure drop across the venturi flow meter, PT2 is the pressure transducer used for measurement of pressure drop across the pitot tube, and PT3 is

the pressure transducer used for measurement of pressure drop across both the microchannel plate and the foam samples.

Table B-1. Diaphragm maximum pressure, sensitivity parameter, and standard error of the estimate for each pressure transducer.

	ΔP_{\max} (Pa)	a (Pa/V)	$\varepsilon_{est,\Delta P}$ (Pa)
PT1	14000	1435.0	54.5
PT2	860	26.3	1.1
PT3	3500	319.5	32

Flow Meter Calibration

The flow meter used here is a venturi flow meter manufactured by Gerand Engineering Company. The calibration procedure involves pumping the working fluid, HFE-7100, through the venturi flow meter and recording the pressure drop directly. Once the fluid passed through the flow meter it is discharged into a graduated cylinder. Using a stopwatch, the time required to fill the graduated cylinder to the level of 800 ml is recorded along with the pressure drop simultaneously. The mass flow rate is then computed from the following equation,

$$\dot{m} = \frac{\rho Vol}{t} . \quad (B-5)$$

Where ρ is the fluid density, Vol is the volume of the cylinder filled up by the fluid, and t is the time it takes to fill the cylinder. The pressure drop is measured using a Validyne differential pressure transducer. The error associated with the pressure transducer is given in Eq. (B-2). The error associated with the stopwatch, ε_{sw} , is estimated to be ± 0.2 s. The smallest increment on the graduated cylinder is 10 ml, therefore the estimated uncertainty in the volume reading from the graduated cylinder, ε_{gc} , is ± 5 ml. Using the Kline-Mcclintock method, the error in the mass flow rate is calculated from the following equation assuming zero error in the fluid density,

$$\varepsilon_{m,c} = \sqrt{\left(\frac{\rho}{t} \varepsilon_{gc}\right)^2 + \left(\frac{\rho Vol}{t^2} \varepsilon_{sw}\right)^2} . \quad (B-6)$$

The measured flow rate is then calibrated directly to the measured pressure drops and is shown below in Fig. (B-2). The equation for flow rate versus pressure drop is given in En. (B-7).

$$\dot{m}_c = A\Delta P^b \quad (\text{B-7})$$

where $A = 3.138 \times 10^{-4}$ and $b = 0.516$.

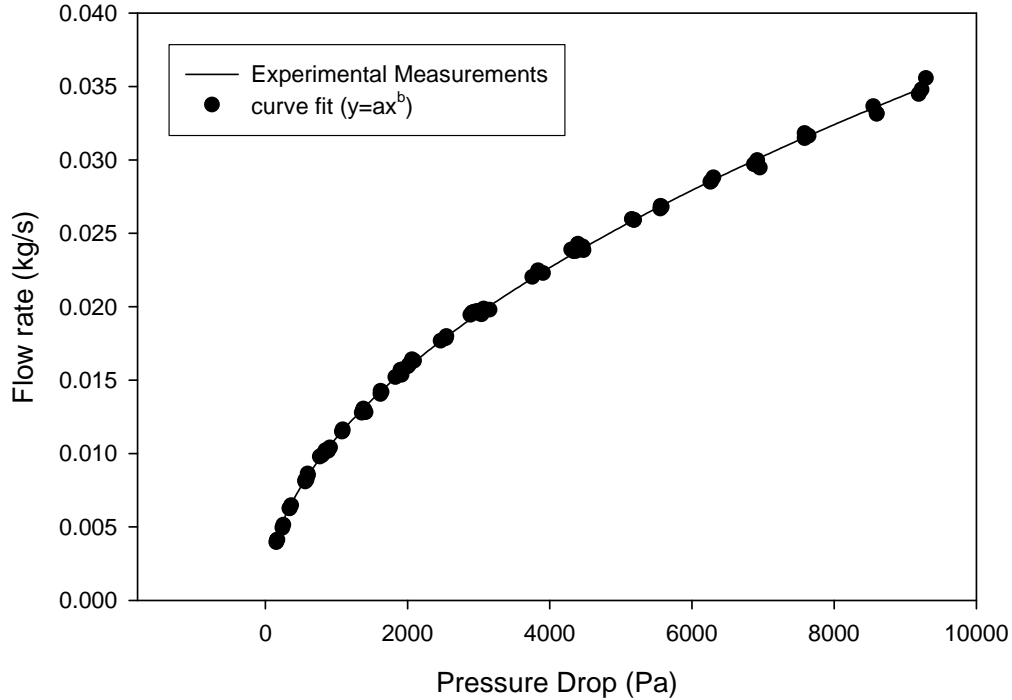


Figure B-2. Flow rate versus pressure drop calibration curve used for measurement of flow rate within the venturi flow meter.

The standard error of the estimate is computed from,

$$\epsilon_{est_m} = \sqrt{\frac{\sum (\dot{m}_m - \dot{m}_c)^2}{N}} = 2.581 \times 10^{-4}, \quad (\text{B-8})$$

where \dot{m}_m is the measured mass flow rate and \dot{m}_c is the mass flow rate estimated by the calibration curve. During the actual experiments, the pressure drop across the venturi is measured and the resulting flow rate is computed from the calibration curve. Since the error in the pressure drop device shows up in both the original calibration as well as in the actual

experiments, this error is accounted for twice in the overall uncertainty of the flow meter. The total uncertainty is given as,

$$\varepsilon_{\dot{m}} = \sqrt{\varepsilon_{m,c}^2 + \varepsilon_{est_{\dot{m}}}^2 + 2\left(\frac{\partial \dot{m}}{\partial \Delta P} \varepsilon_P\right)^2}, \quad (B-9)$$

where $\frac{\partial \dot{m}}{\partial \Delta P}$ is computed from the calibration curve. After some manipulation, Eq. (B-9) can be

shown in the following form,

$$\varepsilon_m = \sqrt{\left(\frac{\dot{m}}{Vol} \varepsilon_{gc}\right)^2 + \left(\frac{\dot{m}^2}{\rho Vol} \varepsilon_{SW}\right)^2 + \varepsilon_{est_{\dot{m}}}^2 + \left(Ab \left[\left(\frac{\dot{m}}{A}\right)^{1/b}\right]^{b-1} \varepsilon_P\right)^2}. \quad (B-10)$$

After plugging in the quantitative values in Eq. (B-10), the error in flow rate can be determined as a function of flow rate only,

$$\varepsilon_m = \sqrt{(.0625\dot{m})^2 + (.1786\dot{m}^2)^2 + (2.581 \times 10^{-4})^2 + (.3474\dot{m}^{.726})^2}. \quad (B-11)$$

It is necessary to mention that flow rates extracted during the actual experiments are not taken directly from the flow rate versus pressure drop calibration found in Fig. B-2. Instead a Discharge Coefficient is extracted from the calibration curve to account for the frictional pressure drop across the venturi. By correlating the Discharge Coefficient with Reynolds number, the calibration curve can be corrected for temperature changes during experiment. Since the true flow rate versus pressure drop curve requires an iterative technique to solve for flow rate, the direct flow rate versus pressure drop calibration from Fig. B-2 was used here in the uncertainty analysis for simplification.

Uncertainty in Power Measurement

The heat input is determined from direct measurements of voltage and current. The voltmeter is a Keithley model 177 microvolt dmm with a manufacturers estimated relative

uncertainty of $\varepsilon_{VM}/V = 0.3\%$. The amp meter is a MPJA model 9903 having a manufacturers estimated relative uncertainty of $\varepsilon_{AM}/I = 2\%$. Using the Kline-Mcclintock method, the relative uncertainty in power is taken to be,

$$\frac{\varepsilon_Q}{VI} = \sqrt{\left(\frac{\varepsilon_{VM}}{V}\right)^2 + \left(\frac{\varepsilon_{AM}}{I}\right)^2} . \quad (\text{B-12})$$

Temperature

The temperature sensors used are type-E thermocouples from Omega. The manufacturers estimated uncertainty is given as $\varepsilon_{TC} = 1.7^\circ\text{C}$. Each thermocouple is calibrated in a bath with a mercury thermometer. The smallest increment on the thermometer is 0.1°C , therefore the estimated uncertainty in the thermometer measurement, ε_{MC} , is $\pm 0.05^\circ\text{C}$. The thermocouples are placed in the bath within 3 cm. distance of the thermometer. The heat flux is raised in increments and the bath is allowed to reach a steady state temperature. At each increment, the voltage signal is taken directly from the data acquisition and the temperature is simultaneously recorded from the thermometer. Since the voltage read from the data acquisition board is read as the difference in voltage between the junction on the board and the thermocouple probe, the temperature reading is read as the difference in temperature between the thermocouple probe and the data acquisition board. The temperature of the data acquisition board is measured at the junction using a thermister. The manufacturers estimated relative uncertainty in the thermister, ε_{TM} , is $\pm 0.025^\circ\text{C}$. When calibrating the board, the junction temperature reading is adjusted to match the ambient air temperature, which is measured using the mercury thermometer. Therefore the error in the junction temperature is defined as the root mean sum of squares of the error in the thermister, the error in the thermometer, and the error in temperature due to the error in the DAQ voltage reading,

$$\varepsilon_{JT} = \sqrt{\varepsilon_{TH}^2 + \varepsilon_{TM}^2 + \left(\frac{\partial T}{\partial V} \varepsilon_V\right)^2}. \quad (\text{B-13})$$

The following calibration curve is plotted relating the temperature directly to voltage.

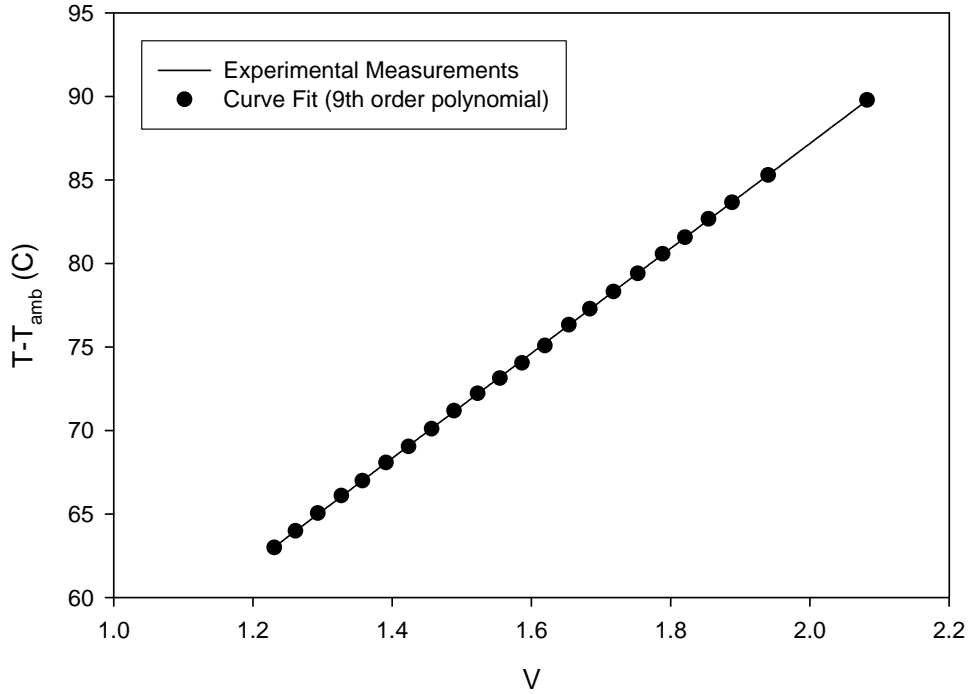


Figure B-3. Temperature calibration curve for a type-E thermocouple.

The standard error of the estimate is computed from,

$$\varepsilon_{est_{\Delta T}} = \sqrt{\frac{\sum (\Delta T_m - \Delta T_c)^2}{N}} = .05^\circ C, \quad (\text{B-14})$$

where ΔT_m is the measured temperature difference between the bath and the junction and ΔT_c is that estimated by the calibration curve. Using the Kline-Mcclintock method, the total uncertainty in the thermocouples is estimated as,

$$\varepsilon_T = \sqrt{\varepsilon_{TH}^2 + \varepsilon_{est_{\Delta T}}^2 + \varepsilon_{JT}^2 + \varepsilon_{TC}^2 + \left(\frac{\partial T}{\partial V} \varepsilon_V\right)^2}. \quad (\text{B-15})$$

Various Parameters

Once the uncertainty in all direct measurements, pressure, flow rate, power, and temperature, are known, the error from other various parameters can be determined.

Wall Temperature

Since the distance between the microchannel wall and the thermocouple probe has some uncertainty, the error in all wall temperature measurements, ε_{T_w} , is computed as follows,

$$T_w = T_m - \frac{\dot{q}t}{kA_c} \quad (\text{B-16})$$

$$\varepsilon_{T_w} = \sqrt{\varepsilon_T^2 + \left(\frac{t}{k_a A_c} \varepsilon_{\dot{q}}\right)^2 + \left(\frac{\dot{q}}{k_a A_c} \varepsilon_t\right)^2}. \quad (\text{B-17})$$

Vapor Quality

The vapor quality is computed from an energy balance,

$$x = \frac{\dot{q} - \dot{m}C_p(T_{out} - T_{in})}{\dot{m}h_{fg}}, \quad (\text{B-18})$$

Since the vapor quality, x , is a function of heat input, temperature, and flow rate, the error in vapor quality must be accounted for accordingly. The equation is shown here as,

$$\varepsilon_x = \sqrt{\left(\frac{1}{\dot{m}h_{fg}} \varepsilon_{\dot{q}}\right)^2 + \left(\frac{\dot{q}}{2h_{fg}\dot{m}^2} \varepsilon_{\dot{m}}\right)^2 + 2\left(\frac{C_p}{h_{fg}} \varepsilon_T\right)^2}. \quad (\text{B-19})$$

Vapor Superficial Velocity

Similarly, the error is computed for the vapor superficial velocity that results from both the flow rate and vapor quality as well as the error in the pitot tube velocity that results from the pressure drop uncertainty.

$$u_v = \frac{\dot{m}x}{A_c \rho_v} \quad (\text{B-20})$$

$$\varepsilon_{u_v} = \sqrt{\left(\frac{x}{A_c \rho_v} \varepsilon_{\dot{m}}\right)^2 + \left(\frac{\dot{m}}{A_c \rho_v} \varepsilon_x\right)^2} \quad (\text{B-21})$$

Pitot Tube Velocity

$$u_m = \frac{1}{1.2} \sqrt{\frac{2\Delta P}{\rho_{air}}} \quad (\text{B-22})$$

$$\varepsilon_{u_m} = \frac{1}{1.2} \sqrt{\frac{1}{2\rho_{air}\Delta P}} \varepsilon_P \quad (\text{B-23})$$

APPENDIX C
PRESSURE GRADIENT AND HEAT TRANSFER DATA FOR FOAM SAMPLES

Table C-1. Pressure gradient for different foams.

D1		L1		L1A		10 PPI		20 PPI		40 PPI	
u_m	dP/dz	u_m	dP/dz	u_m	dP/dz	u_m	dP/dz	u_m	dP/dz	u_m	dP/dz
(m/s)	(Pa/m)	(m/s)	(Pa/m)	(m/s)	(Pa/m)	(m/s)	(Pa/m)	(m/s)	(Pa/m)	(m/s)	(Pa/m)
0.6	282	0.5	226	0.9	338	1.1	339	1.0	316	1.0	442
0.9	382	0.7	298	1.0	435	1.5	525	1.2	457	1.2	659
1.4	689	1.1	503	1.4	705	1.9	910	1.7	804	1.6	1080
1.8	1271	1.8	1083	1.7	1103	2.4	1520	2.2	1343	2.2	1930
2.2	1921	2.4	1819	2.1	1558	2.9	2199	2.6	1985	2.6	2670
2.6	2570	2.7	2475	2.3	1973	3.5	3035	3.1	2708	3.1	3652
3.1	3324	3	3051	2.6	2309	3.9	3763	3.6	3386	3.6	4596
3.4	4040	3.4	3680	3.0	3064	4.3	4562	4.0	4149	4.0	5426
3.6	4517	3.6	4101	3.3	3644	4.6	5152	4.3	4640	4.2	6090
3.8	4947	3.7	4463	3.4	3953	4.9	5653	4.5	5077	4.4	6670
3.8	5191	3.8	4695	3.8	4849	5.0	5934	4.6	5408	4.6	7033

Table C-2. Volumetric heat transfer coefficient and upper fall temperature for different foams.

L1A			D1			L1		
u_m (m/s)	h_v (W/m ³ K)	$T_{w,u}$ (°C)	u_m (m/s)	h_v (W/m ³ K)	$T_{w,u}$ (°C)	u_m (m/s)	h_v (W/m ³ K)	$T_{w,u}$ (°C)
1.6	12364	73.0	1.5	10148	79.6	1.5	10497	77.6
2.1	20458	55.6	2.1	13586	65.2	2.0	15153	61.4
2.6	32539	46.2	2.6	19374	54.2	2.5	21689	51.0
3.2	39497	42.1	3.2	24076	48.4	3.1	27058	45.7
3.7	46448	39.3	3.6	27813	45.1	3.5	31775	42.3
4.2	50438	37.8	4.1	29818	43.2	3.9	33972	40.7
4.6	54321	36.6	4.5	32247	42.0	4.4	36414	39.4
4.9	54428	36.2	4.8	33654	40.8	4.6	37285	38.6
10 PPI			20 PPI			40 PPI		
u_m (m/s)	h_v (W/m ³ K)	$T_{w,u}$ (°C)	u_m (m/s)	h_v (W/m ³ K)	$T_{w,u}$ (°C)	u_m (m/s)	h_v (W/m ³ K)	$T_{w,u}$ (°C)
1.2	12923	59.4	1.1	15552	70.2	0.7	23016	88.7
1.8	26779	44.7	1.7	35774	47.8	1.2	42191	57.4
2.4	45288	37.8	2.2	58228	39.8	1.7	66727	45.3
3.3	70038	33.1	3.0	104675	33.9	2.3	103577	38.3
3.9	89111	31.0	3.5	155029	31.3	2.8	137817	35.0
4.5	101196	29.7	4.2	215088	29.7	3.3	171021	33.2
5.0	116760	29.1	4.8	286133	28.6	3.8	179321	31.7
5.7	122192	28.6	5.2	372559	27.9	4.1	186646	31.1

APPENDIX D
NUMERICAL CODE FOR SOLVING POROUS MEDIA TRANSPORT EQUATIONS

```
#include <iostream>
#include <stdlib.h>
#include <math.h>
#include <stdio.h>
#include <fstream>
#include <gsl_linalg.h>
#include "gsl_errno.h"
#include "gsl_message.h"
using namespace std;
int i;
int j;
int k;
int n;
int m;
int it;
int iter;
int iterTTT;
double Thetas[512][512];
double Thetaf[512][512];
double Ts[512][512];
double Tf[512][512];
double kf;
double kfe;
double alphaf;
double resolutiony;
double u[512][512];
double v[512][512];
double ErrorU;
double Lal;
double Lar;
double La;
double U[512];
double Int[512];
double qw;
double Bi[512];
double Stint[512];
double Re[512];
double Da[512];
double eta[512];
double a[512];
double aa[512];
double b[512];
double bb[512];
double c[512];
```

```
double cc[512];
double d[512];
double dd[512];
double Pr[512];
double ST[512];
double nu;
double C;
double qs;
double qf;
double qint[512];
double qwp;
double dy;
double y[512];
double Tend[512];
double ErrorT;
double Tb[512];
double ErrorTb;
double hr;
double hl;
double Ac;
double As;
double LL;
double Tinf[512];
double L;
double x[512];
double xp[512];
double yp[512];
double dxp;
double dyp;
double resolutionx;
double dx;
double H;
double ErrorTT;
double TTend[51200];
double Tin;
double Theta0;
const double pi = 3.14159265358979323846;
double Nu[512];
double Errorh;
double EB;
double LaA;
double LaB;
double LaC;
double LaD;
double uu[512];
double yy[512];
```

```

double yyp[512];
double alphas[512];
double gammas[512];
double zs[512];
double alphaff[512];
double gammaf[512];
double zf[512];
double resolutionu;
double umax;
double du;
double Ewall[512];
double Eint[512];
double Eint1[512][512];
double Eint2[512][512];
double Eint3[512];
double Eint4[512];
double Es[512];
double Eh[512];
double Eh1[512];
double Eh2[512];
double Eh3[512];
double Tbo[512];
double Tbo1[512];
double Tbo2[512];
double Tbi[512];
double Tbi1[512];
double Tbi2[512];
double rhof = {1.16};
double Cpf = {1030};
double mu = {1.85E-6};
double dyy;
//10 PPI
//double K = {1.98E-8};
//double epsilon = {0.918};
//double kse = {9.778651};
//double asf = {1};
//double Cf = .027;
//double Texp;
//double h[512];
//double Um[512];
//20 PPI
//double K = {1.21E-8};
//double epsilon = {0.918};
//double kse = {9.778651};
//double asf = {1};
//double Cf = .021;

```

```

//double Texp;
//double h[512];
//double Um[512];
//40 PPI
double K = {6.98E-9};
double epsilon = {0.918};
double kse = {9.778651};
double asf = {1};
double Cf = .02;
double Texp;
double h[512];
double Um[512];
//L1A
//double K = {1.66E-8};
//double epsilon = {0.166};
//double kse = {48.62};
//double asf = {1};
//double Cf = .034;
//double Texp;
//double h[512];
//double Um[512];
//double dp = {.0005};
//D1
//double K = {1.66E-8};
//double epsilon = {0.166};
//double kse = {97.24};
//double asf = {1};
//double Cf = .034;
//double Texp;
//double h[512];
//double Um[512];
//double dp = {.00065};
//L1
//double K = {1.66E-8};
//double epsilon = {0.166};
//double kse = {61.88};
//double asf = {1};
//double Cf = .034;
//double Texp;
//double h[512];
//double Um[512];
//double dp = {.0006};
//-----
void WriteU(void)
{
    ofstream file;

```

```

file.open("Velocity.m");
file << "u = [";
for (int n = 0; n <= ((int)resolutiony); n++)
{
    file << u[1][n] << " ";
    if (n == ((int)resolutiony))
        file << "];";
    else
        file << std::endl;
}
}
//-----
void WriteY(void)
{
    ofstream file;
    file.open("YY.m");
    file << "yp = [";
    for (int n = 0; n <= ((int)resolutiony); n++)
    {
        file << y[n] << " ";
        if (n == ((int)resolutiony))
            file << "];";
        else
            file << std::endl;
    }
}
//-----
void WriteX(void)
{
    ofstream file;
    file.open("XX.m");
    file << "xp = [";
    for (int n = 0; n <= ((int)resolutionx); n++)
    {
        file << x[n] << " ";
        if (n == ((int)resolutionx))
            file << "];";
        else
            file << std::endl;
    }
}
//-----
void WriteTs(void)
{
    ofstream file;
    file.open("Temps.m");

```

```

file << "TTs = [";
for (int n = 0; n <= resolutionx; n++)
{
    for (int m = 0; m <= resolutiony; m++)
    {
        file << Ts[n][m] << " ";
    }
    if (n == resolutionx)
        file << "];";
    else
        file << std::endl;
}
}
//-----
void WriteTf(void)
{
    ofstream file;
    file.open("Tempf.m");
    file << "TTf = [";
    for (int n = 0; n <= resolutionx; n++)
    {
        for (int m = 0; m <= resolutiony; m++)
        {
            file << Tf[n][m] << " ";
        }
        if (n == resolutionx)
            file << "];";
        else
            file << std::endl;
    }
}
//-----
void Writeh(void)
{
    ofstream file;
    file.open("Heat.m");
    file << "h40PPI = [";
    for (int k = 0; k <= resolutionu; k++)
    {
        file << h[k] << " ";
        if (k == resolutionu)
            file << "];";
        else
            file << std::endl;
    }
}
}

```

```

//-----
void WriteUm(void)
{
    ofstream file;
    file.open("MeanV.m");
    file << "Um40PPI = [";
    for (int k = 0; k <= resolutionu; k++)
    {
        file << Um[k] << " ";
        if (k == resolutionu)
            file << "];";
        else
            file << std::endl;
    }
}
//-----
void Writejunk(void)
{
    ofstream file;
    file.open("junk.m");
    file << "c = [";
    for (int k = 0; k <= (int)resolutiony; k++)
    {
        file << c[k] << " ";
        if (k == (int)resolutiony)
            file << "];";
        else
            file << std::endl;
    }
}
//-----
void Writejunk2(void)
{
    ofstream file;
    file.open("junk2.m");
    file << "a = [";
    for (int k = 0; k <= (int)resolutiony; k++)
    {
        file << a[k] << " ";
        if (k == (int)resolutiony)
            file << "];";
        else
            file << std::endl;
    }
}
void Writejunk3(void)

```

```

{
    ofstream file;
    file.open("junk3.m");
    file << "b = [";
    for (int k = 0; k <= (int)resolutiony; k++)
    {
        file << b[k] << " ";
        if (k == (int)resolutiony)
            file << "];";
        else
            file << std::endl;
    }
}
void Writejunk4(void)
{
    ofstream file;
    file.open("junk4.m");
    file << "d = [";
    for (int k = 0; k <= (int)resolutionu; k++)
    {
        file << Eh[k] << " ";
        if (k == (int)resolutionu)
            file << "];";
        else
            file << std::endl;
    }
}
//-----
void GenerateMesh(void)
{
    resolutiony=64;
    H=0.06;
    L=.1;
    dyp=(H/L)/resolutiony;
    dy=H/resolutiony;
    y[0]=0;
    yp[0]=0;
    for ( n = 1; n <= resolutiony; n++)
    {
        y[n]=y[n-1]+dy;
        yp[n]=yp[n-1]+dyp;
    }
    resolutionx=64;
    dx=L/resolutionx;
    dxp=1/resolutionx;
    xp[0]=0;

```

```

x[0]=0;
for ( n = 1; n <= resolutionx; n++)
{
    x[n]=x[n-1]+dx;
    xp[n]=xp[n-1]+dxp;
}
dyy = H/(resolutiony);
yy[0] = 0;
for (n = 1; n<= floor(resolutiony/2); n++)
{
    yy[n] = yy[n-1]+dyy;
    yyp[n] = yy[n]/(H/2);
}
resolutionu = 64;
umax = 6;
du = (umax-1)/resolutionu;
Um[0] = 1;
for (n = 1; n<= resolutionu; n++)
{
    Um[n] = Um[n-1]+du;
}
}
//-----
void Momentum(void)
{
    ErrorU=10;
    Lal=Um[k];
    Lar=2*Um[k];
    while (ErrorU>1E-3)
    {
        La=(Lal+Lar)/2;
        Da[k]=K/pow(H/2,2)*1/epsilon;
        eta[k]=pow(epsilon,1.5)*Cf/epsilon*La*H/2*rhof/mu;
        LaA = 2*eta[k]/3*pow(Da[k],-0.5);
        LaB = 1/Da[k]+4*eta[k]/3*pow(Da[k],-0.5);
        LaC = -1/LaD*acosh(sqrt((LaA+LaB)/LaA))-1;
        LaD = sqrt(LaA+LaB)/2;
        for ( n = 0; n <= floor(resolutiony/2); n++)
        {
            uu[n]=1-(LaA+LaB)/LaA*pow(1/cosh(LaD*(yyp[n]+LaC)),2);
        }
        Int[k]=(1-(LaA+LaB)/LaA*(tanh(LaD*(1+LaC))-tanh(LaD*LaC))/LaD)*La;
        ErrorU=fabs(Um[k]-Int[k]);
        if ((Um[k]-Int[k])<0)
        {
            Lar=La;

```

```

        }
        else
        {
            Lal=La;
        }
    }
    for (int it = 0; it <= resolutionx; it++)
    {
        for (int n = int(floor(resolutiony/2)); n <= int(resolutiony); n++)
        {
            u[it][n] = uu[int(n-floor(resolutiony/2))]*La/Um[k];
        }
        for (int n = 0; n <= floor(int(floor(resolutiony/2))); n++)
        {
            u[it][n] = uu[int(floor(resolutiony/2)-n)]*La/Um[k];
        }
    }
    std::cout<<"Momentum Complete"<<endl;
}
//-----
int TemperatureInit(void)
{
    for ( it = 0; it <= (int)resolutionx; it++)
    {
        for ( n = 0; n <= (int)resolutiony; n++)
        {
            Thetas[it][n] = 0;
            Thetaf[it][n] = 0;
        }
    }
}
//-----
int TemperatureLBY(void)
{
    {
        it = 0;
        for (n = 0; n <= (int)resolutiony; n++)
        {
            Thetas[it][n]=(4*Thetas[it+1][n]-Thetas[it+2][n])/3;
            Thetaf[it][n]=0;
        }
        for (i = 0; i <= (int)resolutiony; i++)
        {
            Ts[it][i]=Thetas[it][i]*(100-25)+25;
            Tf[it][i]=Thetaf[it][i]*(100-25)+25;
        }
    }
}

```

```

    }
    }
}
return 0;
}
//-----
int TemperatureMY(void)
{
{
for ( it = 1; it <= (int)resolutionx-1; it++)
{
for ( n = 0; n <= (int)resolutiony; n++)
{
b[n]=-2/(pow(dxp,2))+2/(pow(dyp,2))+Bi[k];
bb[n]=-
(2/(Re[k]*Pr[k]*pow(dxp,2))+2/(Re[k]*Pr[k]*pow(dyp,2))+Stint[k]+u[it][n]/(dyp));
}
for ( n = 0; n <= (int)resolutiony-1; n++)
{
a[n]=1/pow(dyp,2);
c[n]=1/pow(dyp,2);
aa[n]=(1/(Re[k]*Pr[k]*pow(dyp,2))+v[it][n]/(2*dyp));
cc[n]=-(v[it][n]/(2*dyp)-1/(Re[k]*Pr[k]*pow(dyp,2)));
}
a[0] = 0;
aa[0] = 0;
b[0] = 1;
b[(int)resolutiony] = 1;
a[(int)resolutiony] = 0;
c[0] = 0;
bb[0] = 1;
bb[(int)resolutiony] = 1;
aa[(int)resolutiony] = 0;
cc[0] = 0;
alphas[0] = b[0];
gammas[0] = c[0]/alphas[0];
for ( i = 1; i <= (int)resolutiony-1; i++)
{
alphas[i] = b[i]-a[i]*gammas[i-1];
gammas[i] = c[i]/alphas[i];
}
alphas[(int)resolutiony] = b[(int)resolutiony]-a[(int)resolutiony]*gammas[(int)resolutiony-
1];
alphaff[0] = bb[0];
gammaff[0] = cc[0]/alphaff[0];
for ( i = 1; i <= (int)resolutiony-1; i++)

```

```

{
  alphaff[i] = bb[i]-aa[i]*gammaff[i-1];
  gammaff[i] = cc[i]/alphaff[i];
}
alphaff[(int)resolutiony] = bb[(int)resolutiony]-
aa[(int)resolutiony]*gammaff[(int)resolutiony-1];
Tend[0]=-10;
ErrorT=10;
{
  for ( n = 1; n <= (int)resolutiony-1; n++)
  {
    d[n]=-(Bi[k]*Thetaf[it][n]+1/pow(dxp,2)*(Thetas[it+1][n]+Thetas[it-1][n]));
    dd[n]=-Stint[k]*Thetas[it][n]-1/(Re[k]*Pr[k]*pow(dxp,2))*(Thetaf[it+1][n]+Thetaf[it-
1][n])-u[it][n]/(dxp)*(Thetaf[it-1][n]);
  }
  d[0]=1;
  d[(int)resolutiony]=1;
  dd[0]=1;
  dd[(int)resolutiony]=1;
  zs[0] = d[0]/alphas[0];
  for ( i = 1; i <= (int)resolutiony; i++)
  {
    zs[i] = (d[i]-a[i]*zs[i-1])/alphas[i];
  }
  Thetas[it][(int)resolutiony] = zs[(int)resolutiony];
  for ( i = (int)resolutiony-1; i >= 0; i--)
  {
    Thetas[it][i] = zs[i]-gammass[i]*Thetas[it][i+1];
  }
  zf[0] = dd[0]/alphaff[0];
  for ( i = 1; i <= (int)resolutiony; i++)
  {
    zf[i] = (dd[i]-aa[i]*zf[i-1])/alphaff[i];
  }
  Thetaf[it][(int)resolutiony] = zf[(int)resolutiony];
  for ( i = (int)resolutiony-1; i >= 0; i--)
  {
    Thetaf[it][i] = zf[i]-gammaff[i]*Thetaf[it][i+1];
  }
  Tend[iter]=Thetas[(int)resolutionx/2][(int)resolutiony];

  ErrorT=fabs(Tend[iter]-Tend[iter-1]);
}
  for ( i = 0; i <= (int)resolutiony; i++)
  {
    Ts[it][i]=Thetas[it][i]*(100-25)+25;
  }

```



```

    Pr[k]=nu/alphaf;
Momentum();
TemperatureInit();
{
iterTTT=0;
TTend[0]=100;
ErrorTT=10;
EB=1E-12;
while (fabs(ErrorTT)>EB)
{
    iterTTT=iterTTT+1;
    nu=mu/rhof;
    kf=.0212;
    kfe=epsilon*kf;
    C=kse/kfe;
    alphaf=kfe/(rhof*Cpf);
    Tinf[k]=25;
    Stint[k]=h[k]*asf*L/(rhof*Cpf*Um[k]);
    Bi[k]=h[k]*asf*pow(L,2)/kse;
    Re[k]=Um[k]*L/nu;
    Pr[k]=nu/alphaf;
    TemperatureLBY();
    TemperatureMY();
    TemperatureRBY();
TTend[iterTTT]=Thetas[(int)resolutionx/2][(int)resolutiony/2]+Thetas[1][1]+Thetas[(int)resoluti
onx-1][(int)resolutiony-1];
    ErrorTT=(TTend[iterTTT]-TTend[iterTTT-1]);
}
std::cout<<"for k = "<<k<<"  HTC = "<<h[k]<<endl;
for ( n = 0; n <= (int)resolutiony-1; n++)
{
for ( it = 0; it <= (int)resolutionx-1; it++)
{
    Eint1[it][n]=h[k]*asf*(Ts[it][n]-Tf[it][n])*dx*dy;
}
}
for ( n = 0; n <= (int)resolutiony-1; n++)
{
Eint2[0][n] = Eint1[0][n];
for ( it = 0; it <= (int)resolutionx-1; it++)
{
Eint2[it+1][n] = Eint2[it][n]+Eint1[it+1][n];
}
Eint3[n] = Eint2[(int)resolutionx][n];
}
Eint4[0] = Eint3[0];

```

```

for ( n = 0; n <= (int)resolutiony-1; n++)
{
Eint4[n+1] = Eint4[n]+Eint3[n+1];
}
Eint[k] = Eint4[(int)resolutiony]*L;
for ( n = 0; n <= (int)resolutiony-1; n++)
{
Tbo1[n] = u[(int)resolutionx][n]*Um[k]*Tf[(int)resolutionx][n]*dy;
Tbi1[n] = u[0][n]*Um[k]*Tf[0][n]*dy;
}
Tbo2[0] = Tbo1[0];
Tbi2[0] = Tbi1[0];
for ( n = 0; n <= (int)resolutiony-1; n++)
{
Tbo2[n+1] = Tbo2[n]+Tbo1[n+1];
Tbi2[n+1] = Tbi2[n]+Tbi1[n+1];
}
Tbo[k] = Tbo2[(int)resolutiony]/(Um[k]*H);
Tbi[k] = Tbi2[(int)resolutiony]/(Um[k]*H);
Es[k] = rhof*Cpf*Um[k]*L*H*(Tbo[k]-Tbi[k]);
for ( it = 0; it <= (int)resolutionx-1; it++)
{
Eh1[it] = (-kse*(Ts[it][1]-Ts[it][0])/dy-kfe*(Tf[it][1]-Tf[it][0])/dy)*dx;
}
Eh2[0] = Eh1[0];
for ( it = 0; it <= (int)resolutionx-1; it++)
{
Eh2[it+1] = Eh2[it]+Eh1[it+1];
}
Eh[k] = Eh2[(int)resolutionx]*L*2;
Writejunk();
Writejunk2();
Writejunk3();
Writejunk4();
WriteU();
WriteY();
WriteX();
WriteTs();
WriteTf();
Writeh();
WriteUm();
}
}
std::cin.get();
return 0;
}

```

LIST OF REFERENCES

- Aritomi, M., Chiang, J. H., 1993, "Geysering in parallel boiling channels," *Nuclear Engineering Design*. 141, 111.
- Barbir, F., 2005, PEM Fuel Cells, Theory and Practice, Elsevier-Academic Press.
- Bao, Z. Y., Fletcher, D. F., and Haynes, B. S., 2000, "Flow boiling heat transfer of Freon R11 and HCFC123 in narrow passages," *International J. Heat Mass Transfer* 43, pp. 3347–3358.
- Bents, D.J., 2004, Power Systems Integration Office, NASA Glenn Research Center, Personal Communication.
- Bergles, A. E., 1977, "Review of Instabilities in Two-Phase Systems," *Two-phase flows and Heat Transfer*, Vol 1. pp. 383-422
- Berning, T., and N. Djilali, 2003, "Parametric Study of Transport Phenomena in PEM Fuel Cells Using a 3D Computational Model," *ASME First Int. Conf. Fuel Cell Science, Engineering & Technology*, Rochester NY, April 21-23, pp. 187-194.
- Boomsma, K., Poulikakos, D., Zwick, F., 2003, "Metal Foams as Compact High Performance Heat Exchangers," *Mechanics of Materials*, Vol. 35, pp. 1161-1176.
- Boure, J.A., Bergles, A.E., Tong, L.S., 1973, "Review of two-phase flow instability," *Nuclear Engineering Design*, 25, 165–192.
- Brutin, D., Tadrist, L., 2004, "Pressure Drop and Heat Transfer Analysis on Flow Boiling in a Minichannel: Influence on the Inlet Condition on Two-phase Flow Instability," *International Journal of Heat and Mass Transfer*, Volume 47, pp. 2365-2377.
- Burke, K., 2003a, "Unitized Regenerative Fuel Cell System Development," *NASA/TM-2003-212739*.
- Burke, K., 2003b, "Fuel Cells for Space Science Applications," *NASA/TM-2003-212730*.
- Calmidi, V.V., and Mahajan, R.L., 2000, "Forced convection in high porosity metal foams," *J. Heat Transfer* 122, pp. 557–565.
- Chang, Y. J., Chang, W. J., Li, M. C., Wang, C. C., 2006, "An Amendment of the Generalized Friction Correlation for Louver Fin Geometry," *International Journal of Heat and Mass Transfer*, Vol. 49, pp. 4250-4253.
- Chang, Y. J., Wang, C. C., 1997, "A Generalized Heat Transfer Correlation for Louver Fin Geometry," *International Journal of Heat and Mass Transfer*, Vol. 40, No. 3, pp. 533-544.

- Chen, J. C., 1966, "A Correlation for Boiling Heat Transfer of Saturated Fluids in Convective Flow," *Eng. Chem. Process Des. Dev.*, Vol. 5, No. 3, pp. 322-329.
- Cooper, M. G., 1984, "Heat flow rates in saturated nucleate pool boiling—A wide ranging examination using reduced properties," J.P. Hartnett and T.F. Irvine, Jr, Editors, *Advances in Heat Transfer* 16, Academic Press, Orlando.
- Coppo, M., Siegal, N. P., Spakovsky, M. R. von, 2005, "On the Influence of Temperature on PEM Fuel Cells", *Journal of Power Sources*, 159, pp. 560-569.
- Djilali, N. and Lu, Dongming, 2002, "Influence of Heat Transfer on Gas and Water Transport in Fuel Cells", *Int. J. Therm. Sci.* Vol. 41, pp. 29-40.
- Dong, J., Chen, J., Chen, Z., Zhang, W., Zhou, Y., 2007, "Heat Transfer and Pressure Drop Correlations for the Multi-Louvered Fin Compact Heat Exchangers," *Energy Conversion and Management*.
- Durga Prasad, G. V., Pandey, M., Kalra, M. S., 2007, "Review of research on flow instabilities in natural circulation boiling systems," *Progress in nuclear Energy*, Volume 49, pages 429-451.
- Faghri, A., 1995, *Heat Pipe Science and Technology*, ISBN 1-56032-383-3, Taylor and Francis.
- Fiebig, M., Valencia, A., Mitra, N. K., 1994, "Local Heat Transfer and Flow Losses in Fin-and-Tube Heat Exchangers with Vortex Generators: A Comparison of Round and Flat Tubes," *Experimental and Thermal Sciences*, Volume 8, Issue 1, pp. 35-45, January.
- Friedel, L., 1979, "Improved friction pressure drop correlations for horizontal and vertical two-phase pipe flow," *3R Int.* 18, pp. 485-492.
- Fujita, H., Ohara, T., Hirota, M., Furuta, H., 1995, "Gas-liquid flows in flat channels with small channel clearance," In: *Proceedings of the Second International Conference on Multiphase Flow*, Kyoto, Japan, IA3-37-IA3-44.
- Fukuda, K., Kobori, T., 1979, "Classification of Two-phase Flow Instability by Density Wave Oscillation Model", *Journal of Nuclear Science and Technology*, Vol. 16, pp. 95-108.
- Garrity, P., Klausner, J., Mei, R., 2007, "A Flow Boiling Microchannel Evaporator Plate for Fuel Cell Thermal Management", *Heat Transfer Engineering*, Vol. 28 no. 10, pp. 877-884.
- Gorenflo, D., and Fath, W., 1987, "Heat transfer on the outside of finned tubes at high saturation pressures," In: *Proc. XVIIth Internat. Congr. of Refrig., Vienna, Austria, Vol. B*, pp. 955-960.
- Gungor, K.E., & Winterton, R.H.S., 1986, "A General Correlation for Flow Boiling in Tubes and Annuli," *International Journal of Heat and Mass Transfer*, Vol. 29, 3, pp. 351-358.

- Gungor, K.E., & Winterton, R.H.S., 1987, "Simplified General Correlation for Saturated Flow Boiling and Comparisons of Correlations with Data," *Chem. Eng. Res. Des.*, vol. 65., pp. 148-156.
- Haack, D. P. , Butcher, K.R., Kim, T., Lu, T.J., 2001, "Novel Lightweight Metal Foam Heat Exchangers," *2001 ASME Congress Proceedings*, NY, November 2001.
- Hsieh, W. H., Wu, J. Y., Shih, W. H., Chiu, W. C., 2004, "Experimental Investigation of Heat-Transfer Characteristics of Aluminum-Foam Heat Sinks" *International Journal of Heat and Mass Transfer*, Volume 47, pp. 5149-5157
- Hwang, J.J., Hwang, G.J., Yeh, R.H., Chao, C.H., 2002, "Measurement of Interstitial Convective Heat Transfer and Frictional Drag for Flow Across Metal Foams," *Journal of Heat Transfer*, Volume 124, February.
- Ide, H. and Matsumura, H., 1990, "Frictional pressure drops of two-phase gas-liquid flow in rectangular channel," *Exp. Thermal Fluid Sci.* 3, pp. 362-372.
- Incropera, F.P., Dewitt, D.P., Bergman, T.L., Lavine, A.S., 2007, "Fundamentals of Heat and Mass Transfer", 6th edition.
- Ishii, M, 1970, "Study of Flow Instabilities in two-phase mixtures", ANL-76-23.
- Jeng, T. M., Liu, L.K., Hung, Y.H., 2005, "A Novel Semi-Empirical Model for Evaluating Thermal Performance of Porous Metallic Foam Heat Sinks," *Journal of Electronic Packaging*, Volume 127, September.
- Jiang, S. Y., Zhang, Y. J., Wu, X. X., Bo, J. H., Jia, H. J., 2000, "Flow Excursion Phenomenon and its Mechanism in Natural Circulation," *Nuclear Engineering and Design*, Volume 202, pages 17-26.
- Joshi, S. V., Bokil, R. S., Nayak, J. K., 2005, "Test standards for thermosyphon-type solar domestic hot water system: review and experimental evaluation, *Solar Energy*, Vol. 78, Issue 6, pp. 781-798.
- Kakac, S., Bon, B., 2008, "A Review of Two-phase Flow Dynamic Instabilities in Tube Boiling systems", *International Journal of Heat and Mass Transfer*, Vol. 51, pp. 399-433.
- Kandlikar, S. G., 1991, "A Model for Correlating Flow Boiling Heat Transfer in Augmented Tubes and Compact Evaporators," *Journal of Heat Transfer*, 113, pp. 966-972.
- Kandlikar, S. G., 2001, "Two-phase Flow Patterns, Pressure Drop and Heat Transfer During Boiling in Minichannel and Microchannel Flow Passages of Compact Heat Exchangers," *Compact Heat Exchangers and Enhancement Technology for the Process Industries*, Begell House, New York, pp. 319-334.

- Kandlikar, S.G., Steinke, M. E., 2003, "Predicting Heat Transfer During Flow Boiling In Minichannels and Microchannels," *ASHRAE Transactions* 109 (1), pp. 1-9.
- Kandlikar, S. G., Balasubramanian, 2004, P., "An Extension of the Flow Boiling Correlation to Transition, Laminar, and Deep Laminar Flows in Minichannels and Microchannels," *Heat Transfer Engineering*, 25 (3), 86-93.
- Kandlikar, S.G., Balasubramanian, P., 2005, "Experimental Study of Flow Patterns, Pressure Drop, and Flow Instabilities in Parallel Rectangular Minichannels," *Heat Transfer Engineering*, 26 (3), pp. 20-27.
- Kasza, K. E., Didascalou, T., Wambsganss, M. W., 1997, "Microscale Flow Visualization of Nucleate Boiling in Small Channels: Mechanisms Influencing Heat Transfer," Shah, R. K., (Ed.), *Proceedings of International Conference on Compact Heat Exchangers for Process Industries*, Begell house, New York, pp. 343-352.
- Kim, S. Y., Paek, J. W., Kang, B. H., 2000, "Flow and Heat Transfer Correlations for Porous Fin in a Plate-Fin Heat Exchanger," *Journal of Heat Transfer*, Vol. 122, pp. 572-578.
- Klett, J. W., McMillan, A., Gallego, N., 2002, "Carbon Foam for Electronics Cooling," *National Laboratory Fuel Cell Annual Report*.
- Klimenko, V. V., 1990, "A generalized correlation for two-phase forced flow heat transfer," *Internat. J. Heat Mass Transfer* 31, pp. 541–552.
- Kyung, I.S., Lee, S. Y., 1996, "Periodic flow excursion in an open two-phase natural circulation loop," *Nuclear Engineering Design*, 162, 233-244.
- Lasbet, Y., Auvity, B., Castelain, C., Peerhossaini, 2006, H., "A Chaotic Heat-Exchanger for PEMFC Cooling Applications," *Journal of Power Sources Journal of Power Sources*, Vol. 156, Issue 1, pp. 114-118.
- Ledinegg, M., 1938, "Instability of flow during natural and forced circulation," *Die Warme* 61, 881.
- Lee, H.J, Lee, S.Y., 2001, "Pressure drop correlations for two-phase flow within horizontal rectangular channels with small heights," *International Journal of Multiphase Flow*, 27 pp. 783-796.
- Lockhart, R. W., and Martinelli, R. C., 1949, "Proposed correlation of data for isothermal two-phase, two-component flow in pipes," *Chemical Engineering Progress Symposium Series* 45, pp. 39–48.
- Lowry, B. and Kawaji, M., 1988, "Adiabatic vertical two-phase flow in narrow flow channels," *AIChE Symposium Series* 84 263, pp. 133–139.

- Lu, W., Zhao, C., Tassou, S., 2006, "Thermal analysis on metal-foam filled heat exchangers. Part I: Metal-foam filled pipes," *International Journal of Heat and Mass Transfer*, Volume 49, Issue 15-16, pp. 2751-2761
- Liu, Z., and Winterton, R.H.S., 1991, "A general correlation for saturated and subcooled flow boiling in tube and annuli, based on a nucleate pool boiling equation," *Internat. J. Heat Mass Transfer* 34, pp. 2759–2766.
- Lui, H. T., Kodak, G., Kakac, S., 1995, "Dynamical Analysis of Pressure Drop Type Oscillations with a Planar Model," *International journal of Multiphase Flow*, Volume 21, Issue 5, Pages 851-859.
- Mehendal, S. S., Jacobi, A. M., Shah, R. K., 2000, "Fluid Flow and Heat Transfer at Micro- and Meso-scales with Application to Heat Exchanger Design," *Appl. Mech. Rev.* 53 (7), 175-193.
- Mishima, K. and Hibiki, T., 1996, "Some characteristics of air–water two-phase flow in small diameter vertical tubes," *Int. J. Multiphase Flow* 22, pp. 703–712.
- Mishima, K., Hibiki, T. and Nishihara, H., 1993, "Some characteristics of gas–liquid flow in narrow rectangular ducts," *Int. J. Multiphase Flow* 19 1, pp. 115–124.
- Muller-Steinhagen, H. Heck, K., 1986, "A Simple Friction Pressure Drop Correlation for Two-Phase Flow in Pipes," *Chemical Engineering Processes*, Vol. 20, pp. 297-308.
- Muller-Steinhagen, H., Jamialahmadi, M. 1996, "Subcooled Flow Boiling Heat Transfer to Mixtures and Solutions," *Convective Flow Boiling*, Editor John C. Chen, Taylor & Francis, Washington D.C.
- Palm, B. and Tengblad, N., 1996, "Cooling of electronics by heat pipes and thermosyphons—A review of methods and possibilities," *Proc. Nat. Heat Transfer Conf.*, vol. 7, HTD-Vol. 329, pp. 97–108.
- Peterson, G. P., Duncan, A. B., and Weichold, H. M., 1993, "Experimental Investigation of Micro Heat Pipes Fabricated in Silicon Wafers," *Journal of Heat Transfer*, vol. 115, pp. 751-756.
- Ramaswamy, C., Joshi, Y., Nakayama, W., Johnson, W. I., 1998, "Combined effects of sub-cooling and operating pressure on the performance of a two-chamber thermosyphon," *Thermal and Thermomechanical Phenomena in Electronic Systems*, ITherm '98. The Sixth Intersociety Conference on, Seattle, WA, May 1998.
- Ribatski, G., Wojtan, L., Thome, J. R., 2006, "An analysis of experimental data and prediction methods for two-phase frictional pressure drop and flow boiling heat transfer in micro-scale channels," *Experimental Thermal and Fluid Science*, Vol. 31 (1), pp. 1-19.
- Ross, H. D., and Radermacher, R., 1987, "Suppression of nucleate boiling of pure and mixed refrigerants in turbulent annular flow," *Internat. J. Multiphase Flow* 13, pp. 759–772.

- Saha, P, Zuber, N, 1974, "Point of Net Vapor Generation and Vapor Void Fraction in Subcooled Boiling," *Proceedings of 5th International Heat Transfer Conference*, Vol. 4, pp 175-179.
- Schmidt, ThE., 1949, "Heat Transfer Calculations for Extended Surfaces," *Refriger. Eng.* April, pp. 351-357.
- Steiner, D., and Taborek, J., 1992, "Flow boiling heat transfer in vertical tubes correlated by an asymptotic model" *Heat Transfer Eng.* 13, pp. 43–69.
- Stenning, A. H., Veziroglu, T. N., 1967, "Oscillations in Two-Component Two-Phase Flow," NASA CR-72121, Volume 1.
- Tadrist, L., 2006, "Review on two-phase flow instabilities in narrow spaces," *International Journal of Heat and Fluid Flow*, Volume 28, pp. 54-62.
- Thome, J. R., 2004, "Boiling in Microchannels: A Review of Experiment and Theory," *International Journal of Heat and Mass Transfer*, Vol. 25, pp. 128-139.
- Thome, J. R., Dupont, V., Jacobi, A. M., 2004, "Heat Transfer Model for Evaporation in Microchannels Part I: Presentation of the Model."
- Tran, T. N., Wambsganss, M. W., and France, D. M., 1996, "Small circular- and rectangular-channel boiling with two refrigerants," *Internat. J. Multiphase Flow*, 22 3, pp. 485–498.
- Tuckerman, D and Pease, R. E, 1981, "High Performance Heat Sinking for VLS", *I. IEEE Electronic Device Letters*. EDL-2 , pp.126-129.
- Tzeng, S. C., 2007, "Spatial Thermal Regulation of Aluminum Foam Heat Sink Using Sintered Porous Conductive Pipe," *International Journal of Heat and Mass Transfer*, Volume 50, pp. 117-126
- Vafai, K., Kim, S.J, 1989, "Forced convection in a channel filled with a porous medium: an exact solution", *ASME Journal of Heat Transfer*, Vol. 111 pp.1103-6.
- Van Bragt, D.D.B., 1998, "Analytical Modeling of Boiling Water Reactor Dynamics," Delft University Press.
- Vishnyakov, V. M., 2006, "Proton exchange membrane fuel cells," *Vacuum*, Volume 80, Issue 10, The World Energy Crisis: Some Vacuum-based Solutions, 3 August 2006, Pages 1053-1065.
- Wambsganss, M.W., Jendrzejczyk, J.A. and France, D.M., 1991, "Two-phase flow patterns and transitions in a small, horizontal, rectangular channel," *Int. J. Multiphase Flow* 5, pp. 40–56.
- Wambsganss, M.W., Jendrzejczyk, J.A., France, D.M. and Obot, N.T., 1992, "Frictional pressure gradients in two-phase flow in a small horizontal rectangular channel," *Exp. Thermal Fluid Sci.* 5, pp. 40–56.

- Wang, C. C., Lee, C. J., Chang, C. T., Lin, S. P., 1999, "Heat Transfer and Friction Correlation for Compact Louvered Fin and Tube Heat Exchangers," *International Journal of Heat and Mass Transfer*, Vol. 42, pp. 1945-1956.
- Wetton, B., Promislow, K., Caglar, 2004, A., "A simple thermal model of PEM fuel cell stacks," *Proceedings of the Second International Conference on Fuel Cell Science, Engineering and Technology*, Rochester NY, June.
- Yadiaroglu, G., 1981, "Two-phase flow instabilities and propagation phenomena," *Thermohydraulics of Two-phase Systems for Industrial Design and Nuclear Engineering* (Edited by J. M. Delhaye, M. Giot and M. L. Riethmuller), Chap. 17 McGraw-Hill, New York.
- Yadigaroglu, G., Bergles, A. E., 1969, An Experimental and Theoretical Study of Density-Wave Oscillations in Two-Phase Flow, MIT rept. DSR 74629-3 (HTL 74629-67).
- Yang, X.T., Jiang, S.Y., Zhang, Y.J., 2005, "Mechanism Analysis on Flow Excursion of a Natural Circulation with Low Steam Quality," *Nuclear Engineering and Design*, 235, pp. 2391-2406.
- You L., Liu H., 2002, "A Two-phase Flow and Transport Model for the Cathode of PEM Fuel Cells," *International Journal of Heat and Mass Transfer*, 45 (11), pp. 2277-2287.
- Zhang, Y., Ouyang, M., Qingchun, L., Luo, J., Li, X., 2004, "A Model Predicting Performance of Proton Exchange Membrane Fuel Cell Stack Thermal Systems," *Applied Thermal Engineering*, Vol. 24, pp. 501-513.
- Zhao, C., Lu, W., Tassou, S., 2006, "Thermal analysis on metal-foam filled heat exchangers. Part II: Tube heat exchangers," *International Journal of Heat and Mass Transfer*, Volume 49, Issue 15-16, Pages 2762-2770.
- Zuber, N., and Findlay, J. A., 1965, "Average Volumetric Concentration in Two-Phase Flow Systems", *Journal of Heat Transfer*, Vol. 87, pp. 453-468.
- Zuo, Z. J., Fale, J. E., Gernert, N. J., 2000, "Study of Drainage Disk Thermosyphon Condenser Design," *Journal of Enhanced Heat Transfer*, Volume 7, Issue 3.

BIOGRAPHICAL SKETCH

Patrick Garrity is a Ph.D. student focusing on thermal science and fluid dynamics at the University of Florida, United States. He received his bachelor's degree from the University of Massachusetts in 2004. Currently he is working on thermal management of PEM fuel cells with a focus on microchannel flow boiling.